Comparison of Resedimented with Intact Mudrock Behavior

a thesis submitted by

James M. Finnegan

In partial fulfillment of the requirements for the degree of

Master of Science in Civil and Environmental Engineering

Tufts University

Medford, MA

August 2020

Advisor: John T. Germaine

ABSTRACT

This thesis studies Gulf of Guinea Miocene Mudrock (GoG) samples, provided by Chevron, and compares resedimented to intact engineering properties. GoG required a new processing method to break apart clay floccs. Clay mineralogy is dominated by kaolinite, and plasticity is unusually high for kaolinite based on Atterberg limits. Hydrometer tests had significant bias, likely caused by structured water, abnormally dense water bonded in layers to the surface of the clay particles.

CRS tests show that resedimented specimens are less dense than intact specimens at the in situ stress level of 9.5 MPa, and permeability is similar. Mercury porosimetry data show similar pore size distributions. One CRS test was performed on an intact specimen using the same methods, and the intact compression index was very similar to that of the resedimented specimens. However, porosity of the intact specimen was slightly higher, and intact yield stress was much higher.

ACKNOWLEDGEMENTS

TABLE OF CONTENTS

LIST OF TABLES

LIST OF FIGURES

1 INTRODUCTION

1.1 PROBLEM STATEMENT AND RATIONALE

Resedimentation has been used to systematically study soils for decades because it allows for control over porosity and stress history. The results from tests on resedimented specimens have been used to develop numerous correlations and material models. However, the mechanical behavior of resedimented specimens has never been directly compared to preserved intact specimens of the same material using the same testing procedures. Now those material models and correlations will be validated by comparing the behavior of the intact material that they model to the behavior of the resedimented material that they are based on.

The goal of this research is to compare the behavior of resedimented Gulf of Guinea Miocene Mudrock to that of preserved intact Gulf of Guinea Miocene mudrock using the same testing methods. This research was made possible by the UT GeoFluids consortium and by Chevron. Gulf of Guinea Miocene Mudrock is a new material in the GeoFluids database, through the process of this research index tests were performed to classify it and integrate it into the database.

1.2 RESEARCH OBJECTIVES AND SCOPE

The objectives and scope of this research are presented in the following list:

1. Conduct a literature review of the geologic history of the Gulf of Guinea Miocene Mudrock deposit and previous attempts to compare intact and resedimented behavior

2. Develop a method for processing the non-preserved material for resedimentation and testing

3. Characterize the material with a suite of index property tests

4. Characterize the engineering properties of the resedimented material using triaxial and CRS tests on resedimented specimens

5. Develop methods for preparing intact specimens for triaxial and CRS testing

6. Characterize the engineering properties of the intact material using triaxial and CRS tests on intact specimens

7. Compare the engineering behavior of the resedimented material to that of the intact material

8. Compare the engineering behavior of Gulf of Guinea mudrock to the rest of the GeoFluids databse

1.3   ORGANIZATION OF THE THESIS

This thesis is organized into 6 chapters:

The second chapter discusses background on the Gulf of Guinea Mudrock. It includes a geological background, including location, geologic history, deposition history, and details on the source material. It also includes a background on the previous geotechnical research on the engineering behavior of mudrocks and previous comparisons of intact to resedimented behavior.

The third chapter summarizes the specimen preparation and testing program. It details the processing methods developed to prepare the non-preserved material for resedimentation and testing. It describes the testing program for the research: index tests, triaxial tests, and CRS tests. It also describes procedures for resedimentation and for preparing intact specimens for testing.

The fourth chapter explains the laboratory equipment and methods used in the research. It describes the electronic instrumentation in the Tufts laboratory. It summarizes the methods for index tests used to classify the material. It summarizes the methods used for engineering tests: triaxial and CRS tests, and the differences between methods for tests on intact and resedimented specimens.

The fifth chapter details test results. It details index test results, consolidation results from CRS tests and the K_0 consolidation portion of triaxial tests, permeability results from CRS tests, and shear results from triaxial tests. It presents a comparison between intact and resedimented results for each type of tests and a summary of findings at the end.

The sixth chapter concludes the thesis by summarizing the testing methods developed as part of the research, summarizing the test results and conclusion, and providing recommendations for future work.

2 BACKGROUND

2.1 INTRODUCTION

The source material for this research is a marine mudrock deposited off the coast of West Africa, referred to at Gulf of Guinea Mudrock. This is a new material for the Geofluids database, which is summarized in Table 2-1. Chevron provided non-preserved cores of the material for index testing and resedimentation. Chevron also provided preserved intact specimens cut to appropriate dimensions for CRS and Triaxial testing. This chapter presents background on the material and previous related work.

Section 2.2 recaps a geologic background on the material, including location, source material, and deposition. Section 2.3 describes previous research done on mudrocks and hard clays.

2.2 GEOLOGIC BACKGROUND

2.2.1 Location of Sampling

The Gulf of Guinea mudrock samples used in this research were retrieved by Chevron offshore near the coast of Angola's Cabinda province in a region known as Block 14. Block 14 is a tract of approximately 1560 square miles designated for oil and natural gas drilling, shown in Figure 2-1. The material was retrieved from approximately 3,200 feet below mudline. The geological region is commonly referred to as the Congo Submarine Fan (Figure 2-2), due to the sedimentary influence of the Congo River in the area. The region has been studied by the oil industry due to the presence of oil and natural gas deposits.

2.2.2 Geologic History of the Congo Submarine Fan

The South American continent fit into the Gulf of Guinea before continental drift as part of the Gondwana supercontinent (Bullard, Everett, & Gilbert Smith, 1965). The West African continental margin formed after the breakup of the supercontinent and opening of the South Atlantic Ocean in the early Cretaceous period (Burke, Dessauvagie, & Whiteman, 1971). Erosional events were responsible for removing up to 1000 meters of sediment from the Congo Fan between its formation and the present day. The first erosional event took place in the Eocene. It is thought to be caused either by the upper slope and shelf break of the continental margin being eroded by deep ocean current, or by sea level change (McGinnis, Driscoll, Karner,

Brumbaugh, & N., 1993). The second erosional event, which is associated with seaward tilting and uplift of the margin, took place in the early Miocene (~24 Ma). The Congo River shifted to its current location at the end of the Miocene period (5 Ma). (Brice, Cochran, Pardo, & Edwards, 1982; Uenzelmann-Neben, Spiess, & Bleil, 1997)

A geologic time scale is shown in Figure 2-3 for reference. The scale includes sketches of the presumed locations of the continents through geologic time.

2.2.3   Deposition History

Sediments below the unconformity formed by the first major erosional event are primarily pelagic carbonates. The sediments above the unconformity are primarily terrigenous siliciclastics (Savoye, Babonneau, Dennielou, & Bez, 2009). Gulf of Guinea Miocene Mudrock was deposited above the unconformity, and geologic evidence shows that it was not tectonically uplifted between deposition and present day.

The deposit from which the Gulf of Guinea Miocene mudrock material used for this research came was deposited during Miocene period (24 – 5.3 Ma). Sedimentation rates increased during the Miocene period, due to a combination of both continental uplift and climate change. Sedimentation rates in the region are well-correlated with continental uplift. (Seranne, Seguret, & Fauchier, 1992)

Geologists speculate that global cooling causes changes in seasonal and latitudinal temperature gradients and an increase in temperature contrasts between the continents and oceans. Any readjustment of the landscape to altered conditions should be associated with increased erosion (Willgoose, Bras, & Rodriguez, 1991). The Congo River drains a large portion of the African continent, so it records shifts in climatic conditions as changes in sediment supply. Continental uplift caused an increase in relief at the continental margin, which would have caused an increase in the terrigenous sediments deposited in the region. The effects of uplift and climate change are documented in the literature to have increased the clastic sediment supply to the Congo River fan in the Miocene era. (Lavier, Steckler, & Brigaud, 2001; Seranne M. , 1999).

Lavier, Steckler, and Birgaud (2001) reconstructed the stratigraphy along two cross sections across the Congo and Angolan margins from the Eocene (58 Ma) to the present. The closer cross section to Block 14, where the Gulf of Guinea mudrock was retrieved, is referred to

as the Angola cross section. The location of the Angola cross section is shown in Figure 2-4. It presents a geologic profile for visualizing the deposition history. Figure 2-5 shows the cross section at the Eocene-Oligocene transition (34.5 – 24 Ma). It was during this time that the first major submarine erosion of the continental slope took place, and the sediment type changed from pelagic carbonates to terrigenous siliciclastics. Figure 2-6 shows the cross section from the Miocene to the present day. It was during this time that the Gulf of Guinea mudrock studied for this research was deposited. During this time, sedimentation rates increased due to continental uplift and climate change, and the sediment supply in the area grew seaward. The cross sections show the Miocene sediments being buried by newer sediments and remaining buried until the present day. The high angle faults in the region are also shown.

2.2.4   Source Material

Uenzelmann-Neben (1998) developed a model of the sedimentation history of the Congo fan area based on interpretation of high resolution seismic reflection data. In the late Paleogene, the Congo fan had one main source of sediment deposition: the Kouilou-Niari River, which is located approximately 150 miles north of the Congo River, entirely within the borders of the Republic of the Congo. During the Neogene period, the Congo river gradually became a second main source, and the two rivers both contributed to sediment deposition. The influence of the Kouilou-Niari diminished after the Neogene, and the Congo became the prevailing sediment source for the fan. The Congo remains the main source of sediment to the present day, with the deposition location having moved further west into the lower fan. The evolution of sediment sources is depicted in Figure 2-7. Sediments in the whole area have evidence of gas. (Uenzelmann-Neben, 1998)

The sedimentation model developed by Uenzelmann-Neben (1998) does not pinpoint the composition and sources of sediments that were deposited on the Congo fan throughout geologic time; rather, it focuses on changes in depositional location and rates of deposition over the life of the fan. Therefore, the best way to approximate the makeup of the source material for the Gulf of Guinea mudrock is to investigate the geologic makeup of the Congo Basin and the climate of the basin at the time of deposition.

The Congo River Basin (Figure 2-8) is one of the largest continental sedimentary basins in the world, covering over 1.2 million square kilometers (463,000 square miles). Little is known

about it compared to other basins of similar size due to a variety of factors including: inconsistent nomenclature and inaccessibility between countries due to decades of conflict; minimal outcrop exposure; limited and often proprietary seismic, core, and well data; a lack of datable volcanics; and sporadic distribution of diagnostic fossils (Roberts, Jelsma, & Hegna, 2015). The Congo Basin is an intracratonic basin, meaning that it is a broad, saucer-shaped basin within a stable continental crustal mass. The basin is a broad plain whose borders are made up of plateaus and areas of high topographic relief. The Atlantic margin was uplifted to form the present western boundary of the basin during the breakup of the Gondwana supercontinent (Bullard, Everett, & Gilbert Smith, 1965; Burke, Dessauvagie, & Whiteman, 1971). The East African Rift shoulder forms the eastern boundary of the basin, and plateaus of the Central African shield form the northern and southern boundaries. (Roberts, Jelsma, & Hegna, 2015) A simplified geologic map of the Congo Basin is shown in Figure 2-9.

The Congo Basin receives an average rainfall of 1500 mm per year (59 inches per year), with some regions receiving upwards of 2000 mm per year (79 inches per year). The basin makes up a portion of the sub-Saharan African jungle; approximately 65% of the land area in the basin is characterized as a tropical savanna climate, and the remaining 35% is a tropical rainforest. Crystalline and metamorphic rocks, including gneiss, migmatites, amphibolites, and granitic intrusions, dominate the basement rocks of the basin. The central plain consists of sand, sandstones, and argillites. The western part of the basin is made up of coastal formations that are mainly sandstones and limestones (Negrel, Allegre, Dupre, & Lewin, 1993).

The sedimentary fill in the Congo basin can be up to 9 km thick. Sediment ages span from Proterozoic to present day. The origin of the sediments varies widely across the basin, ranging from crystalline basement rocks to ancient deformed sediments. Roberts, Jelsma, & Hegna (2015) divide the stratigraphy of the basin into five sequences. The five sequences are breifly described below in order of age from oldest to youngest:

1. Shallow marine limestones – formed from stromatolites, which are layered mounds of sedimentary rocks formed in shallow water by bio-chemical processes
2. Marine clastics – deposited when a marine transgression flooded the basin
3. Marine cyclothem – alternating marine and non-marine deposits of sandstone and shale

4. Lacustrine deposits – glacial, peri-glacial, and interglacial deposits formed in glacial lake environments

5. Triassic and Cenozoic clastic units – regionally extensive, mostly flat-lying deposits

Roberts, Jelsma, & Hegna (2015) cite debate and lack of understanding regarding the age and details of the sequences within the geologic community. Further detail on the sequences is beyond the scope of this work.

According to the sedimentation model developed by Uenzelmann-Neben (1998) the Congo fan received sediments deposited from both the Congo River and the Kouilou-Niari River during the Miocene, when the Gulf of Guinea mudrock was deposited. The Kouilou-Niari Basin is a comparatively small basin. It drains mostly the uplifted Atlantic margin, which is made up mostly of Proterozoic and Cenozoic sediments. The climate of the basin is classified as tropical savanna.

The climate of the region experienced mild warming and then was stable between the Oligocene and Middle Miocene: still within the tropical climatic zone (Broucke, et al., 2004). Tropical climates with high precipitation have the potential for high rates of suspended sediment transport (Mitchell & Soga, 2005). The increase in deposition on the Congo fan during the Miocene discussed in section 2.2.2 is consistent with the climate history. Kaolinite is known to commonly form in humid, tropical regions due to their high rates of chemical weathering (Mitchell & Soga, 2005). Based on the climate present in the region at the time, it is reasonable to expect that a significant portion of the suspended sediment being removed from the basin was kaolinite, which makes up a significant portion of the Gulf of Guinea mudrock.

2.3   PREVIOUS WORK

The relationship between intact and resedimented mudrock behavior has not been extensively studied, and there is little consensus on how accurately resedimented specimens predict intact behavior. The literature on the topic can be broken down into two categories: studies in the geotechnical field which deal with low stresses and short time scales, and studies in the geological or petroleum engineering field which deal with higher stresses and geological time scales.

2.3.1 Geotechnical Studies

Some studies in the geotechnical community have identified the aging of soils as having an impact on behavior. Anderson and Woods (1976) concluded that all cohesive soils experience a log linear increase in shear stiffness with time. They identified two separate time domains for modulus increase: a primary domain that coincides with primary consolidation, and a secondary domain of long-term time effect that occurs after primary consolidation. They defined a parameter known as N_G that quantifies the increase in shear stiffness with aging:

$$N_G = \frac{\Delta G_{MAX}}{\Delta G_{MAX(t-t_{ref})} \log\left(\frac{t}{t_{ref}}\right)} \qquad \text{2-1}$$

$where: \Delta G_{MAX(t-t_{ref})} = initial\ shear\ stiffness\ determined\ at\ a\ reference\ time(t_{ref})$
$\quad \Delta G_{MAX} = increase\ in\ shear\ stiffness\ a\ time\ with\ respect\ to\ t = t_{ref}$
$\quad t = generic\ time$

Anderson and Stokoe (1978) concluded that all soils exhibit a long term time effect, and that time effect cannot be explained simply by changes in void ratio due to secondary compression. They proposed that the increase in stiffness over time resulted from a strengthening of physical-chemical bonds in cohesive soils, and an increase in particle contact in cohesionless soils.

Burland (1990) referred to the properties of reconstituted clays as "intrinsic" because they are inherent to the soil and independent of the natural state and any structure or fabric that has developed. He introduced the concept of a void index, I_v, a normalizing parameter defined below:

$$I_v = \frac{e - e_{100}^*}{e_{100}^* - e_{1000}^*} \qquad \text{2-2}$$

$where\ e_{100}^*; e_{1000}^* = void\ ratio\ at\ 100\ kPa\ and\ 1000\ kPa, respectively$

Burland plotted I_v versus the log of effective stress for both reconstituted and natural sedimentary clays. From those plots, he differentiated the intrinsic compression line (ICL) for reconstituted clays, and the sedimentary compression line (SCL) for natural soils. He found that the SCL lies above the ICL for most normally consolidated clays. For clays whose SCL is well above the ICL, the two curves tend to converge at higher stresses, which implies the collapse of

the natural structure with increase in stress. For clays whose SCL lies close to the ICL, the two curves tend to remain parallel, which implies that the natural and reconstituted structure are similar. Burland concluded that the properties of natural clay differ from the intrinsic (reconstituted) properties due to the influence of soil structure, which is defined as fabric and bonding. Soil structure depends on depositional conditions and post-depositional processes such as leaching.

Schmertmann (1991) addressed the mechanisms responsible for changes in mechanical behavior associated with "engineering aging," or short term aging. He suggested that the phenomenon had a primarily mechanical origin, even in clays, stating that engineering aging effects involve primarily the movement of particles and changes in the structure or fabric of the soil. He did not describe chemical bonding or other cohesion effects as playing a major role in age-strengthening over engineering time scales, but he pointed out that "changes in the particles themselves" are caused over geologic time by chemical effects.

Santagata and Kang (2006) analyzed shear stiffness data obtained with seismic cone penetrometer tests (CPT) at three sites on Boston Blue Clay (BBC). They compared the CPT results to the results of over 90 triaxial tests that had been performed on resedimented BBC (RBBC). They concluded that at the same OCR and stress level, natural clay on average displays an initial stiffness 50% greater than that of resedimented clay.

House (2012) compared the behavior of intact BBC to the behavior of RBBC using previous consolidation and strength data from tests performed at MIT. The study was focused on tests on normally consolidated specimens which had corresponding Atterberg limit data. House compared permeability, compressibility, coefficient of consolidation, lateral stress ratio, undrained strength, and friction angle between BBC and RBBC. House concluded that although there was enormous data scatter in natural BBC specimens, resedimentation was overall a good analog for mechanical behavior of field specimens.

The geotechnical literature comparing intact to resedimented clays is limited to low stress levels and short time durations. The studies above analyzed specimens at stress levels mostly below 1 MPa, and the duration of the lab testing was on the order of days or weeks. Some of the authors attempt to extrapolate lab behavior out to geologic time, but the geotechnical literature does not provide an accurate comparison to the stress levels and time scales of mudrocks.

2.3.2 Studies at Larger Stress Levels and Time Scales

Karig and Ask (2003) investigated late Miocene aged silty mudrocks retrieved from the Nankai trough off the coast of Japan and middle Eocene aged carbonate mudrocks retrieved from the Atlantic abyssal plain off of Portugal, and they attempted to compare the results to geotechnical literature. They performed uniaxial strain tests to stresses varying between 0.2 and 20 MPa in triaxial cells with an algorithm to maintain constant cross-sectional area on intact and disaggregated sediments. The compression curves of the disaggregated material had the same slope as the intact material, but at a higher porosity. Their methods of disaggregation and reconstitution of test specimens are unclear. They concluded that some of the commonly accepted geotechnical behavior cannot be validly extrapolated to mudrocks under higher stresses and longer time scales. During creep, porosity is assumed to be log linear with stress. They concluded that assumption is not valid for mudrocks at effective stress above 1 MPa, and that secondary compression index increases with stress. However, they concluded that the yield stress still accurately reflects the previous maximum consolidation state for the materials they tested. They identified a new phase of post-yield strain for these materials. It exhibited higher values of compression index than elastic deformation, but lower values than virgin compression. They termed this phase "tertiary consolidation," and a schematic of how it fits into the typical geotechnical framework of primary and secondary consolidation is shown in Figure 2-10.

Betts (2014) characterized the compression and permeability of resedimented high plasticity Gulf of Mexico mudrock from the Eugene Island block (RGoM_EI) off the coast of Louisiana with CRS tests up to 20 MPa. He compared the results of those tests to field porosity measurements that were calculated using two different methods: empirical correlations based on sonic velocities and integration of bulk density. The resedimented porosity fell below the density derived porosity, and above the sonic derived porosity. Betts concluded that RGoM_EI is a reasonable analog for field behavior. Betts conducted a literature review of previous attempts at comparing intact to resedimented behavior and created a chart (Figure 2-11) that illustrates the disagreement to date using two sources mentioned above (Burland, 1990; Karig & Ask, 2003).

Daigle and Screaton (2015) assembled a data set of permeability measurements from over 25 years of drilling at 317 subduction zones worldwide. They compared lab methods including steady state flow tests, uniaxial consolidation tests, and transient pulse decay to downhole field

measurements. Their work confirmed previous research that porosity-permeability behavior is a function of clay-size fraction. They concluded that the lab trends matched large scale field trends for samples retrieved from structural domains with negligible shear; however, in domains where shear is significant, lab trends consistently underestimate the rate of permeability reduction with loss of porosity.

2.3.3 Conclusion

Although some attempts have been made, as discussed above, to compare the mechanical behavior of intact and resedimented specimens, several of the studies have shortcomings regarding time and stress level. Attempts to explain age related changes in properties center around mechanical changes in the orientation of particles and chemical changes in the particles themselves, but no consensus has been reached. Of the few studies that account for the geologic time scale and stress level of mudrocks, none use consistent laboratory methods in their comparisons.

Name	Liquid Limit (%)	Plastic Limit (%)	Plasticity Index (%)	Clay Fraction (%)	Specific Gravity	USCS Classification
Resedimented Boston Blue Clay (RBBC)	47	24	23	56	2.778	CL
Resedimented Gulf of Mexico Eugene Island Block (RGoM_EI	87	24	63	65	2.775	CH
Resedimented Gulf of Mexico Ursa (RGoM_Ursa)	52	24	28	54	2.667	CH
Resedimented Cornwall Kaolin (RK_Cornwall)	48	29	19	64	-	ML
Resedimented Edgar Plastic Kaolin (RK_EPK)	68	37	31	73	-	MH
Resedimented Villanova Tulo White Kaolin (RK_VWK)	49	34	15	50	-	ML
Resedimented London Clay (RLC)	74	31	43	63	2.8	CH
Resedimented Presumpscot Clay (RPC)	33	19	14	37	2.772	CL
Resedimented San Francisco Bay Mud (RSFBM)	60	32	28	52	2.69	MH
Resedimented Ugnu Clay (RUC)	57	26	31	44	2.699	CH
Resedimented Nankai Clay (RNC)	68	29	39	55	2.68	CH
Resedimented Nile Silty Clay (RNSC)	80	27	53	-	-	-
Skibbereen Silt (SS)	-	-	-	-	-	-
Resedimented Florida Bay Mud (RFB)	-	-	-	-	-	-

Table 2-1: Geofluids database summary
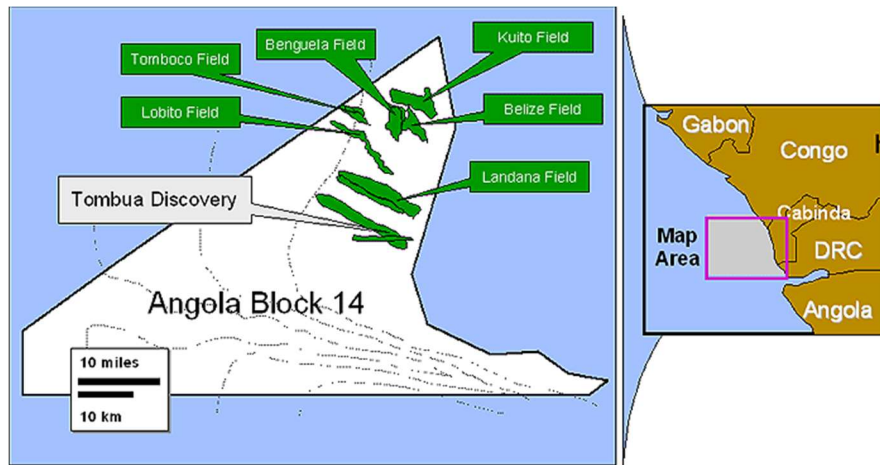
Figure 2-1: Block 14 map
(Chevron USA, 2001)
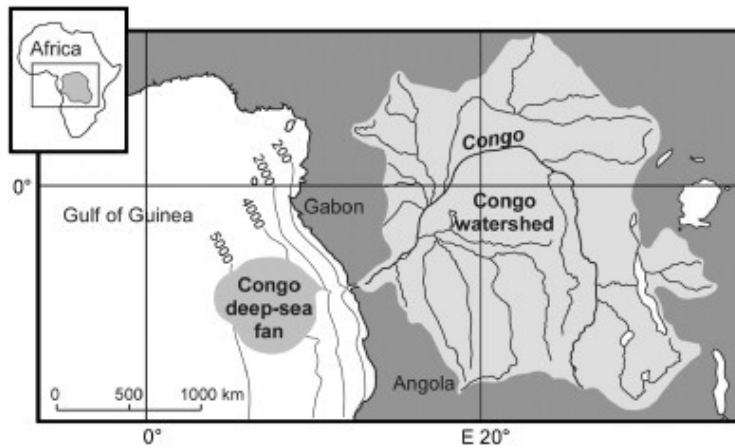
Figure 2-2: Congo Basin and fan map
(Marques, 2015)

Eon	Era	Period		Epoch	Time	Life	Tectonics
Phanerozoic	Cenozoic	Quaternary		Holocene	0.01	Homo sapiens	
				Pleistocene	1.6	Homo erectus	
		Tertiary	Neogene	Pliocene	5.3	hominins	
				Miocene	24	apes	
			Paleogene	Oligocene	37	primates	
				Eocene	58	major mammal diversification	
				Paleocene	66	end of dinosaurs	
	Mesozoic	Cretaceous			144	early birds dinosaurs	
		Jurassic			208		
		Triassic			245	early mammals amniotes	
	Paleozoic	Permian			286	tetrapods Acanthostega	
		Carboniferous			360		
		Devonian			408	Eusthenopteron	
		Sulurian			438		
		Ordovician			505		
		Cambrian			570		
Pre-cambrian	Proterozoic				2500		
	Archean				3800		
	Hadean				4550		

Legend:
- Eurasia
- North America
- South America
- Africa
- Australia
- Antarctica

Figure 2-3: Geologic time scale
*time referencing millions of years (Hogervorst, Bouma, & Vos, 2009)

14
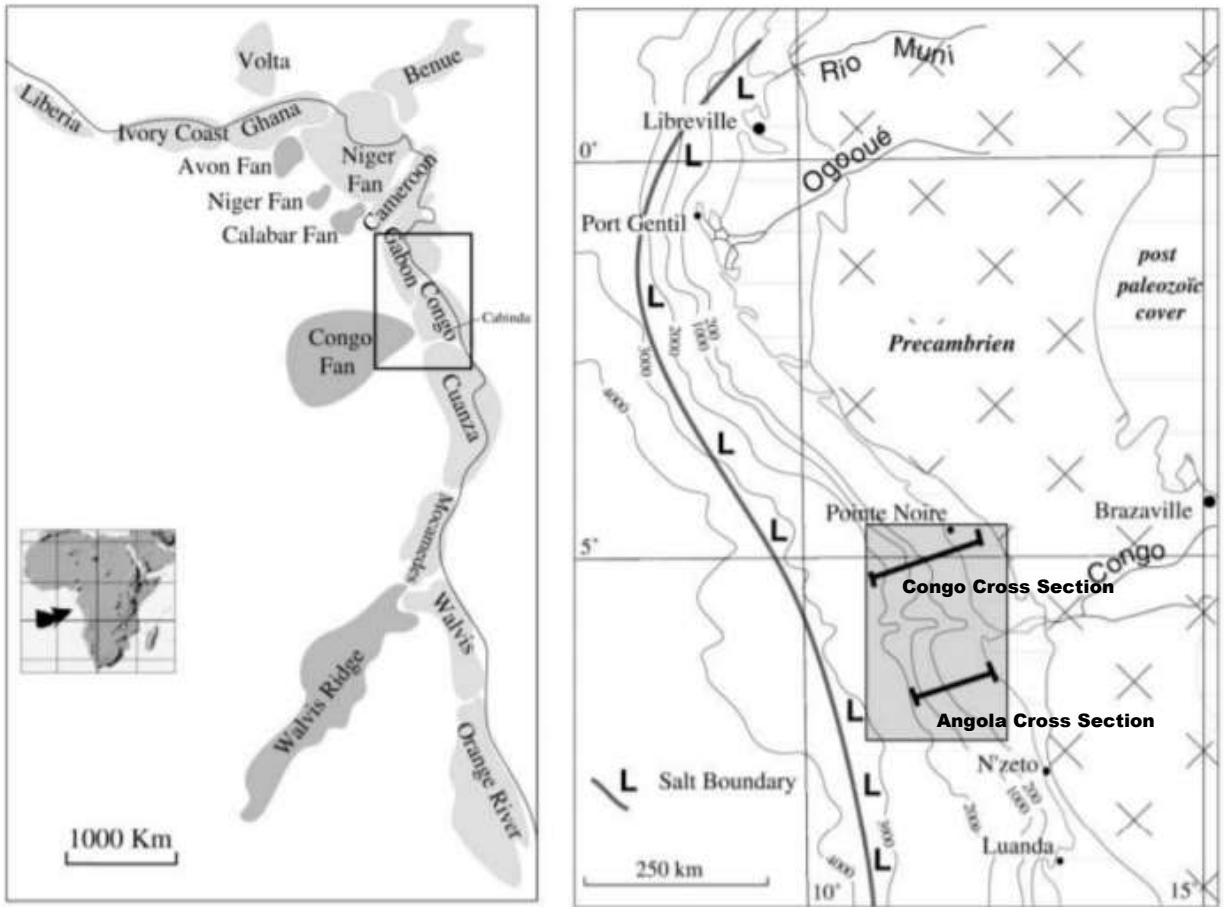
Figure 2-4: Location of Angola cross section
(Lavier, Steckler, & Brigaud, 2001)
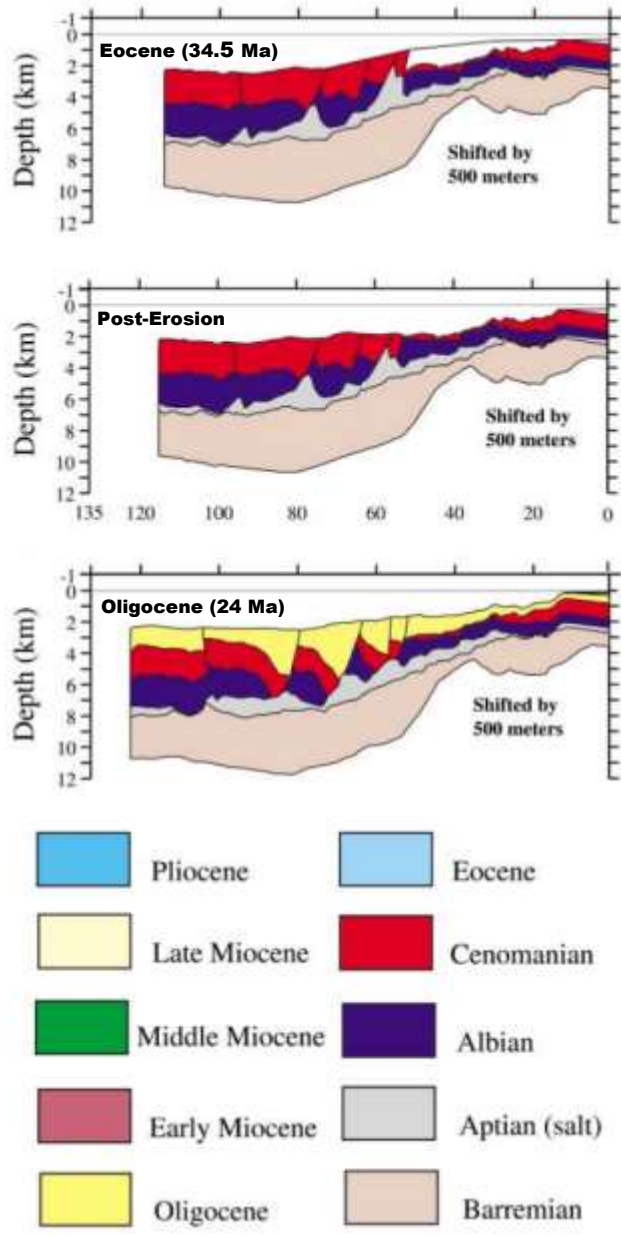
Figure 2-5: Angola cross section: 34.5 – 24 Ma
(Lavier, Steckler, & Brigaud, 2001)
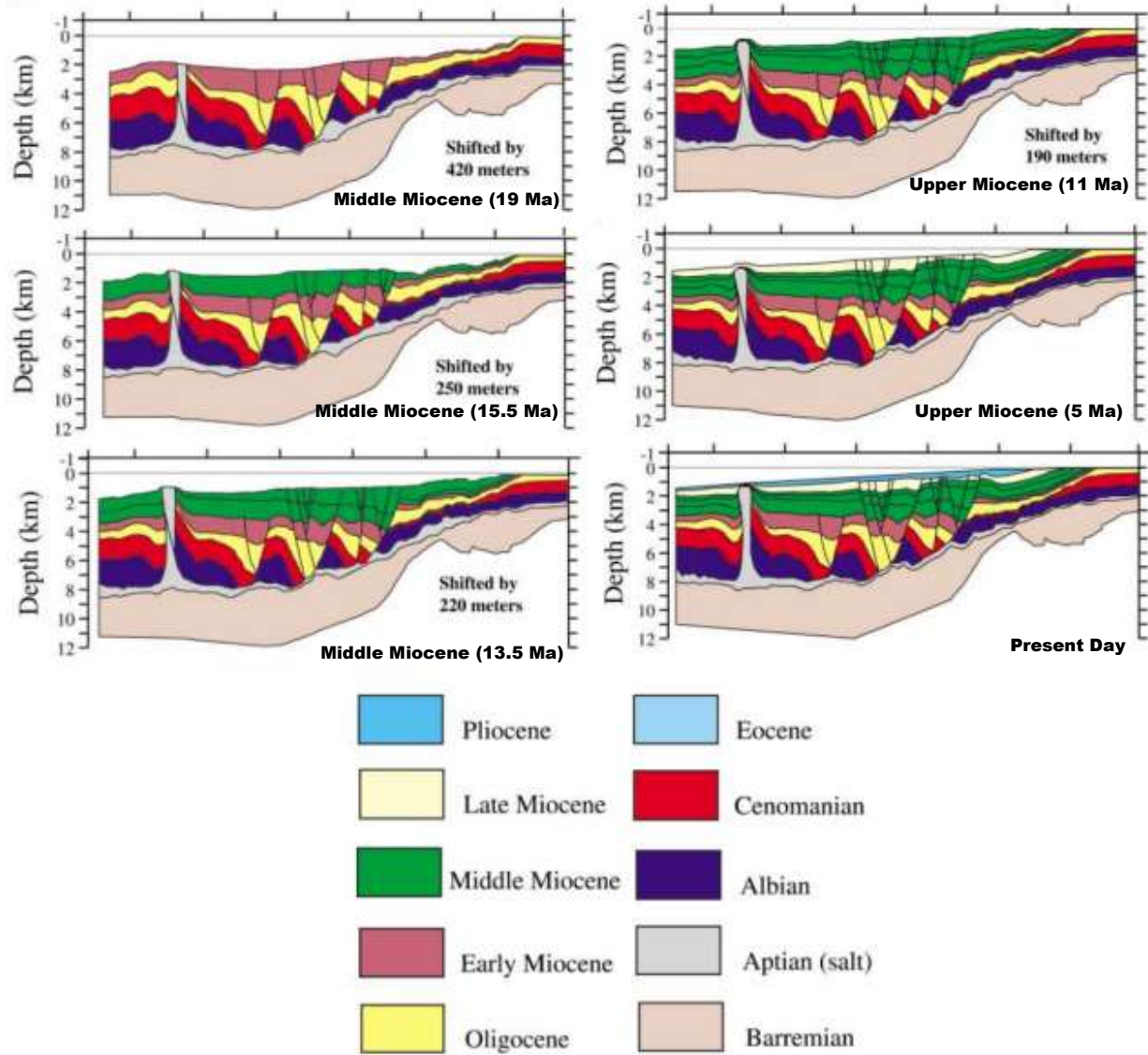
Figure 2-6: Angola cross section: 19 Ma – present day
(Lavier, Steckler, & Brigaud, 2001)

A   Late Paleogene/ Early Neogene

B   Late Neogene

C   Early Quaternary

D   Late Quaternay
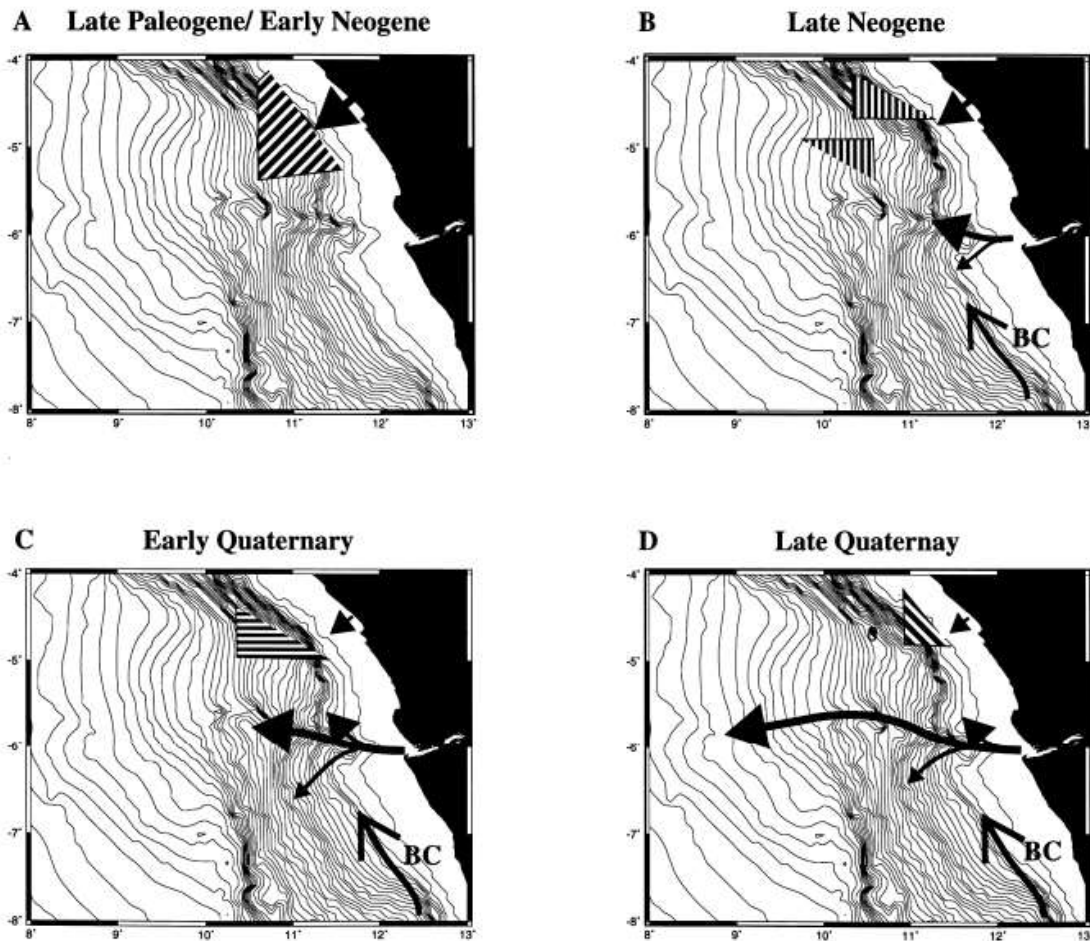
Figure 2-7: Model for the evolution of deposition in the Congo Fan since the late Paleogene (Uenzelmann-Neben, 1998)
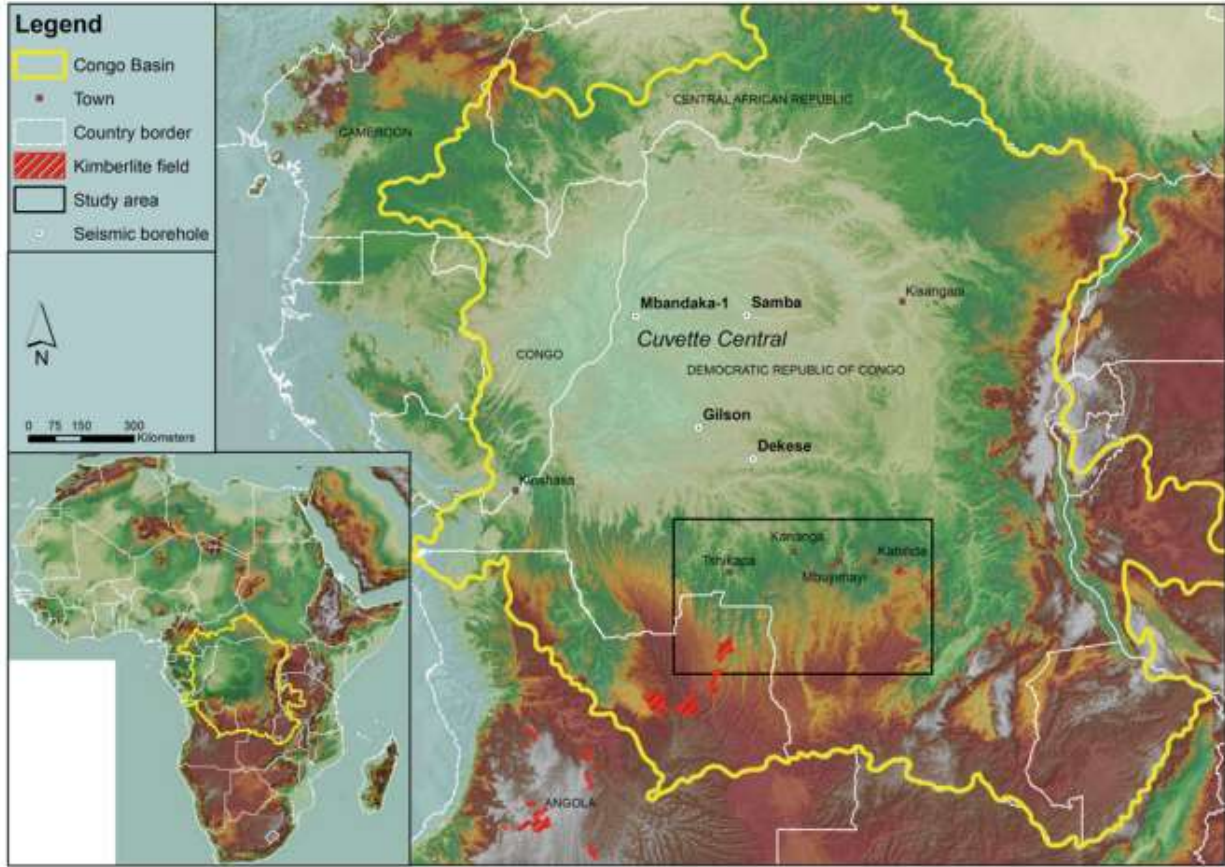
Figure 2-8: Congo Basin map
(Roberts, Jelsma, & Hegna, 2015)
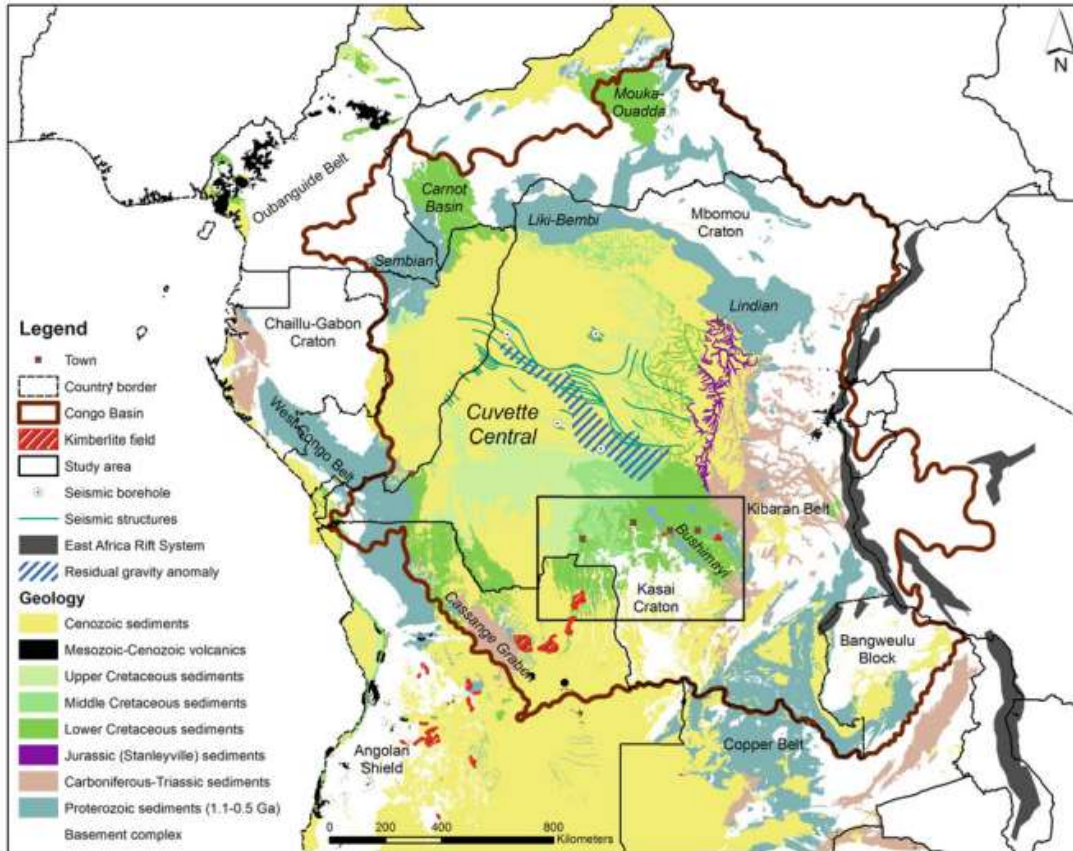
Figure 2-9: Simplified geologic map of the Congo Basin
(Roberts, Jelsma, & Hegna, 2015)
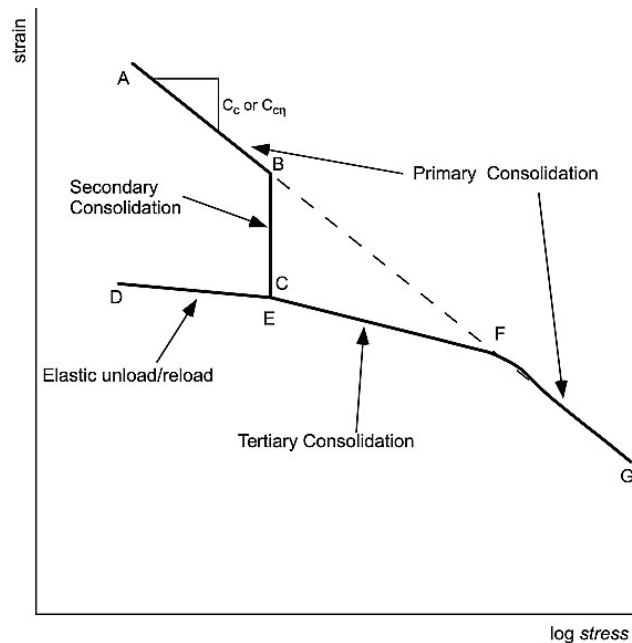
Figure 2-10: Schematic plot of consolidation scheme proposed by Karig & Ask (2003)
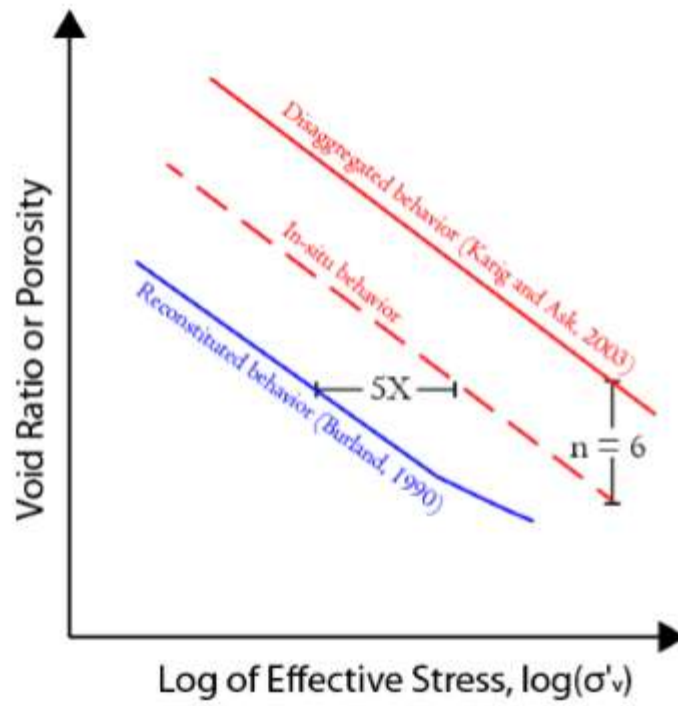
Figure 2-11: Schematic of disagreement in previous comparison literature (Betts, 2014)

3 SPECIMEN PREPARATION AND TESTING PROGRAM

3.1 INTRODUCTION

Laboratory tests on fine-grained soils can be grouped into three main categories: index tests, shear tests, and compression tests. Index tests are used to characterize and classify the material based on physical properties. Compression tests measure the compressibility and permeability of the soil. Shear tests measure the strength and failure envelope of the soil. This chapter reviews the testing program and specimen preparation techniques used for this research.

Section 3.2 describes the naming convention used to refer to lab specimens in this thesis. Section 3.3 describes the processing methods developed for non-preserved samples in this research. Section 3.4 describes the resedimentation method for creating test specimens. Section 3.5 gives a background on the intact specimens used in this research and the method used to prepare them. Section 3.6 details the laboratory testing program for this research.

3.2 SPECIMEN NAMING CONVENTION

Chevron delivered several feet of non-preserved Gulf of Guinea Mudrock core to the Tufts Advanced Geomaterials Laboratory for testing (Figure 3-1). Two sections of the non-preserved material were removed for testing. Resedimented Gulf of Guinea mudrock specimens are referred to as RGoG. The first was an 8-inch section of core referred to as Series I (RGoG-I). It was removed, air dried, ground, and homogenized for a pilot testing program. The second was a 16-inch section referred to as Series II (RGoG-II). It was removed, air dried, ground, and homogenized for testing as part of this research. Material used for Series I and Series II is shown in Figure 3-2. The remaining material in the cores is known as Series III (RGoG-III). It was removed and stored in a bucket for future testing. This thesis presents results from tests on resedimented specimens from both Series I and Series II.

Chevron sent six intact CRS specimens and three intact triaxial specimens to the Tufts lab for testing. The specimens were cut from a preserved intact core, whose insitu moisture content was preserved. Intact Gulf of Guinea mudrock specimens are referred to as GoG. The intact specimens were retrieved from similar depths and locations to the non-preserved core.

3.3 NON-PRESERVED SAMPLE PREPARATION

3.3.1 Background and Rationale

Intact samples are collected and tested in a way that maintains the insitu state of stress and structure of the soil. Although intact samples best represent the natural soil, obtaining them can be difficult and costly, especially for deep or offshore samples. Sampling and transportation can be costly and result in unintentional disturbance of the samples. Therefore, it is sometimes more practical to use resedimentation to systematically study a soil. Resedimentation, described in detail in Section 3.4, allows for control over stress history and porosity, which ensures accurate testing results. The samples for this research were prepared for resedimentation using the methods described below.

3.3.2 Primary Processing

Non-preserved samples were received from Chevron as pictured in Figure 3-1. The samples were retrieved from 4162–4164 feet and 4167–4173 feet. A hammer and chisel were used to break about 4 kg of the sample out of the core barrel to be used for this research. The portion of the sample used for this research is referred to as Series II. Next, the sample was passed through a disk grinder (Figure 3-3) twice to produce a uniform powder, a method referred to as primary processing.

3.3.3 Secondary Processing

Evaluation of the primary processed material under a microscope (

Figure 3-4) shows intact clay aggregates. Most of the material settles out of water within 30 seconds (Figure 3-6), which means a high fraction of the material is coarse-grained. These observations indicate that the disk grinder used for primary processing did not break apart the clay aggregates. Typically, primary processing is enough to prepare a sample for resedimentation, but a secondary processing method was developed for this research to break apart the clay aggregates and sufficiently prepare the sample for resedimentation.

The secondary processing method consists of forming a slurry with 80 g/L salt water that is then circulated through a shear pump to fully break apart the clay aggregates. The salt water is formed by weighing and mixing appropriate portions of distilled water and sea salt acquired from Whole Foods. The slurry was formed by combining the ground sample with salt water in a jar then adding ceramic beads and shaking overnight in a wrist action shaker (Figure 3-7). The wrist action shaker reduces the size of the particles in the ground sample so as not to clog the shear

pump. Once the slurry has been formed, it is circulated through the shear pump thoroughly to ensure that all clay aggregates are broken up. Figure 3-8 shows the shear pump circulation apparatus. The shear pump works by spinning a rubber blade that contacts the metal housing (Figure 3-9). The blade circulates the material while rubbing it against the metal, which shears the material in a similar manner as rubbing it between an index finger and a thumb. About 20 to 30 minutes of circulation through the shear pump is generally enough to fully disaggregate the clay. A simple check to ensure that the clay is disaggregated can be performed by looking at the coarse fraction of the material under a microscope. The coarse fraction can be separated by mixing a small fraction of the slurry with distilled water in a beaker (Figure 3-6). The beaker is shaken with a wrist action while covered, then the coarse fraction settles for 30 seconds. The liquid is decanted from the top and the coarse fraction remains at the bottom of the beaker for inspection. If clay aggregates are visible (

Figure 3-4), then more circulation through the shear pump is necessary. If only quartz particles and no clay aggregates are visible (Figure 3-5) then no more circulation through the shear pump is necessary.

3.4   RESEDIMENTATION

3.4.1   Background

Resedimentation is the process of one-dimensionally consolidating a dilute, deaired clay slurry in a rigid-walled cylindrical tube, known as a consolidometer (Figure 3-10). Resedimentation was first developed at MIT in the 1960s. The early method produced partially saturated, large diameter soil cakes that were divided into smaller samples for individual tests (Ladd & Varrallyay, 1965). A back pressure of 200 kPa was required to fully saturate the samples. The procedure was subsequently modified by Germaine (1982) to produce fully saturated samples that did not require back pressure saturation. The process was further modified by Seah (1990) to improve the efficiency of sample production, provide more uniform samples, and allow for continuous monitoring through remote data acquisition.

Abdulhadi (2009) introduced a new resedimentation procedure by reducing the diameter of the consolidometer to produce individual test specimens. The smaller diameter reduced the required loads to be applied to a specimen to achieve a given stress level. Abdulhadi's method was modified by Hanley (2017), who developed a device like a syringe with which one individual can place the slurry in the consolidometer. This method eliminated the need for two people to place the slurry, reduced wasted slurry, and allowed the use of slurries with lower water contents.

3.4.2 Process

Hanley's method details the process of resedimenting a sample that begins as a dry clay powder. The secondary processing method described in section 3.3.3 yields a wet slurry, so Hanley's method was adapted for use with slurry as described below.

(i)   Hydration, Deairing, and Deposition

Leave he slurry to hydrate for 24 hours after the end of secondary processing. After hydration, place the slurry in a sealed container and exposed to a vacuum to remove any entrapped air. Draw the deaired slurry into the syringe device through a funnel attached to the spout. Then, tremie the slurry into the consolidometer, which contains a porous stone lined with filter paper at the bottom. Place the consolidometer in a container of water mixed to the desired salt content, 80 g/L sea salt for this research, to maintain full saturation. Fill the top of the consolidometer with distilled water periodically, frequently enough so that the liquid never fully evaporates, to prevent desiccation from the top of the specimen.

(ii)   Consolidation

After deposition, place a porous stone with filter paper on top of the slurry. The porous stones on top and bottom of the slurry allow for double drainage, and therefore faster consolidation. Then load the specimen incrementally using a Load Increment Ratio (LIR) of one. Maintain each load increment until at least the end of primary consolidation, usually approximately two days, before the addition of the next increment. Continue the loading process until the specimen reaches the target vertical stress. Once the target stress is reached, allow the specimen additional time for at least one cycle of secondary compression under the target stress, then unload to an OCR of 4 in one increment. At an OCR of 4, the clay is assumed to be close to hydrostatic stress conditions, which means K_0 is equal to one. Under these conditions, shear strains from sample extrusion and trimming are minimized (Santagata M. C., 1994).

(iii)   Extrusion and Preparation

After consolidation and unloading to an OCR of 4, the specimen is ready for testing. Samples resedimented below 1 MPa can be extruded manually, and a hydraulic jack is used to extruded higher stress samples. Samples are then trimmed and prepared for testing as described in further detail in Chapter 4.

3.5 INTACT SPECIMENS

3.5.1 Background

Chevron sent six intact specimens for CRS testing and three intact specimens for triaxial testing to the Tufts Laboratory. The CRS specimens are from depths 4166.5–4166.75 feet. The triaxial specimens are from depths 4165.65–4166.0 feet. These specimens were cut from preserved core, which is assumed to maintain its insitu moisture content. The samples were received from Chevron wrapped and dipped in rubber coating, as shown in Figure 3-11.

3.5.2 Preparation

The intact samples were hydrated in a vacuum desiccator (Figure 3-12) containing a super-saturated salt solution. A solution at room temperature is considered super-saturated if it contains a higher concentration of a dissolved compound than the solubility concentration of that solid. The creation of a super-saturated solution takes advantage of the increased solubility of most compounds with increased temperature. The solution for this research was created by heating distilled water near its boiling point and stirring in the desired salt until the concentration was higher than the solubility concentration. The salt was stirred in progressively and allowed to dissolve completely. Once the solution cools it is super-saturated. The salt solution was used to set the relative humidity of the air in the desiccator, and in turn, saturate the samples. The relative humidity values produced by various salts present in the Tufts lab are listed in Table 3-2. The procedure for saturation in the vacuum desiccator is summarized below:

1. Place the super-saturated salt solution at the bottom of the closed desiccator for several days prior to introducing the specimen to let dissolved air escape from the solution.
2. After sitting for several days, vacuum the desiccator until it boils to remove any remaining air.
3. Weigh the container tare, then weigh the specimen and container tare, and place them into the desiccator.
4. Attach the desiccator valve to a vacuum and apply for no more than five minutes to remove air from the chamber. Cut off the vacuum if the specimen appears to be drying out.
5. Close the desiccator valve to lock in the vacuum.

6. Weigh the specimen periodically (once per week) to determine when it has reached equilibrium.

7. Repeat steps 3 and 4 after weighing to re-establish the vacuum in the desiccator chamber.

The desiccator should remain in a temperature-controlled location for this process. A super-saturated sodium-tartrate solution is used to obtain 92% relative humidity in the desiccator. A super-saturated potassium phosphate monobasic solution is used to obtain 96% relative humidity in the desiccator.

3.6 TESTING PROGRAM

3.6.1 Index Tests

Index properties are related to engineering behavior that help classify a soil and provide indicators to mechanical behavior. The following index tests were performed for this research:

- Grain Size Distribution
- Atterberg Limits
- Specific Gravity
- Natural Salt Content
- X-Ray Diffraction (XRD) Mineralogy

The methods for performing these tests are detailed in Section 4.2. The results of these tests are discussed in Section 5.2.

3.6.2 Mercury Porosimetry

Chevron performed mercury injection capillary pressure (MICP) tests on both intact and resedimented CRS specimens to evaluate the pore size distribution. The tests are summarized below, as well as in Table 3-1.

Two tests were run on Series I material that had undergone primary processing only: one test was on a specimen compressed to 10 MPa, and the other was on a specimen that was compressed to 35 MPa. Five tests were run on Series I material that had undergone secondary processing: one test was on a specimen that was compressed to 10 MPa, three tests were on specimens that were compressed to 35 MPa, and one test was on a specimen that was

compressed to 100 MPa. One test was run on an intact specimen retrieved from 4225 feet below mud line, which had an estimated effective overburden of 9.5 MPa.

The methods for performing MICP tests are summarized in Section 4.3. The results of the tests are detailed in 5.3.

3.6.3 CRS Compression Tests

Constant Rate of Strain (CRS) Consolidation tests were performed to determine the compressibility and permeability properties of the material over a range of 0.1 to 100 MPa. A total of 10 CRS tests were performed as part of this research. The tests are summarized below, and specifics for each test are available in Table 3-1.

The first CRS tests performed for this research were low stress tests on primary processed Series I RGoG. Next, low stress tests were performed secondary processed Series I RGoG to compare the effects of primary and secondary processing. High stress tests were then run on both primary and secondary processed Series I RGoG. After the Series I tests, Series II RGoG was processed and prepared for testing. Low and high stress tests were performed on Series II RGoG. Finally, high stress test was performed on a preserved intact specimen. A total of 10 CRS tests were performed.

The methods for performing CRS tests on resedimented specimens are detailed in section 4.5. The methods of performing CRS tests on intact specimens are detailed in section 4.6. The results of all CRS tests are detailed in sections 5.4 and 5.5.

3.6.4 Triaxial Shear Tests

K_0 consolidated undrained triaxial compression tests were performed to determine the strength properties of the soil over a range of 0.4 to 4 MPa. Four triaxial tests were performed as part of this research. One of the tests was not successful due to a specimen that failed prior to the test, and another was not successful due to a leak during K_0 consolidation. The successful tests are summarized below as well as in Table 3-1.

One triaxial test was performed in the low stress triaxial cell to a maximum stress level of 0.4 MPa on Series II RGoG that had undergone secondary processing. One triaxial test was performed in the medium stress triaxial cell on Series II RGoG that had undergone secondary processing.

29

The methods for performing low stress triaxial tests are summarized in section 4.5.3, and the methods for performing medium stress triaxial tests are summarized in section 4.5.4. The results of both triaxial tests are detailed in section 5.6.

Test Type	Test Number	Stress Level (MPa)	Series	Processing
CRS	CRS1551	10	I	Primary
CRS	CRS1553	35	I	Primary
CRS	CRS1556	35	I	Secondary
CRS	CRS1557	10	I	Secondary
CRS	CRS1588	100	I	Primary
CRS	CRS1589	100	I	Secondary
CRS	CRS1590	100	I	Primary
CRS	CRS1599	10	II	Secondary
CRS	CRS1610	100	II	Secondary
CRS	CRS1615	100	Intact	NA
Triaxial	TX1445	0.4	II	Secondary
Triaxial	TX1450	1	II	Secondary
Triaxial	TX1455	4	II	Secondary
Triaxial	TX1458	1	II	Secondary
MICP	CRS1551	10	I	Primary
MICP	CRS1553	35	I	Primary
MICP	CRS1588	100	I	Primary
MICP	CRS1556	10	I	Secondary
MICP	CRS1557	35	I	Secondary
MICP	CRS1588	100	I	Secondary
MICP	CRS1590	100	I	Secondary
MICP	-	9.5	Intact	NA

Table 3-1: Summary of Engineering Tests
Note: tests highlighted in red were unsuccessful

Salt	RH in Super-saturated Solution (%)
Sodium Tartrate	92
Potassium Phosphate Monobasic	96
Copper Sulfate	98

Table 3-2: Relative humidity of supersaturated solution based on salt type
(R. Ewy, e-mail correspondence, November 20, 2019)

Figure 3-1: Non-preserved core samples as received in the Tufts Laboratory from Chevron
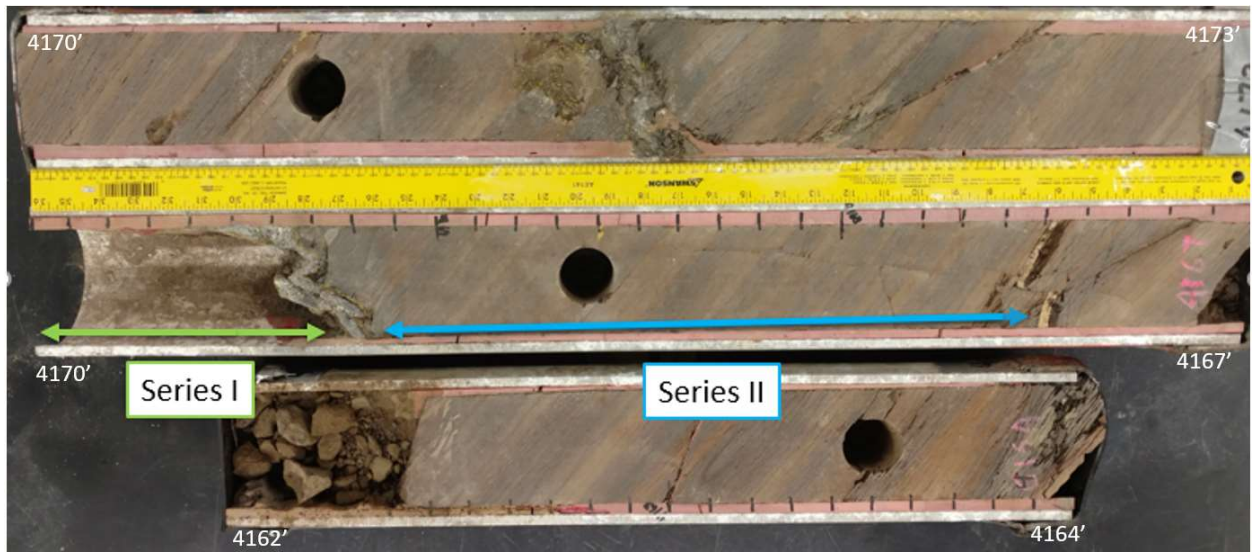
Figure 3-2: Non-preserved core, depths and locations of Series I and Series II material noted
Note: Series III is the remaining fine-grained material in the cores and is being stored for future testing

Figure 3-3: Disk grinder

Figure 3-4: Primary processed material with intact clay aggregates
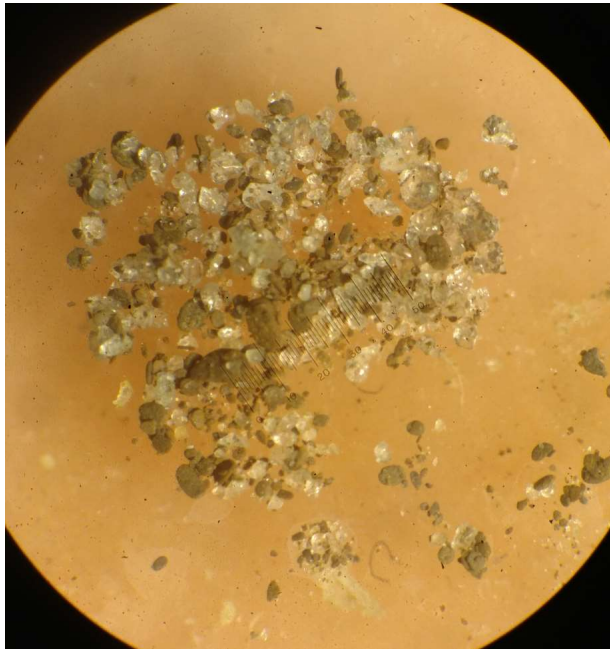
Figure 3-5: Coarse fraction of secondary processed material

Figure 3-6: Primary processed material fast settling rate
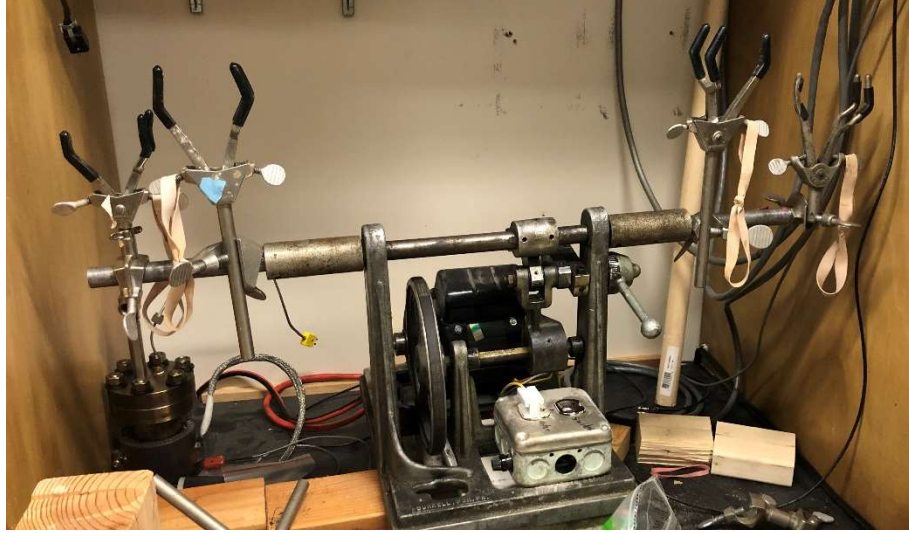
Figure 3-7: Wrist action shaker

Figure 3-8: Shear pump circulation apparatus
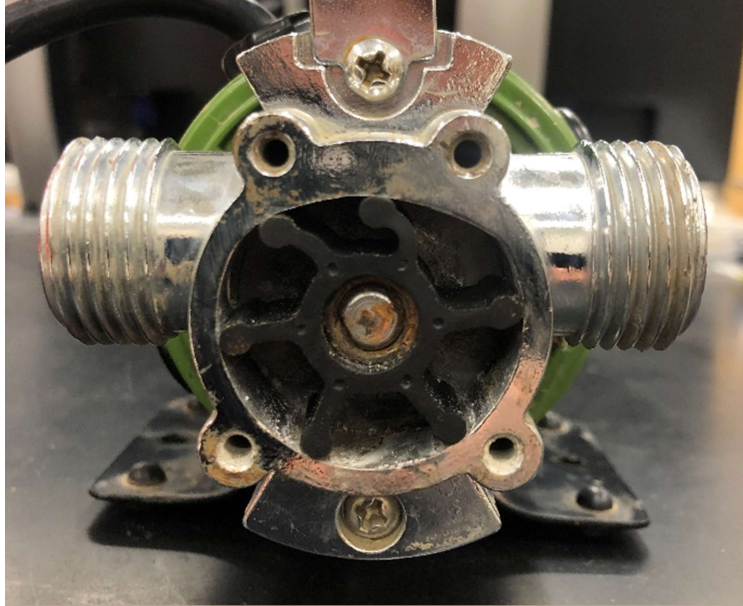
Figure 3-9: Closeup of the inside of the shear pump

Figure 3-10: Resedimentation consolidometer

Figure 3-11: Intact samples as received from Chevron

Figure 3-12: Vacuum desiccator used for saturating intact samples

4   LAB TESTING EQUIPMENT AND METHODS

4.1   INTRODUCTION

The goal of this research is to classify the new Gulf of Guinea mudrock material based on index tests, and to compare resedimented behavior to intact behavior. This chapter describes laboratory testing methods used in this research, as well as the equipment used for them.

Section 4.2 describes the index testing procedures used to classify the material. Section 4.3 summarizes the methods for mercury porosimetry tests used to evaluate the pore size distribution of the material at various stress levels. Section 4.4 describes the electronic instrumentation and data acquisition system used for automating the tests and collecting data. Section 4.5 describes the equipment and procedures for triaxial and CRS tests on resedimented specimens. Section 4.6 describes the equipment and procedures for triaxial and CRS tests on intact specimens.

4.2   INDEX TESTS

4.2.1   Grain Size Distribution

The grain size distribution of the soil was determined by two methods of sedimentation tests: hydrometer and pipette. Sedimentation tests are used to determine the grain size distribution of fine-grained soils. No coarse-grained material remained in the soil after secondary processing, so mechanical sieving was not necessary for grain size analysis.

The hydrometer test measures the density of fluid containing the soil in suspension over time as the particles settle. The specific gravity of the fluid is measured with the hydrometer, and the fluid temperature is measured at the same time to calculate viscosity. Stokes Law is used to approximate the diameter of particles remaining in suspension and the fluid density measured by the hydrometer is used to calculate their mass. According to Stokes Law, the terminal velocity of a smooth, spherical particle falling through the fluid is proportional to the diameter of the particle squared (Germaine & Germaine, 2009). The full procedure for the hydrometer test can be found within ASTM D7928.

The pipette test measures the dry mass of samples of soil taken at specified times from a constant depth within a fluid containing the soil in suspension. The test method specified in Head (1980) was modified for use in this research. The specific gravity and temperature of the fluid

were measured at the same time pipette samples were taken, and the following equations were used to calculate percent finer and particle diameter:

$$\rho_{f,T} = R_H \cdot \rho_{w,20°C}$$ 4-1

where: $\rho_{f,T}$ = density of fluid at reading temperature (g/cm³)

R_H = hydrometer reading

$\rho_{w,20°C}$ = density of water at 20°C (0.9982 g/cm³)

$$V_p = \frac{m_{wet}}{\rho_{f.T}}$$ 4-2

where: V_p = actual volume of pipette sample (cm³)

m_{wet} = wet mass of pipette sample (g)

$$N_m = \frac{\left(\frac{m_{dry}}{V_p} \cdot 1000 - m_{disp}\right)}{m_{total}} \cdot 100\%$$ 4-3

where: N_m = percent finer at reading m (%)

m_{dry} = dry mass of pipette sample (g)

m_{disp} = mass of dispersant (g)

m_{total} = total dry mass (g)

$$D = \sqrt{\frac{18}{\rho_{f,T}g(G_s - 1)} \cdot \frac{H}{t}} \cdot 10$$ 4-4

where: μ = dynamic viscosity of the fluid (g-sec/cm²) calculated by using correlations to temperature measurements in Germaine & Germaine, 2009

g = acceleration due to gravity (980.7 cm/s)

G_s = specific gravity of the soil

H = fall distance of particles (cm)

t = time (s)

Exactly 5.00 g of sodium hexametaphosphate dispersant is added to the specimens for both the hydrometer and the pipette tests to completely break up the clay flocs into their individual particles and ensure accurate results. The addition of dispersant to fully break up the clay flocs also ensures that grain size results would be consistent between primary and secondary processing.

4.2.2   Atterberg Limits

Atterberg Limits are boundaries in material behavior for fine grained soils that are defined by water content. They were developed by Dr. Arthur Atterberg in 1911 to classify agricultural soils and were later standardized for index testing in geotechnical applications (Casagrande A. , 1932). Most soils in their natural state exist between the liquid and plastic limits, so those are the most used in geotechnical engineering. The liquid and plastic limit testing procedures are fully described in ASTM D4318.

The liquid limit is defined as the water content at which the soil transitions between plastic and fluid behavior. The liquid limit test uses a Casagrande device (Figure 4-1) and grooving tool (Figure 4-2). The soil is placed in the cup to fill the same volume that water would while in the drop position, then the grooving tool is used to cut a uniform groove down the center of the soil. The number of drops (blows) from a height of 10 mm required to close 13 mm of the groove is recorded at least three times, and the soil is progressively dried for each reading. Ideally, all readings are between 15 and 35 blows because the relationship between water content and blow count is linear within that range (Germaine & Germaine, 2009). The data are plotted on a liquid limit flow curve (Figure 4-3) with blows on the x-axis as a log scale, and water content on the y-axis as a linear scale. The liquid limit is calculated as the water content corresponding to closure at 25 blows, obtained with a linear best fit line through the data points.

The plastic limit is defined as the water content at which the soil transitions between plastic and semi-solid behavior. The plastic limit test involves rolling a thread of the soil on a grooved glass plate (Figure 4-4) to dry it out. The soil has reached the plastic limit when the thread crumbles at a diameter of 3.2 mm. The plastic limit is the average water content of at least three threads that crumble at a diameter of 3.2 mm.

Once the liquid and plastic limits of a soil are known, the plasticity index can be calculated, and the soil can be classified according to the Unified Soil Classification System (USCS). The plasticity index is the difference between the liquid limit and the plastic limit. Liquid limit, plastic limit, and plasticity index are typically reported as integers. The liquid limit is plotted versus the plasticity index on the Casagrande Chart to obtain a USCS classification of the soil. If the natural water content is known, the liquidity index can be calculated as well using the following equation:

$$LI = \frac{w_c - PL}{PI} \qquad\qquad 4\text{-}5$$

where: LI = Liquidity index (decimal)

w_c = natural water content (%)

PL = plastic limit (integer value without a percent symbol)

PI = plasticity index (integer value without a percent symbol)

Other Atterberg limits, such as the fluidization limit and the shrinkage limit, exist but were not tested as part of this research. Other methods for determining the liquid and plastic limits exist, such as the fall cone method, but those methods were not used.

4.2.3 Specific Gravity

Specific gravity of a material is defined as the ratio of the density of that material to the density of distilled water at 20°C. Accurate specific gravity results are important for phase relationship calculations and other testing procedures. Several methods exist for measuring specific gravity. The water pycnometer and gas pycnometer methods were used in this research.

The water pycnometer method is appropriate for measuring the specific gravity of nonreactive particles that are denser than water (Germaine & Germaine, 2009). It involves measuring the mass of a soil sample submerged in a flask (Figure 4-5) containing distilled water. The volume of the flask is calculated by measuring the mass of the flask when it is filled with only distilled water at a constant temperature. Then the mass and temperature of the flask and submerged soil is measured several times. The flask is stored under controlled temperature conditions between measurements to ensure a uniform temperature. The relationship between the mass of the soil and volume of water displaced by it can be used to calculate the specific gravity.

42

The full procedure for the water pycnometer specific gravity test can be found within ASTM D854.

The gas pycnometer method is appropriate for measuring the specific gravity of a variety of substances, including those that contain materials that are water soluble. It was used in conjunction with the water pycnometer method to obtain results without the interaction of the clay double layer with the experimental water. The test involves measuring pressure in a container with the soil when a known volume of gas is injected into the container. The pressure increase is related to the volume of the sample, and the specific gravity can be obtained from the dry mass and volume of the specimen. The full procedure for the gas pycnometer method can be found within ASTM D5550.

4.2.4 Salt Content

The surfaces of clay particles are electrically charged, and at least a portion of the strength of most clays is derived through long range electrical forces. Therefore, the chemistry of the pore fluid plays an important role in the mechanical behavior of fine-grained soils. Pore fluid chemistry also affects the clay structure during deposition. (Lambe & Whitman, 1969)

Accurate salt content results are important for field representative resedimented specimens, correct pore fluid salinity during triaxial and CRS tests, and accurate phase relations calculations. The salt content of a soil sample is usually represented as grams of salt per kilogram of dry soil. Fine-grained soil samples do not need to be intact for salt content measurements, provided that the soil has not been leached or the chemistry otherwise altered during transport. (Germaine & Germaine, 2009)

Several methods involving separating the pore fluid from the soil and measuring its salinity are common, including gravimetric measurements, refraction measurements, and conductivity measurements (Germaine & Germaine, 2009). ASTM D4542 is a standard method for measuring salt content by refraction, but accuracy and range are low. Conductivity measurements were used to determine salt content in this research. The procedure, adopted from Germaine & Germaine (2009), is as follows:

1. Obtain a representative water content measurement for the soil to be tested
2. Measure the mass of a centrifuge test tube and cap.

3. Add approximately 25g of wet soil to the test tube.

4. Measure the mass of test tube, cap, and wet soil.

5. Add approximately 20g of distilled water to the test tube.

6. Measure the mass of the test tube, cap, wet soil, and water.

7. Shake the test tube vigorously for approximately 1 minute.

8. Place the test tube in a centrifuge and spun at 5000 rpm for 30 minutes.

9. Decant the supernatant liquid from the test tube into a small beaker.

10. Measure the conductance of a reference salt solution (1g/L) with a conductance probe.

11. Clean the probe with distilled water and dry.

12. Measure the conductance of the supernatant.

13. Clean the probe with distilled water and dry.

14. Repeat steps 9-11 two more times and average the conductance measurements.

15. Normalize the conductivity of the supernatant liquid to the reference solution and calculate the salt concentration

Figure 4-6 shows the calibration curve used for the conductance probe in this research. The salt concentration is calculated using the process summarized below. The first step is to calculate the salinity of the supernatant using the equation from the calibration curve:

$$SS = 10^{[log_{10}\left(\frac{C}{C_0}\right)+0.0184]/0.9332} \qquad \text{4-6}$$

$where\ SS = salinity\ of\ supernatant\ fluid$

$\quad C = measured\ conductivity\ of\ supernatant\ fluid$

$\quad C_0 = conductivity\ of\ reference\ solution$

Then the salt content of the soil per unit dry mass is calculated:

$$s = \frac{SS * \left(\frac{m_w}{100}\right)}{\frac{m_s}{1000}} \qquad \text{4-7}$$

$where\ s = salt\ per\ dry\ mass\ (g/kg)$

$\quad m_w = mass\ of\ water\ (g)$

$\quad m_s = mass\ of\ dry\ soil\ (g)$

Obtaining an accurate, representative water content measurement of the soil to be used in the test is important because it is used to estimate the mass of water and mass of dry soil in the equation above.

4.2.5 Mineralogy

Approximately 40 grams of secondary processed Series II material was air dried and ground into a powder with a mortar and pestle for mineralogy testing by X-Ray powder diffraction (XRPD). Half of the material was sent to the James Hutton Limited Institute's Clays and Minerals Laboratory in Aberdeen, U.K. and the other half to Chevron's Briarpark Laboratory in Houston, Texas. XRPD can be used to identify many crystalline substances, such as minerals. It involves bombarding the sample with electrons and recording the response spectra to identify the minerals present and their relative percentages within the sample. Clay mineral XRPD was performed on the portion of the sample smaller than 0.002 mm in diameter to identify the clay minerals present, and bulk XRPD was performed on a portion of the whole sample.

4.3 MERCURY POROSIMETRY

RGoG specimens were sent to Chevron for Mercury Porosimetry testing. The specimens were compressed CRS specimens. Each specimen was cut in half after compression. One half was oven dried in the Tufts lab, and the other half was packaged in a plastic bag within another plastic bag that contained a paper towel to preserve the moisture. Seven total CRS specimens were sent to Chevron for testing. The test specimens and their stress levels are available in Table 3-1. Chevron also provided results for Mercury Porosimetry tests on intact specimens retrieved from a similar location and stress level.

Mercury Porosimetry involves injecting mercury into an oven dried specimen at incrementally higher pressures. The amount of mercury that enters the pore space is measured at each pressure increment, and those measurements can be used to calculate the incremental pore throat radius and cumulative porosity of the specimen.

The test method is inherently biased because oven drying a fine-grained specimen collapses the double layer and causes significant shrinkage, so the pore structure of the specimen during the test is different from the pore structure before oven drying. However, the oil industry

still depends on mercury porosimetry results to provide insight into the pore structure of the materials they work with.

4.4 ELECTRONIC INSTRUMENTATION

Electronic instrumentation was used to record accurate measurements of displacement, force, and pressure to ensure accurate results and allow for automation in CRS and triaxial tests. Calibrations for force, pressure, and displacement are performed periodically in the Tufts lab against a reference standard. Each calibration is performed with a measured input voltage. During testing, a local DC power supply provides power for all instrumentation for a single test. The input voltage is recorded along with the measurements from each device, and the measurement is then normalized to the input voltage.

Electronic instrumentation discussed in this section includes LVDTs, string potentiometers, load cells, pressure transducers, pressure volume actuators (PVAs), the central data acquisition, and computer control for triaxial and CRS tests.

4.4.1 Linear Variable Differential Transformers (LVDTs)

LVDTs are electric transformers used to measure linear displacement. They have two parts: a ferrous core and a cylindrical barrel. They operate by creating a magnetic field inside of the cylindrical barrel that is distorted proportionally to displacement as the ferrous core enters the inside of the barrel. The output is then measured and calibrated to a reference displacement. The LVDTs used in this research have a linear working range of slightly more than 2 cm. Outside of the linear range, displacement is not directly proportional to output voltage, and the linear calibration factor no longer applies. LVDTs used for this research have a resolution of approximately 0.04 mm.

4.4.2 String Potentiometers

String potentiometers are also used to measure linear displacement. They contain a cable wrapped around a constant diameter spool and a rotational potentiometer. As the end of the cable is displaced, the spool rotates, and the potentiometer creates an electric signal proportional to the displacement of the cable.

String potentiometers have a linear range within the range of displacement of the devices used. They are also DC rather than AC devices, which reduces the impact of electrical noise.

Both attributes provide and advantage over LVDTs when measuring large displacements. String potentiometers used in this research have a resolution of approximately 0.07 mm.

4.4.3 Load Cells

Various load cells were used in this research, depending on the testing apparatus and the maximum expected load. The load cells employ an S-shaped steel shear beam that deforms elastically when loaded. Strain gauges within the load cell measure the deflection of the beam and output voltage is proportional to the load.

4.4.4 Pressure Transducers

Pressure transducers of various capacities were used to measure pore pressure and cell pressure during CRS and triaxial tests for this research. Pressure transducers consist of a metal diaphragm of known area and strain gauges. As pressure is exerted on the metal diaphragm, it deforms elastically, and the strain gauges measure its deflection. Output voltage is proportional to the pressure.

4.4.5 Pressure Volume Actuators

Pressure volume actuators (PVAs) are used to control fluid pressure for both cell and pore fluid in CRS and triaxial apparatuses. The PVAs were designed and fabricated in house. They are also used to measure pore fluid volume change in the triaxial apparatus. They consist of a piston sealed in a rigid tube, a fluid reservoir, and a computer-controlled motor to move the piston. As the piston moves, fluid is forced in or out of the tube, controlling the pressure based on a feedback loop established by the computer and a transducer measuring the pressure. The position of the piston is measured with an LVDT or string potentiometer, which can be calibrated to measure fluid volume change.

4.4.6 Central Data Acquisition System

The central data acquisition system (Figure 4-7) in the Tufts lab allows for accurate collection of measurements from transducers to be used in final calculations for all CRS and triaxial tests, as well as device calibrations. The system consists of an auto ranging analog to digital (A/D) converter capable of reading voltage scales for all the laboratory electronic instrumentation, a laboratory wide multiplexer that allows the data acquisition system to switch between instrumentation channels, and a computer to store the data and perform scheduling for

47

the A/D converter. Once a task is scheduled, the data acquisition system reads outputs from the electronic instrumentation for the test, independent of the computer control for that test.

4.4.7 Computer Control System

The triaxial and high stress CRS apparatuses used for this research are automated using a computer control system that was initially developed by Sheahan (1991) and modified by Casey (2014). Test parameters including axial force, axial displacement, cell pressure, pore pressure, and pore volume change are measured using transducers. The output from each transducer is converted to a digital signal using a local A/D converter and sent to a computer running a control program written in QuickBASIC. The user interface for a testing apparatus in the laboratory is shown in Figure 4-8. The program can control all phases of a triaxial test: pressure up, back pressure saturation, K_0 consolidation or stress path consolidation, and shearing. The program operates via a feedback loop that compares actual transducer readings to target values for the current test phase, then determines the corrective action to bring the reading to a target value. The program uses either intermittent proportional or continuous proportional integral differentiation (PID) control to generate a digital signal that is sent to a D/A converter. The analog signal from the D/A converter is sent to a custom control box (Figure 4-9) that drives one of three motors to adjust either the cell pressure, pore pressure, or axial load continuously and precisely throughout the test. The computer control system is described in greater detail within Casey (2014) and Sheahan & Germaine (1992).

4.5 TESTS ON RESEDIMENTED SPECIMENS

4.5.1 Low Stress CRS Tests

Low stress CRS tests for this research were performed using a Trautwein CRS device (Figure 4-10) with manual control. The CRS procedure was first developed by Smith and Wahls (1969). It is a more efficient method of determining the consolidation parameters of a specimen compared to the incremental consolidation test because it is less labor-intensive. The test also allows for studying the strain rate sensitivity of soils. The procedure was improved by Wissa (1971) who added the ability to back pressure saturate specimens in the apparatus prior to loading and measure pore pressures at the base of the specimen during the saturation process. The full procedure is detailed in ASTM D4186 as well as Parry (2018), and it is summarized in the following steps:

(i) Specimen Trimming and Preparation

Extrude approximately one inch of the resedimented specimen from its consolidometer and cut using a wire saw. Place the specimen on top of a piece of wax paper on the plastic disk of the trimming device (Figure 4-11). Center the specimen below the confining ring (Figure 4-12), and advance the ring evenly through the specimen while scraping the trimmings away. Cut excess material from the confining ring using a wire saw and save for a water content measurement. Smooth the top and bottom of the specimen with a razor blade. Next, measure the mass of the specimen and ring. The weight of the ring is later subtracted to obtain the initial wet mass. Measure the depth of the specimen into the ring. The total height of the ring is later subtracted to obtain the initial height of the specimen.

(ii) Cell and Load Frame Set Up

After the specimen is trimmed, place filter papers and porous stones on its top and bottom. Clean all cell components, and clean and grease all O-rings prior to assembly. Center the confining ring in the base of the cell with a square O-ring at its base. Place the cell chamber and top cap with the piston secured in its retracted position onto the base and secure by tightening the nuts onto the threaded rods attached to the base. Record the load cell zero before the CRS cell contacts the load cell. Place the LVDTs and record zeros. Place the CRS cell in the load frame and secure the piston in contact with the porous stone on top of the specimen. Place a moment and shear break on top of the piston and adjust the load frame piston until it contacts the break. Fill the cell with water, 80 g/L for this research, using a screw pump (Figure 4-13) connected to a reservoir. Record cell pressure and pore pressure zeros while the cell is connected to atmospheric pressure.

(iii) Back Pressure Saturation

Apply a constant cell pressure of 400 KPa using a manual air pressure regulator (Figure 4-14) and air to water pressure converter. Use the voltage meter to determine the correct pressure to apply. Once the cell has reached the target pressure, leave it for at least 24 hours to come to equilibrium. The piston remains locked in place during this step to prevent swelling, and all drain lines remain open.

(iv)   CRS Loading

After back pressure saturation, load the specimen at a constant rate of strain. Close the bottom valve, isolating the pore pressure transducer to read the pore pressure at the base of the specimen. Set the load frame to the desired strain rate and direction and turn the motor on. Monitor the test closely at the beginning to ensure that the load frame is loading in the right direction at the desired rate. Continue loading at the constant rate while the data acquisition system takes readings at a specified rate, usually 15 to 30-minute intervals. Loading continues until the desired maximum stress level is reached. For this research, the desired maximum stress level coincided with the capacity of the load cell. Monitor the load cell reading closely at the end of the test so as not to exceed its capacity.

(v)   Disassembly

No unloading was performed as part of this research, so the next step after CRS loading was disassembly. Disassembly starts by depressurizing the cell and unloading the specimen with the piston locked in place to reduce swelling. Disassemble the chamber, wipe excess water off of the ring, and determine the wet mass of the ring and the specimen. Extrude the specimen from the confining ring to be oven dried and weighed. Clean and dry the cell components to prevent corrosion.

(vi)   Calculations

The excess pore pressure at the base of the specimen during the test is used to calculate the effective stress and hydraulic conductivity of the specimen throughout the test. Excess pore pressure is the difference in the base pore pressure reading and the cell pressure reading. Those calculations, from ASTM D4186, are summarized below:

$$\sigma'_{a,n} = \left(\sigma_{a,n} - \frac{2}{3}u_{m,n}\right)$$
4-8

$where: \sigma'_{a,n} = axial\ effective\ stress\ at\ time\ n$

$\quad\quad \sigma_{a,n} = reduced\ axial\ total\ stress\ at\ time\ n$

$\quad\quad u_{m,n} = base\ excess\ pore\ pressure\ at\ time\ n$

$$\sigma_{a,n} = \sigma_{measured,n} - u_{back,n} \tag{4-9}$$

$where: \sigma_{measured} = stress\ measured\ by\ transducer\ at\ time\ n$

$\quad u_{back,n} = back\ pressure\ at\ time\ n$

$$u_{m,n} = u_{base,n} - u_{back,n} \tag{4-10}$$

$where: u_{base,n} = base\ pressure\ measured\ by\ transducer\ at\ time\ n$

$$k_n = \frac{1}{2} \frac{\dot{\varepsilon}_n H_n H_0 \gamma_w}{u_{m,n}} \tag{4-11}$$

$where: k_n = hydraulic\ conductivity\ at\ time\ n$

$\quad \dot{\varepsilon}_n = strain\ rate\ at\ time\ n$

$\quad H_n = drainage\ height\ of\ the\ specimen\ at\ time\ n$

$\quad H_0 = starting\ drainage\ height\ of\ the\ specimen\ (starting\ specimen\ height)$

$\quad \gamma_w = unit\ weight\ of\ water$

$$H_n = H_0 - \Delta H_n \tag{4-12}$$

$where: \Delta H_n = change\ in\ specimen\ height\ at\ time\ n$

$$\Delta H_n = \left(\delta_n - \delta_{af,n} - \delta_{ap,n} \right) \tag{4-13}$$

$where: \delta_n = axial\ deformation\ of\ specimen$

$\quad \delta_{af,n} = apparatus\ compressibility\ due\ to\ net\ axial\ force, equations\ in\ appendix$

$\quad \delta_{ap,n} = apparatus\ compressibility\ due\ to\ chamber\ pressure$

The coefficient of consolidation is calculated using the hydraulic conductivity and the volume compressibility in the calculations summarized below:

$$c_{v,n} = \frac{k_n}{m_{v,n} \gamma_w} \tag{4-14}$$

$where: c_v = coefficient\ of\ consolidation\ at\ time\ n$

$\quad m_{v,n} = volume\ compressibility\ at\ time\ n$

$$m_{v,n} = \frac{\varepsilon_{n+1} - \varepsilon_{n-1}}{\sigma'_{a,n+1} - \sigma'_{a,n-1}}$$

4-15

where: $\varepsilon_{n+1}; \varepsilon_{n-1} = axial\ strain\ (\%)\ at\ time\ n+1;\ n-1$

$\sigma'_{a,n+1}; \sigma'_{a,n-1} = axial\ effective\ stress\ at\ time\ n+1;\ n-1$

Axial strain and void ratio are tracked throughout the test in order to create a compression curve. They are calculated using the following equations:

$$\varepsilon_n = \frac{H_0 - H_n}{H_0} \times 100\%$$

4-16

where: $\varepsilon_n = axial\ strain\ (\%)\ at\ time\ n$

$$e_n = \frac{H_n - H_s}{H_s}$$

4-17

where: $e_n = void\ ratio\ at\ time\ n$
$H_s = equivalent\ height\ of\ solids$

$$H_s = \frac{V_s}{A}$$

4-18

where: $V_s = volume\ of\ solids$
$A = specimen\ area$

The voltage readings from the transducers during the test are recorded by the central data acquisition system. A QBASIC program, titled CRSQB3B, is used to convert the voltages into engineering values of axial displacement, load, cell pressure, and pore pressure. This program can reduce data from both low stress and high stress CRS tests. The engineering values are then used to calculate effective stresses and strains.

4.5.2   High Stress CRS Tests

The procedure for testing resedimented specimens in the high stress CRS cell (Figure 4-15) is similar to that of the low stress cell. The high stress CRS setup was designed, machined, and built at MIT. Details of the load frame design are available in Ge (2019). The load frame was custom made to withstand stresses up to 100 MPa. The device is operated by a hydraulic jack and force measurements are carried out by a load cell, each of which have capacity above 100 MPa. It is made of stainless steel and is capable of testing in high salinity and medium

temperature environments. Parry (2018) used the cell to perform medium temperature CRS tests, but all CRS tests for this research were performed at room temperature.

The cell is computer controlled, with a program similar to the triaxial control program described in section 4.4.7 that was modified by Ge (2019) for CRS testing. The program is capable of back pressure saturation, constant rate of strain loading, constant gradient loading, and creep at a constant stress level. The cell pressure is controlled by a motor connected to the PVA and automated instead of by a manual air pressure system. Back pressure saturation is automated using the computer control. The hydraulic jack is driven by a PVA that allows for automating CRS loading to a specified stress level (usually 95 MPa) with the computer control program. A maximum pore pressure gradient is specified. Once the pore pressure gradient threshold is reached during CRS loading, the computer control automatically switches to constant gradient loading which maintains the pore pressure gradient. The test is carried out under the constant gradient condition until the maximum stress level is reached.

The trimming and cell set up procedures remain the same as the low stress procedure, with the difference being that the cell is filled with water from the cell PVA instead of a screw pump. The calculations for the CRS portion of high stress tests are the same as the calculations for low stress CRS tests. However, the apparatus has a different compressibility, which must be accounted for correctly. The constant gradient calculations, developed by Lowe (1969), are described below:

$$k_n = \frac{c_v \gamma_w a_v}{1 + e_0} \qquad\qquad 4\text{-}19$$

$where: c_v = coefficient\ of\ consolidation$
$\qquad H_d = drainage\ height$
$\qquad a_v = coefficient\ of\ compressibility$

$$a_v = \frac{\Delta e}{\Delta \sigma} \qquad\qquad 4\text{-}20$$

$$c_v = \frac{\Delta \sigma_v}{\Delta t} \frac{H_d{}^2}{2\Delta u} \qquad\qquad 4\text{-}21$$

4.5.3 Low Stress CK$_0$UC Triaxial Tests

Low stress triaxial tests were performed in a clear acrylic triaxial cell capable of cell pressures up to 1 MPa. The tests are automated using the program described in section 4.4.7. The standard procedure for consolidated undrained triaxial compression tests is described in detail in ASTM D4767 as well as in Zablocki (2018), and that procedure is summarized in the following steps:

(i)   Specimen Trimming

Extrude the resedimented specimen from the consolidometer and cut with a wire saw. Triaxial specimens are approximately 8 cm tall and 3.5 cm in diameter. Cut the specimen to slightly higher than the desired height and place in the trimming device (Figure 4-16). Trim the specimen first with a wire saw, and weigh and air dry the trimmings for water content measurements. Then trim the specimens with a razor. Rotate the specimen during trimming to ensure that it remains a perfect cylinder. After trimming the sides of the specimen, wrap it in wax paper and place it in a metal jacket. Cut the top and bottom with a wire saw and smooth with a razor. Measure the initial diameter, height, and wet mass of the specimen.

(ii)   Cell Setup

Place nylon filters on the top and bottom of the specimen and place moist porous stones on each of the filters. Place the specimen, filters, and stones on the pedestal of the triaxial cell, on which thin rubber membranes and three O-rings have already been positioned. Unlubricated condoms are used for membranes for low stress tests. Position two O-rings on the pedestal between the inner membrane and the outer membrane, and position one on top of the outer membrane, sitting between the two others to create a tight seal. Once the specimen is in place, roll the membranes up over the specimen, and place three more O-rings on the top pedestal in the same manner. Position the LVDT and measure the zero value. Manually adjust the cell displacement until the moment and shear breaks are lightly contacting the load cell. Measure the zero value of the load cell. Once the specimen is in place and sealed, assemble the cell (Figure 4-17) and fill it with silicon oil.

(iii)   Pressure Up

After the cell is set up, measure zero values for the cell pressure and pore pressure and set up the computer control program for the test. Next, pressurize the cell until a slight positive pore pressure is generated. This usually requires a cell pressure of approximately ¼ of the maximum past stress and provides a record of the sampling effective stress. Maintain the cell pressure overnight.

(iv)   Back Pressure Saturation

After pressure up, back pressure saturate the specimen at the sampling effective stress by increasing cell pressure and back pressure incrementally by the same value. The final pore pressure at the end of back pressure saturation should be at least 0.2 MPa. The back pressure drives any air molecules in the specimen or the drainage lines into solution and leaves the specimen fully saturated. Full saturation is essential to accurately calculating effective stress.

Leave the specimen to equilibrate for 24 hours after the final pressure increment is applied. Check the Skempton B-value after the specimen equilibrates to confirm that the specimen is saturated. The B-value parameter is described within Skempton (1954), and can be defined by the following equations:

$$B = \frac{\Delta u}{\Delta \sigma_{oct}} = \frac{1}{1 + n\frac{C_w}{C}} \qquad \text{4-22}$$

$where: \Delta\sigma_{oct} = change\ in\ octahedral\ stress$
$\qquad \Delta u = resultant\ change\ in\ pore\ pressure$
$\qquad n = porosity$
$\qquad C_w = compressibility\ of\ pore\ fluid$
$\qquad C = compressibility\ of\ soil\ skeleton$

A B-value of almost exactly 1 implies full saturation for a soft clay, because the compressibility of the pore fluid is several orders of magnitude smaller than that of the soil skeleton. That is not the case for stiffer clays and mudrocks because the soil skeleton compressibility is comparable to the pore fluid compressibility. A detailed discussion of the dependence of B-value on soil compressibility is available in Casey (2014). For low stress triaxial tests, a B-value of 0.95 or higher is required to ensure that the specimen is fully saturated and to move on to K_0 Consolidation.

(v)   K$_0$ Consolidation

K$_0$ consolidation allows for control of the stress state of the specimen and ensures that it is normally consolidated prior to shearing. K$_0$ consolidation is performed by the computer control program. The specimen is compressed vertically at a specified strain rate, 0.15% per hour for this research, and the control program adjusts the cell pressure to maintain a constant cross-sectional area. K$_0$ consolidation most accurately represents the consolidation process for insitu soils. Other consolidation methods are stress path and hydrostatic, but they were not used as part of this research.

After K$_0$ consolidation is completed, hold the specimen at constant stress for one log cycle of secondary compression. At the end of the secondary compression phase, perform a leak check by closing the drainage lines for at least five minutes and monitoring pore pressure. If the pore pressure remains constant during the leak check the specimen is ready to be sheared.

(vi)   Undrained Shear

During undrained shear, the computer controls axial strain rate while the cell pressure is kept constant. The axial strain rate for undrained shear is typically 0.5% per hour, and excess pore pressure within the specimen is measured. Only undrained shear tests were performed for this research, so the drainage lines were closed prior to shearing.

(vii)   Disassembly

After shearing is completed, drain the cell, and remove the specimen. Weigh and oven dry the specimen. Dry and clean the cell components to prevent corrosion. Store the stones in water in a closed container.

(viii)   Calculations

All calculations required to determine the results from the shear phase of the triaxial test are summarized below.

The height and cross-sectional area of the specimen at the end of consolidation are determined based on the following equations:

$$H_C = H_0 - \Delta H_0 \qquad\qquad 4\text{-}23$$

where: H_c = *height of specimen at the end of consolidation*

H_0 = *initial height of specimen*

ΔH_0 = *change in height at the end of consolidation, measured by LVDT*

$$A_c = \frac{V_0 - \Delta V_{sat} - \Delta V_c}{H_c} = \frac{V_{wf} + V_s}{H_c} \qquad\qquad 4\text{-}24$$

where: A_c = *cross sectional area of specimen at the end of consolidation*

V_0 = *inital volume of specimen*

ΔV_{sat} = *change in volume of specimen during saturation*

ΔV_c = *change in volume of specimen during consolidation*

V_{wf} = *final volume of water*

V_s = *volume of solids*

The specimen is assumed to maintain its right-cylindrical shape during consolidation. The cross-sectional area of the specimen can be calculated under the right-cylindrical assumption for any load during the consolidation process using the following equation:

$$A = \frac{A_c}{1 - \varepsilon_l} \qquad\qquad 4\text{-}25$$

where: A = *cross sectional area for a given applied axial load*

ε_l = *axial strain (decimal) for the given applied axial load*

During and after undrained shear, the cross-sectional area of the specimen is calculated using the following parabolic area correction, which was developed specifically for undrained conditions (Germaine & Ladd, 1988):

$$A_{parabolic} = A_c \left[-\frac{1}{4} + \frac{\sqrt{25 - 20\varepsilon_a - 5\varepsilon_a^2}}{4(1 - \varepsilon_a)} \right]^2 \qquad\qquad 4\text{-}26$$

where: $A_{parabolic}$ = *corrected cross sectional area for a given axial strain*

ε_a = *axial strain* (%)

The rubber membrane creates a principal stress difference that is accounted for using the following correction equation:

$$\Delta(\sigma_1 - \sigma_3)_m = \frac{4 E_m t_m \varepsilon}{D_c} \qquad \text{4-27}$$

$where\text{:}\ \Delta(\sigma_1 - \sigma_3)_m = membrane\ correction$

$\qquad E_m = Young's\ Modulus\ of\ membrane\ material$

$\qquad t_m = thickness\ of\ membrane$

$\qquad \varepsilon = axial\ strain$

$D_c = \sqrt{4 A_c / \pi}$

The correction can be applied to the measured stresses in order to calculate the corrected principal stress difference:

$$(\sigma_1 - \sigma_3)_c = \frac{P}{A} - (\sigma_1 - \sigma_3)_m \qquad \text{4-28}$$

$where\text{:}\ (\sigma_1 - \sigma_3)_c = corrected\ deviator\ stress$

$\qquad P = applied\ axial\ load$

$\qquad A = cross\ sectional\ area\ corresponding\ to\ applied\ axial\ load$

The voltage readings from the transducers during the test are recorded by the central data acquisition system. A QBASIC program, titled QBTXRED8, is used to convert the voltages into engineering values of axial displacement, load, volume change, cell pressure, and pore pressure. The engineering values are then used to calculate effective stresses and strains. The details of the procedure used in the program are explained in detail in Sheahan (1991).

4.5.4 Medium Stress CK₀UC Triaxial Tests

One medium stress triaxial test was performed for this research. The procedure is similar to the low stress procedure described in section 4.5.3.The test was performed in a triaxial cell with a steel chamber (Figure 4-18) capable of withstanding cell pressures up to 10 MPa. The full procedure for testing in the medium stress triaxial cell is detailed within Casey (2011), and Hanley (2017). The differences between the low stress procedure are summarized here.

The filter papers, porous stones, and drain lines are dry during the cell set up process. Instead of using two condoms as rubber membranes, use two 0.012-inch rubber membranes. Apply the membranes directly to the specimen using a vacuum membrane stretcher. Hold the top

cap in place during this process using an alignment device to keep the specimen vertical and the top cap in position to fit smoothly into the piston. Place two O-rings on the top and bottom pedestals before applying the second membrane, then place a third O-ring between them and on top of the outer membrane, in the same manner as with the low stress test.

After the specimen is sealed, connect the top cap to the drainage line, and use the crane to lower the steel chamber over the specimen. Fill the chamber with oil and pressurize to 0.1 MPa to prevent the specimen from swelling when the drainage lines are filled with water. Vacuum the drainage lines to remove air. Connect a sealed flask filled with water at the desired pore fluid salinity (80 g/L for this research) between the vacuum and the drainage lines. Submerge the line below the surface of the water in the flask to observe if any air bubbles continue exiting the drainage lines after it has been evacuated. If air bubbles continue exiting at a high rate, a leak is present. If the lines have no leaks, release the vacuum, flushing the lines with water. Record the sampling effective stress the following day, and carry out back pressure saturation in the same manner as with the low stress tests. Usually the final pore pressure is 0.5 MPa instead of 0.2 MPa before the B-value check. Medium stress specimens are resedimented to higher stress levels, and therefore stiffer than low stress specimens. A stiffer soil structure means that a lower B-value is expected. A detailed discussion of the dependence of B-value on soil compressibility is available in Casey (2014).

Carry out K_0 consolidation and undrained shear at strain rates of 0.15%/hr and 0.5%/hr, respectively using the computer control program in the same manner as described in section 4.5.3. Disassemble the cell and remove the specimen from the membrane to be oven dried at the end of shear.

4.5.5   Oven Drying

All tests discussed in this section, and many others discussed in this chapter, require oven drying to determine the dry mass of the test specimen. Oven drying in many geotechnical laboratories is considered to be sufficient if the specimen remains in the oven at 105°C overnight. However, the fine-grained specimens tested in this research do not fully dry out in an oven at 105°C for several weeks. Test specimens for this research were removed from the oven

periodically, placed in a glass desiccator to cool, weighed, and placed back in the oven. The final dry weight was recorded as the weight of the specimen when it reached equilibrium, meaning it maintained a constant mass between measurements.

4.6 TESTS ON INTACT SPECIMENS

4.6.1 High Stress CRS Tests

One high stress CRS test was performed on an intact specimen as part of this research. The diameter of the cut specimen was several millimeters larger than that of the confining ring for the high stress CRS apparatus, so trimming the specimen was necessary. Trimming was a more difficult process for the intact specimen than for resedimented specimens. The specimen was much denser than the typical resedimented specimen used for CRS testing, so the usual effort of pushing the confining ring down onto the specimen was not enough to penetrate it. Also, the specimen possessed bedding planes that were liable to fracture if too much force or uneven force was exerted on the specimen. The trimming and cell setup methods are described below:

Use an electric rotary brush with metal bristles to shave the diameter of the specimen down until it fits in the confining ring. Take care not to shave the diameter of the specimen smaller than that of the confining ring, which would allow for unconfined compression and violate the boundary conditions assumed for a CRS test. Shave the specimen from top to bottom and slide the confining ring down progressively as the specimen is shaved. This process uses the same trimming device as the process for resedimented specimens to allow for rotating the specimen to evenly trim it around its circumference. This is a labor-intensive process; it took over an hour to trim the first intact CRS specimen. The trimming procedure resulted in small imperfections in the specimen due to fractures along bedding planes and uneven shaving with the rotary brush.

Vacuum the cell and lines to remove water and prevent swelling during the cell set up process. After the cell is set up and in place, measure the string potentiometer zero values, and apply an axial force of approximately 0.3 MPa to prevent swelling during filling of the cell. Connect a sealed flask with water at the desired pore fluid salinity (80 g/L) to the vacuum lines in the same manner as the medium stress triaxial procedure, discussed in section 4.5.4. Remove the vacuum, flushing the cell with water. Restrain the specimen from swelling with an applied

vertical stress during this process. The remaining test procedure is the same as the procedure discussed in section 4.5.2.

Figure 4-1: Casagrande cup for Liquid Limit Test

Figure 4-2: Liquid limit grooving tool
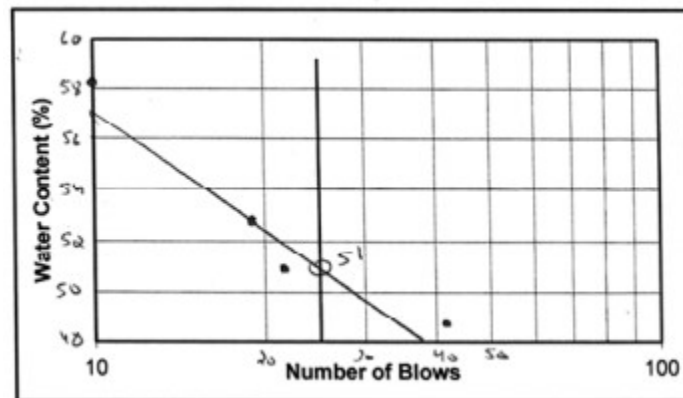
Figure 4-3: Liquid limit flow curve for primary processed material

Figure 4-4: Plastic limit grooved glass plate

Figure 4-5: Specific gravity flask
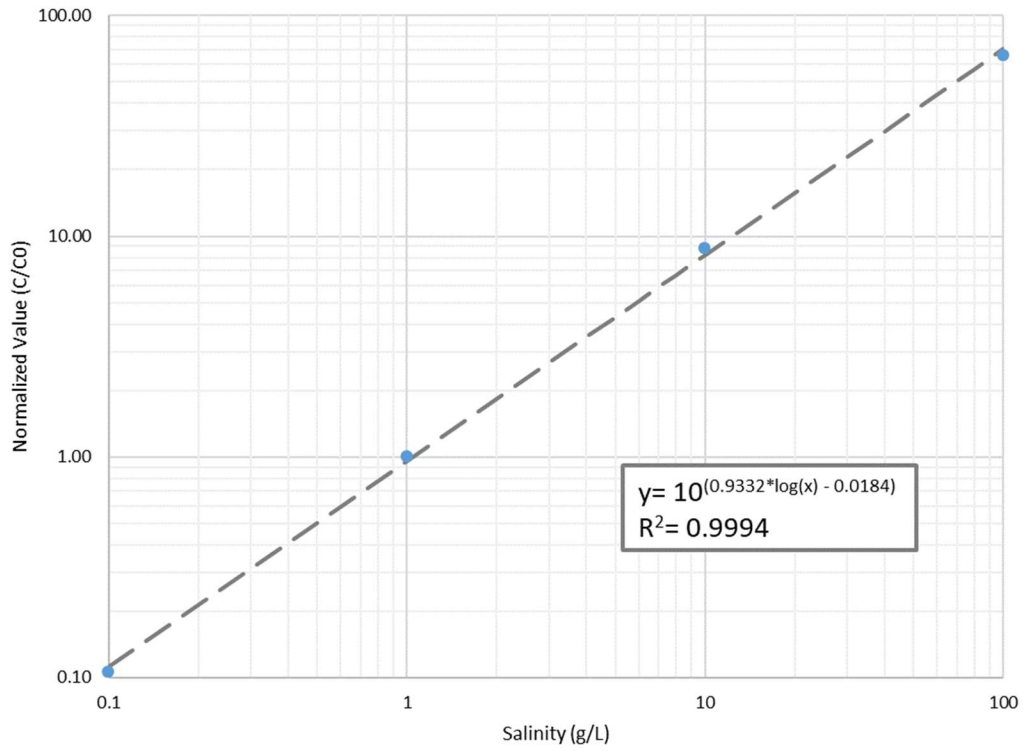
Figure 4-6: Conductance Probe Calibration Curve

Figure 4-7: Tufts central data acquisition system

Figure 4-8: Computer control monitor and user interface

Figure 4-9: Control box
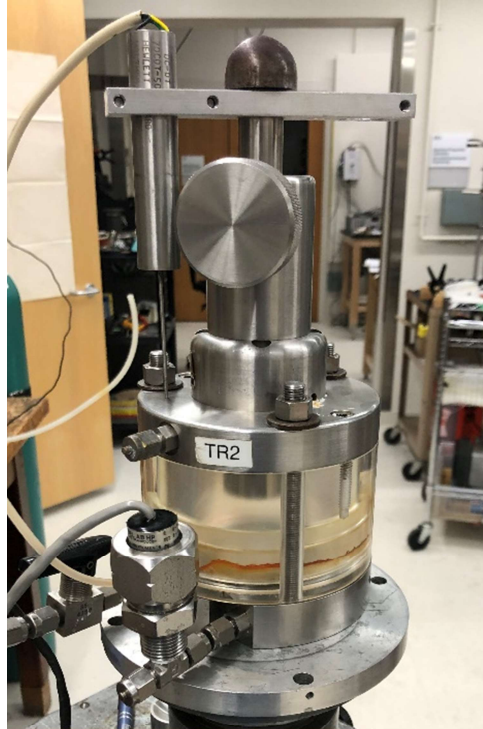
Figure 4-10: Low stress CRS cell
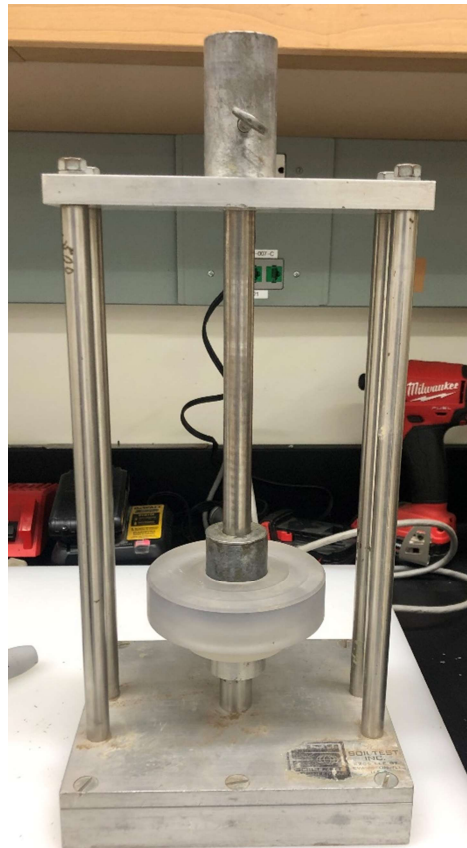
Figure 4-11: CRS trimming device

Figure 4-12: CRS confining ring and recess tool
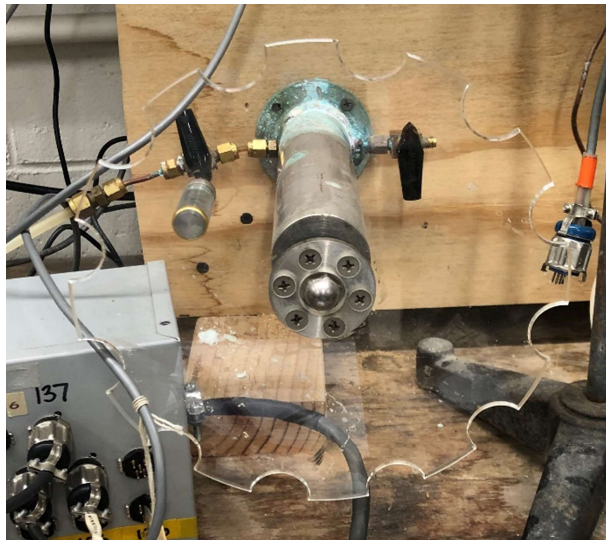
Figure 4-13: Screw pump
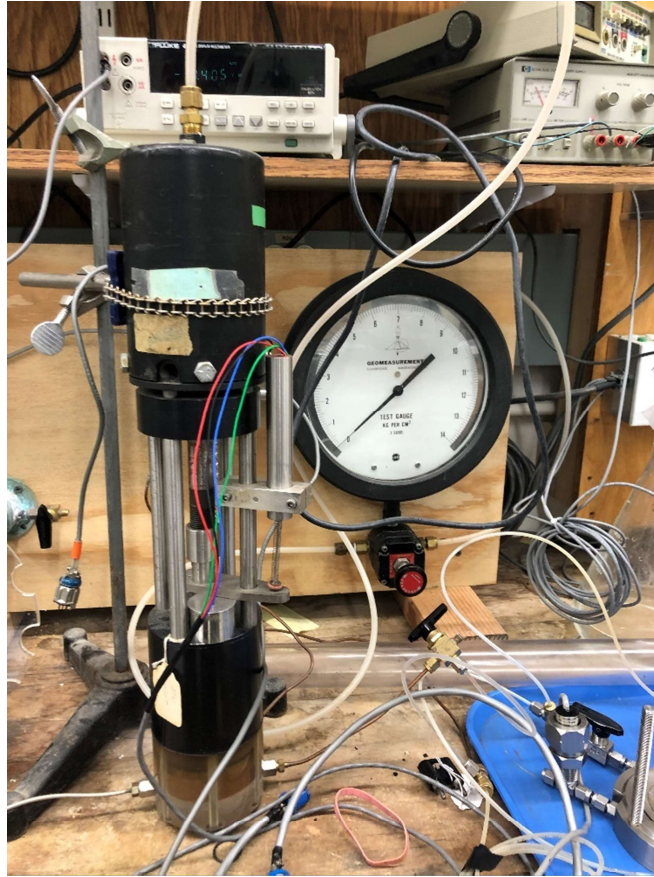
Figure 4-14: Air pressure regulator

Figure 4-15: High stress CRS cell
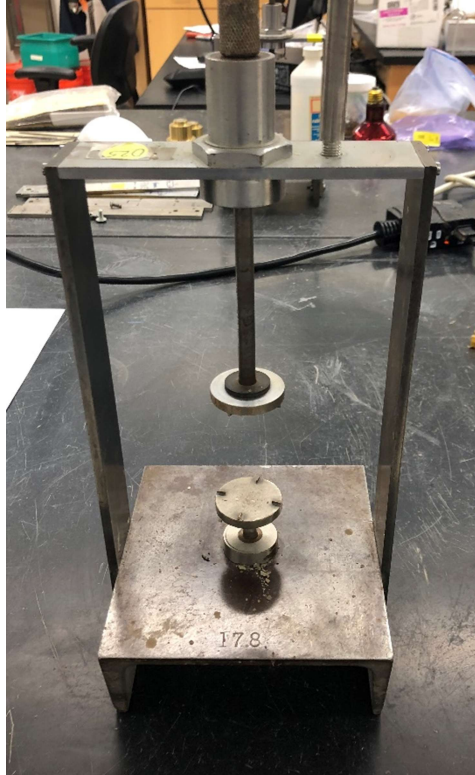
Figure 4-16: Triaxial trimming device

Figure 4-17: Low stress triaxial cell

Figure 4-18: Medium stress triaxial cell

5 TESTING RESULTS

5.1 INTRODUCTION

The Gulf of Guinea mudrock was classified based on its index properties. Then the mechanical properties of RGoG, including compression, permeability, and shear behavior were studied with CRS compression and triaxial shear tests. The compression behavior of intact GoG was studied with a CRS test. Chevron performed mercury porosimetry tests on both resedimented and intact GoG. The results of lab testing are described in this chapter.

Section 5.2 details the results of index tests. Section 5.3 describes the results from Mercury Porosimetry tests. Section 5.4 describes consolidation results from both CRS compression tests and triaxial K_0 consolidation. Section 5.5 describes permeability results from CRS compression tests. Section 5.6 details stress-strain strength results from triaxial shear tests. Each section includes a comparison of resedimented to intact behavior for the properties being discussed in that section, and section 5.7 includes a summary of testing results.

5.2 INDEX TESTS

Index tests were performed to classify RGoG by its appearance and physical characteristics. These tests include mineralogy, grain size distribution, Atterberg limits, specific gravity, and salt content. The results of the tests are summarized in Table 5-1 and described in detail in this section.

5.2.1 Mineralogy

X-Ray diffraction mineralogy tests were performed on samples of this material separately by Chevron and the James Hutton Institute. Interpretation of response spectra to determine the relative mineral percentages was performed by Chevron and Hutton. The results of the tests are summarized in Table 5-2 and Table 5-3. Tests were performed on both the bulk sample of the material, and the clay fraction (less than 2μm diameter). The clay fraction of the material is dominated by kaolinite, with illite and smectite each making up about one quarter of the clay fraction. Clay mineralogy results are summarized in Figure 5-1.

73

The results of the Chevron tests are in Table 5-4 and Table 5-5. The results of the Hutton tests are in Table 5-6 and Table 5-7. The results are comparable. GoG has a clay fraction of approximately 80%, about half of which is kaolinite and the remainder is evenly split between smectite and illite. The Chevron results showed a slightly higher portion of smectite and a slightly higher overall clay fraction. The differences between results are likely because XRD tests are performed on a very small specimen that may not be representative of the portions of minerals present in the whole sample.

Gulf of Guinea Mudrock is the first natural kaolinite material in the Tufts Geomaterials Lab database. The mineralogy of the full database is summarized in Figure 5-2. Kaolinite is typically associated with large particles, small surface areas, and low plasticity behavior. The results described in the following sections demonstrate that the typical assumptions for kaolinite behavior are not true for Gulf of Guinea Mudrock.

5.2.2 Grain Size Distribution

Ten hydrometer tests were performed as part of this research: four tests on primary processed Series I material, four tests on secondary processed Series I material, and two tests on secondary processed Series II material. All hydrometer results are plotted in Figure 5-3. Three of the hydrometer tests had an additional pipette component: one test on secondary processed Series I material and two tests on secondary processed Series II material. The results are plotted and compared to hydrometer tests performed on Series I RGoG in Figure 5-4. The hydrometer test results are consistent between the two Series II trials; however, they show greater than 100 percent finer for particle diameters greater than approximately 0.08 mm. A percent finer greater than 100 is mathematically impossible, which means that the hydrometer results had considerable bias.

The bias could have been caused by the presence of dense water layers surrounding the clay molecules. Soil water density, defined as the ratio of soil water mass to soil water volume, is typically assumed to be equal to that of free water, $\rho_{w,T}$, which is approximately 0.9982 g/cm^3, but that is not always the case, especially in fine grained soils. Structured water is abnormally dense water (greater than 1.15 g/cm^3) around exchangeable cations and mineral surface hydroxyls that is a result of compressive stresses and denser water particle orientation caused by cation hydration, surface hydration, and interlamellar hydration. Currently, no unified theory

74

exists to explain variations in soil water density, and there is little agreement on experimental methods to accurately measure soil water density. (Zhang & Lu, 2018)

The hydrometer test procedure is designed for use with distilled water and dispersant, so dense water molecules that form the layer surrounding the clay particles could have caused the fluid to become denser, resulting in higher than expected hydrometer readings. The pipette tests were performed because the density of the water in the fluid does not impact the results, so the bias seen in the hydrometer test could be avoided.

To assess the validity of the assumption that structured water was increasing the density of the fluid, a spreadsheet (Table 5-8) was used to approximate the equivalent density of free water in the sedimentation cylinder using the following equations:

$$V_{w,l} = m_s A_s h_l f_c * 100^{-4}$$
5-1

$where: V_{w,l} = volume\ of\ surface\ water\ (cm^3)$
$\quad m_s = mass\ of\ solids\ (g)$
$\quad A_s = specific\ surface\ area\ (\frac{m^2}{g})$
$\quad h_l = height\ of\ structured\ water\ layer\ (Angstroms)$
$\quad f_c = clay\ fraction\ (decimal)$

$$m_{w,l} = V_{w,l}\rho_{w,l}$$
5-2

$where: m_{w,l} = mass\ of\ surface\ water\ (g)$
$\quad \rho_{w,l} = density\ of\ surface\ water\ (\frac{g}{cm^3})$

$$\rho_{w,l} = \frac{M_w}{V_{w,f}}$$
5-3

$where: M_w = total\ mass\ of water\ in\ cylinder\ (g)$
$V_{w,f} = equivalent\ volume\ of\ free\ water\ in\ cylinder\ (cm^3)$

Two versions of the calculations were performed for each hydrometer test: one assuming that no dense layer of water exists (i.e. $\rho_{w,l} = \rho_{w,T}$) and another assuming that a dense layer exists (i.e. $\rho_{w,l} > \rho_{w,T}$). The results of each calculation are shown in Figure 5-5. The values of A_s, h_l, and $\rho_{w,l}$ were adjusted for these calculations to provide the closest fit to the true density of free water at the measured temperature. The optimum value of A_s was found to be 500 m²/g, which is higher than expected for kaolinite, but well within the range of natural fine-grained soils

(Lambe & Whitman, 1969). Given the Atterberg limits for RGoG, discussed in the following section, this value is a reasonable assumption. The optimum value of h_l was found to be 5.9 Angstroms. This is approximately the thickness of two water molecules, a reasonable thickness for a double layer (Lambe & Whitman, 1969). The optimum value of $\rho_{w,l}$ was found to be 1.5 g/cm^3, which is about 50% higher than the density of free water but well within the range of possible soil water density values for kaolinite, which has an experimental maximum of 1.68 g/cm^3 (Zhang & Lu, 2018).

The first version of the calculations, with the assumption that no dense layer exists, is the assumption used when calculating percent finer from hydrometer data. Calculations with this method yield densities that are all higher than the density of free water, which gives validity to the hypothesis that dense water is affecting the hydrometer results. The second version of the calculations adjusts for the dense water layer. The weight and volume values of the dense water layer were subtracted from the respective totals of those values for the whole cylinder, then the density of the free water in the cylinder was calculated in the same manner. The results are much closer to the expected density of free water based on the temperature.

Although the results from the second method of calculations are closer, they still vary beyond the range of actual densities of free water for the temperature range. The large variance means that scatter is caused by other issues, possibly including inaccurate hydrometer readings. The calculations performed in Table 5-8 plotted in Figure 5-5 are a test of the concept that dense water is impacting hydrometer results. They indicate that dense water is indeed present in the sedimentation cylinders during the hydrometer test. This phenomenon could cause incorrect hydrometer results in many fine-grained soils, particularly those with large specific surface areas which would allow the volume of dense water to become a significant portion of the total volume. The hydrometer results were insufficient due to the curves being greater than 100% finer at diameters greater than approximately 8 mm, so pipette tests were performed in conjunction with the hydrometers for comparison.

The pipette results are slightly above 100 percent finer for the first set of readings, although not to the extent of the hydrometer results, which could be explained by a slight error in the total dry mass of the samples. Some clay particles adhere to the hydrometer and thermometer after they are taken out of the fluid after a reading. The particles that adhere are never accounted

for in the total dry mass. One reading does not remove a significant amount of material, but the cumulative amount of material removed over the course of both the hydrometer and pipette tests could account for the error in the final dry mass. Errors are also possible when measuring the dry mass of the total specimen as well as each individual pipette mass. The pipette results are considered to be accurate, and the hydrometers are considered to be biased. The clay size percentage is calculated as the percentage of the total mass that is made up of particles smaller than 2 μm. Clay size is used to calculate activity, and it is an important control of the mechanical properties of a soil. The clay size percentages based on the pipette results are indicated in Table 5-1.

Values of percent finer greater than 100 have not been documented within the GeoFluids database, and this phenomenon does not appear to be common for kaolinite clays. However, some other clays do show similar behavior. Typical geotechnical practice for hydrometer curves showing greater than 100 percent finer is to cut off the top portion of the curve greater than 100 percent finer. A comparison of hydrometer and pipette results for these materials shows that this practice is not accurate. The true grain size distribution curve appears to be the result of a shift and compression of the hydrometer curve affected by structured water.

The average particle size of Series II RGoG is slightly smaller than that of Series I RGoG. The clay fractions of Series I and Series II are 62% and 67%, respectively. These values are close enough to be considered nearly identical because only Series II has a pipette reading at 2 μm, but the Series I value was interpolated. Differences could also be caused by slight spatial variation in particle size in the non-preserved core between the locations of Series I and II.

5.2.3 Atterberg Limits

The Atterberg Limits are defined by the water content of a soil at a specific shear strength, described in detail in section 4.2.2. They can be correlated to material behavior properties such as strength and permeability. They were therefore important for this research in comparing the behavior of resedimented material to that of intact material.

Atterberg Limits were tested on several samples of the material. The results are summarized in Figure 5-6. The liquid limit of the Series I material that underwent only primary processing is 51%. That number increased to 79% after the Series I material underwent secondary processing, a large increase that demonstrates the importance of secondary processing

for fully reducing the clay aggregates of this material. The difference in Atterberg limit values between primary processed and secondary processed material shows the importance of processing on the outcome of the test. The secondary processing method breaks up the clay flocs and alters the mechanical behavior of the material. This difference between primary and secondary processing is not present for the grain size tests because the addition of sodium hexametaphosphate dispersant serves to break up the flocs in the same manner, regardless of whether the material has undergone secondary processing or not.

The liquid limit of the Series II secondary processed material increased from the Series I secondary processed material to 87%. The increase in liquid limit from Series I to Series II indicates high spatial variability over a short section of source material core.

Based on the Atterberg limit values, Series I is classified as an elastic silt, and Series II is classified as a high plasticity clay. The measured Atterberg limit values are much higher than expected for a Kaolinitic clay. The typical geotechnical understanding of kaolinitic clays is that they have very low plasticity. Three other synthetic kaolin materials in the GeoFluids database are also plotted in Figure 5-6 for reference. Two of them are classified as low plasticity clays, and the other is a high plasticity silt. All three of their liquid limits and plasticity indices are significantly lower than the secondary processed Series II RGoG. The discrepancy between RGoG and typical kaolinitic clays demonstrates that clay fraction mineralogy is by itself not an accurate predictor of mechanical behavior. This discrepancy could be explained by smaller than normal kaolinite particles, which would have a higher plasticity. It could also be explained by Smectite minerals being interlayered with the Kaolinite minerals in the clay particles and exerting more of an influence on mechanical behavior than their relative percentages of the clay fraction mineralogy would indicate.

Figure 5-7 shows the Atterberg limit values of all other materials in the GeoFluids database compared to Series II RGoG. Several materials in the database are in the high plasticity range similar to RGoG, with Gulf of Mexico Eugene Island (RGoM_EI) and Nile Silty Clay (RNSC) being the closest. London Clay (RLC) and Nankai Clay (RNC) are also comparable. The Atterberg limit values of the materials that are comparable to RGoG are listed in Table 5-9. Their mechanical behavior, including compression, permeability, K_0, friction angle, and undrained shear strength, is compared in subsequent sections.

5.2.4 Specific Gravity

The specific gravity of primary processed Series I RGoG was 2.619 based on the results of the water submersion method. This measurement was compared to the helium gas method, which yielded a result of 2.589. This difference is also likely due to the bound water effect discussed in detail in section 5.2.2.

The specific gravity of secondary processed Series I RGoG was 2.657. The specific gravity of Series II RGoG was found to be 2.668. Both tests on secondary processed material were performed with the water submersion method.

5.2.5 Salt Content

The natural salt content of Series II RGoG was found to be 11.5 grams of salt per kilogram of solid material. This is a high value, which is expected because GoG was deposited in a marine environment. For example, Boston Blue Clay has a salt content of only about 2.7 g/kg (Casey, 2014). The value is comparable to the salt content of Gulf of Mexico Eugene Island Clay, another marine clay, which has a salt content of approximately 14 g/kg (Hanley, 2017). Assuming an in-situ porosity of 0.3 and fully saturated conditions, this salt content is equivalent to a pore fluid salinity of 71.4 g/L.

5.2.6 Summary of Index Properties

The results of the index tests performed for this research are summarized in Table 5-1. The average particle size of Series II RGoG is nearly identical to that of Series I. The values for liquid limit, plasticity index, and activity of RGoG after secondary processing with the shear pump method described in section 3.3.3 are significantly higher than the value after only primary processing. The discrepancy shows that processing plays an important role in material behavior. The liquid limit and plasticity index of Series II are also higher than those values for Series I after secondary processing. This could be due to heterogeneity in the core. It is also possible that Series I was not sufficiently processed and therefore is not representative of behavior of the material after complete reduction of the clay aggregates.

Interpreting hydrometer test results proved to be problematic, probably because of structured water, so the pipette test was used to accurately analyze grain size distribution. Comparison of the Atterberg limits results between the primary processed and secondary

processed material indicates that primary processing alone does not fully break down the clay aggregates and secondary processing is necessary.

Mineralogy results show that the material has a high fraction of kaolinite, which is not consistent with the high Atterberg limit results. Although typical Atterberg limit values for kaolinite clays are much lower, the discrepancy could be explained by extremely low size of kaolinite particles or mixing with smectite particles which exhibit a considerable influence on the overall mechanical properties of RGoG.

This is a new type of mineralogy for the Tufts database. The clay mineralogy is different than the other natural materials previously studied in the Tufts lab; all other natural materials have been made up of illite and smectite with very little kaolinite. This mineralogy moves into a new region of the mineralogy plot (Figure 5-2). The high liquid limit and plastic limit are not expected based on the Kaolinite mineralogy, which will provide valuable insight into the impact of clay mineralogy on mechanical behavior.

5.3 MERCURY POROSIMETRY

Chevron performed mercury porosimetry tests on seven resedimented specimens and several intact specimens. The resedimented specimens sent to Chevron were compressed CRS specimens cut in half. One half was oven dried in the Tufts lab and the other half was preserved moist. The test specimens and their maximum stress levels are specified in Table 3-1.

Mercury porosimetry has been widely used to analyze the pore structure of fine-grained soil specimens. The accuracy of the test has come into question in literature because many pores in fine-grained materials are not accessible to the surrounding mercury. Specimens are oven dried before mercury porosimetry tests, which causes contraction in fine grained specimens (Figure 5-8). Deirieh et al. (2019) studied the effects of oven drying and MICP on RGoM_EI at various stress levels and concluded that oven drying induced shrinkage in both large (>35 nm) and small (<35 nm) pores. The large pores are interparticle pores at the boundaries of silt particles and clay aggregates, and the small pores are clay pores between clay particles within a clay aggregate. This contradicted previous studies on the topic, which likely did not consider that MICP does not provide valid estimates for pore size distributions in materials with limited pore

accessibility (Diamond, 2000). Deirieh et al. also concluded that increasing effective stress leads to shrinkage in both small and large pores. Shrinkage is stress dependent, with a progressively smaller portion of shrinkage present in samples under higher effective stresses (Deirieh, Chang, Casey, Joester, & Germaine, 2019).

Although Deirieh et al. concluded that oven drying causes the collapse of pores of all sizes, they also noted a lack of visible change in the shape, size, orientation, and spatial distribution of pores and particles after oven drying based on SEM images. They attribute the lack of difference to much of the shrinkage taking place in pores that are smaller than 35 nm and therefore not detectable in SEM images. They conclude that mercury porosimetry can be valuable for assessing pore structure trends in mudrocks, but it should not be used to quantitatively assess changes in porosity.

Mercury porosimetry curves comparing primary processed RGoG to secondary processed RGoG compressed to stress levels of 10 MPa, 35 MPa, and 100 MPa in a CRS apparatus are compared in Figure 5-9. The modal pore throat radius is plotted versus stress level in Figure 5-10. Secondary processing increases the modal pore throat radius, which is the peak of the incremental porosity curve. This is likely due to the clay aggregates being broken down during secondary processing. The values converge as stress levels increase, and they overlap at the 100 MPa stress level.

Mercury porosimetry curves comparing incremental porosity to pore throat radius for secondary processed RGoG specimens are compared to the mercury porosimetry curve for an intact specimen with an effective overburden pressure of approximately 9.5 MPa in Figure 5-11. The modal pore throat radius for the resedimented specimen compressed to 10 MPa is slightly higher than that of the intact specimen, which had a similar overburden pressure (9.5 MPa). This means that resedimented specimens are less dense than intact specimens.

The cumulative porosity for the same three secondary processed specimens is compared to the cumulative porosity of the intact specimen in Figure 5-12. The curves indicate that the oven dried porosity of the 10 MPa specimen is approximately 0.33, the 35 MPa specimen is approximately 0.27, and the 100 MPa specimen is approximately 0.24. The oven dried porosity of the intact specimen (9.5 MPa) is approximately 0.22. Based on the normally consolidated portion of the compression curves in Figure 5-15, the porosity of the specimen at 10 MPa should

be approximately 0.38, at 35 MPa it should be approximately 0.28, and at 100 MPa it should be approximately 0.18. Based on measurements on intact core provided by Chevron, the porosity of intact GoG is approximately 0.32. Each of the resedimented specimens was compressed in a CRS apparatus and then removed before oven drying. Accurately measuring swelling during the takedown phase of a CRS test is difficult, but the specimens likely swelled to a much higher porosity than what would be indicated by the compression curve during that phase. Then shrinkage to the MICP curve porosities occurred during oven drying.

The porosity of RGoG estimated based on the compression curves at each stress level is plotted versus modal pore throat radius in Figure 5-13 and compared to intact GoG. The modal pore throat radius decreases linearly with porosity in the resedimented material. The intact material has a lower modal pore throat radius than the resedimented line at its porosity value of 0.32. The intact GoG, at an in situ effective stress of 9.5 MPa, has a significantly lower porosity and modal pore throat radius than RGoG at a comparable stress level of 10 MPa.

In general, the lower stress specimens shrank more than the higher stress specimens. This is consistent with Dierieh et al. (2019), who measured drying shrinkage ranging from 69% in RGoM_EI specimens at 0.2 MPa to 29% in RGoM_EI specimens at 63 MPa. The correlation with stress level is not as apparent with RGoM due to the uncertainty caused by swelling.

The incremental porosity curves and the cumulative porosity curves for the resedimented specimens have the same shape as the intact curves. The similar shapes show that the pore structure of resedimented specimens is the same as that of intact specimens over the range of pore sizes. The resedimented curves have matching shapes with varying peak values over the stress levels tested, which shows that resedimentation is an accurate analog for intact pore structure over a range of stress levels. The shifting of the resedimented curves toward lower pore throat radii with increasing stress level, as well as the similar shapes of the intact and resedimented curves, indicates that a resedimented specimen could be brought to a stress level that would recreate the intact pore structure exactly. However, that exact stress level is uncertain due to the uncertainty surrounding the results of the test due to oven drying and the qualitative nature of the analysis of the test results.

5.4 CONSOLIDATION

Consolidation tests were performed on RGoG using both high and low stress CRS apparatus. One high stress test CRS test was performed on intact GoG. A total of 10 CRS tests were performed. Specimens were K_0 consolidated prior to undrained shear in the triaxial tests. Two triaxial tests were performed. This section describes the consolidation results from all these tests and presents a comparison of intact and resedimented results.

5.4.1 CRS Results

Five low stress CRS tests were performed on RGoG. Of the five low stress tests, two were performed on primary processed Series I RGoG, two were performed on secondary processed Series I RGoG, and one was performed on secondary processed Series II RGoG. The compression curves for all the low stress tests are presented in void ratio space in Figure 5-14 and porosity space in Figure 5-15.

The low stress compression curves all fall into a narrow range. Series II appears to be slightly higher on the void ratio/porosity axis than Series I, but all curves converge at higher stresses and have the same slope. Although secondary processing drastically increases the liquid limit of RGoG, the compression curves for the two tests on primary processed RGoG show no apparent difference from the secondary processed RGoG.

Five high stress CRS tests were performed. Of the five high stress tests, two were performed on primary processed Series I RGoG, one was performed on secondary processed Series I RGoG, one was performed on secondary processed Series II RGoG, and one was performed on intact GoG. The compression curves for all the high stress tests are presented in void ratio space in Figure 5-16 and porosity space in Figure 5-17.

The high stress curves are slightly more scattered on the void ratio/porosity axis than the low stress curves, but the slopes remain consistent over full stress range. Series II falls between the scatter of Series I in the high stress curves. Again, secondary processing appears to have little effect on compression at high stresses, even though it has a major effect on liquid limit.

The scatter in the high stress curves is likely due to errors in measuring porosity, but the consistent slopes show overall consistent behavior. Figure 5-18 shows the same high stress curves with initial void ratios adjusted. The void ratios are adjusted so that each curve converged

to the void ratio of intact GoG at 100 MPa. Initial void ratios for CRS1588, CRS1589, CRS1590, and CRS1610 were adjusted by 5.0%, 7.5%, -0.9%, and 4.2%, respectively. The curves all have similar slopes in their normally consolidated regions.

Casey et. al. (2019) analyzed empirical models for evaluating the compression behavior of resedimented mudrocks based on 15 different resedimented mudrocks. They concluded that normal compression of silt-rich, low liquid limit mudrocks is best described by assuming a log-linear relationship between vertical effective stress and void ratio. Normal compression of smectite-rich, higher liquid limit mudrocks is best described by assuming a log-linear relationship between vertical effective stress and porosity. RGoG does not fit into either of those models. The porosity space compression curves are concave down, and the void ratio space curves are concave up.

Casey et al. also noted that a log-log relationship of (1 + void ratio) and vertical effective stress as another description for compression behavior, although none of the materials in their study fit into that framework exactly, However, that relationship is fairly accurate for describing the compression behavior of RGoG, which does not fit into the two other frameworks preferred by Casey et al. Figure 5-19 shows the series II compression curves, each with an initial void ratio increased by 4.2% to match the intact curve, plotted in the (1 + void ratio) versus effective stress space. A straight-line fit is shown on the plot. The straight-line fit is represented by the following equation:

$$\ln(1 + e) = C \ln\left(\frac{\sigma'_v}{100}\right) + e_{100} \qquad\qquad 5\text{-}4$$

$where: C = slope\ of\ the\ regression\ line$
$\qquad\quad e_{100} = void\ ratio\ at\ 100\ MP$

This equation is based on the compression curve for intact GoG. The value of C used in the regression line is -0.117 and the value of e_{100} is 0.271. The equation predicts void ratio for normally consolidated GoG and RGoG reasonably accurately over about two and a half orders of magnitude, with an R^2 value of 0.9954. The compression curves dip slightly below the regression line in the middle of the stress range (approximately 2 to 15 MPa) and rise above the regression line at the low stress end of the range (lower than approximately 0.5 MPa). The compression

curves are not perfectly linear in this space; however, the line captures the curves remarkably well for a straight line over more than two orders of magnitude.

Although the compression curves are not linear in void ratio space, an exponential equation can be used to fit the curves. Figure 5-20 shows adjusted void ratio versus effective stress for the same tests used for the above correlation. The following equation was developed to fit the curves over the stress range of 0.1 to 100 MPa:

$$e = 1.25(0.19\sigma_v')^{-0.17} - 0.47 \qquad\qquad 5\text{-}5$$

The equation fits the concave up shape of the curves reasonably well over three orders of magnitude, with an R^2 value of 0.9995. It would likely need to be adjusted to fit results outside of that stress range. This equation is not simply summarized by a linear model, like equation 5-4, but it gives an accurate estimate of void ratio based on stress level over the full stress range.

5.4.2 Triaxial Consolidation Results

Two triaxial tests were performed, each with a K_0 consolidation phase prior to shear. One test was a low stress test compressed to 0.4 MPa, and the other was a medium stress test compressed to 4 MPa. Both tests were performed on secondary processed Series II RGoG. The compression curves from those K_0 consolidation phases are plotted with both the low stress and high stress Series II CRS curves in Figure 5-21. The triaxial compression curves follow the concave up orientation of the CRS curves.

5.4.3 Comparison of Intact to Resedimented

Figure 5-16 and Figure 5-17 show measurements of intact void ratio and porosity plotted with the compression curves from high stress CRS tests. These measurements are based on mass and volume measurements performed by Chevron on triaxial sized specimens from preserved intact GoG. The values vary between 0.324 and 0.339. The in situ effective stress for these specimens was estimated at 9.5 MPa. The intact material is approximately 0.11 void ratio units, 0.5 porosity units, lower (denser) than Series II RGoG at the same stress level. These results agree with mercury porosimetry data that show RGoG to be less dense than intact GoG at similar stress levels, discussed in section 5.3.

In addition to porosity data on intact specimens, a high stress CRS test was performed on an intact GoG specimen for direct comparison to RGoG. The specimen was preserved in wax

and wrapped in aluminum foil, shown in Figure 5-22 when it was received in the Tufts lab. The specimen was not at full saturation for the trimming and setup portions of the test. As shown in Table 5-10, the specimen was at approximately 45% saturation before the test began, which is not typical for a sample at depth and less than half of the saturation value of all other CRS specimens. Full saturation is essential for accurate CRS results. The specimen was brought to full saturation in the high stress CRS apparatus with back pressure saturation for 28.5 hours at 0.4 MPa. Future specimens for intact CRS testing would benefit from being saturated using the vacuum desiccator procedure discussed in section 3.5.2 before trimming and back pressure saturation.

Once saturated, the intact specimen behaved similarly to how a resedimented specimen would have been expected to behave in CRS compression: a flat recompression phase followed by a steepening of the curve to the steep virgin compression line. After showing an initially very stiff response, the curvature between reloading and virgin compression stretched over a much wider stress range than a typical resedimented specimen, which can be seen in the gradual steepening of the curve. The curvature stretches over a range of approximately 7 MPa to almost 30 MPa, whereas most resedimented specimens transition from recompression to virgin compression over a range of just a few MPa. The virgin compression lines of the two tests are compared in Figure 5-23, in which a straight line is fit to the straight portion of each curve. The slope of the virgin compression line, known as the compression index (C_c) is calculated with the following equation:

$$C_c = -\frac{\Delta e}{\Delta \log(\sigma'_{vc})}$$
5-6

where: $C_c = compression\ index$
$e = void\ ratio$
$\sigma'_{vc} = vertical\ effective\ stress$

The compression index fit line for the Series II RGoG was 0.375, and the compression index fit for the intact GoG was 0.384. The compression index was also plotted versus stress level for the normally consolidated portion of each test in Figure 5-24. The points in that figure represent the compression index, calculated using the equation above. The points were calculated using values of void ratio and effective stress separated by 50 data acquisition system readings to

reduce noise. The intact compression index is slightly higher than the resedimented compression index, which is the same trend shown by the straight line fit.

The normally consolidated portion of the intact GoG curve compares very well to that of RGoG, as shown in Figure 5-23. The intact GoG curve is approximately 0.037 void ratio units above (less dense) the RGoG curve, and the compression indices are comparable. Karig and Ask (2003) present data on disaggregated and intact specimens over a stress range of 0.2 to 20 MPa that shows the opposite trend: disaggregated material is less dense than intact material, but their reconstitution methods are unclear. However, their results showed disaggregated and intact material having the same compression index, which agrees with the GoG and RGoG results. The plots of intact porosity measurements show the opposite trend: they are denser than the resedimented specimens at the in situ stress level of 9.5 MPa. More testing is necessary to determine if the differences in void ratio between RGoG and GoG are systematic or within experimental variability.

5.4.4 Intact Preconsolidation Pressure

The strain energy method (Becker, Crooks, Been, & Jefferies, 1987) was used to calculate the preconsolidation pressure for the intact CRS specimen. The strain energy method uses a plot of effective stress versus work on a linear scale. A straight line is extended from the recompression portion of the curve, and another straight line is extended from the normally consolidated portion of the curve. The estimated preconsolidation pressure lies at the intersection of the lines. The strain energy construction for the intact GoG specimen is shown in Figure 5-25. A preconsolidation pressure of 28.4 MPa was estimated for this specimen based on the strain energy method. This analysis is based on the shape of the compression curve and is not affected by the position of the curve on the void ratio axis. The estimated in situ value is closer to 10 MPa based on Chevron's estimates of overburden density from well logs and in situ pore pressure.

The discrepancy in preconsolidation pressure could be explained by several factors. One logical explanation is that the deposit was unloaded from some previously higher stress state and is now overconsolidated. However, the geological background of the region and the depositional history of GoG does not support the hypothesis that mechanical unloading ever took place. Instead, a possible cause of overconsolidation is bonding or cementation of the grains caused by

diagenetic processes, which could have increased the yield strength past what would be expected based on in situ effective stress alone. Casey (2014) defines "apparent preconsolidation" as an increase in overconsolidation due to non-mechanical processes, such as cementation. Diagenetic processes can be a much more important cause of overconsolidation in older sediments than mechanical processes (Casey, 2014).

Another possible cause of the discrepancy is loading rate dependence and secondary compression, also known as creep. The loading rate in a laboratory CRS test is much different than the geologic loading rate that GoG has experienced since deposition. Much of the research on this topic focuses on soft soils. However, Powell, Take, Siemens, & Remenda (2012) investigated the time dependent behavior of the Bearpaw Shale, a hard clay shale, using both CRS and oedometer loading techniques. They concluded that both soft clays and hard clay shales show a dependence of preconsolidation pressure on strain rate, and that the influence of creep is important although hard to quantify over the geological history of a deposit.

Another explanation for the discrepancy could be the underestimation of field density, and therefore the underestimation of true insitu effective stress. Ferrari, Favero, and Laloui (2016) compared the yield stress of Opalinus Clay specimens to the in situ effective stress estimated by field densities. They created an apparatus capable of performing oedometer tests to 100 MPa with pore pressure control. They created an analytical method to analyze shale consolidation behavior, which was modified from the traditional oedometer analysis method due to the nature of the hydraulic jack causing the load to increase to the target load for each increment over several minutes instead of instantaneously. They tested two different series of Opalinus Clay specimens. They used the Casagrande method (Casagrande, 1936) to determine the yield stress of their specimens. The Casagrande yield stress was on the order of 10-20% higher than the estimated overburden stress based on a comparison to vertical stress estimated from the approximate depth and density of the samples indicates that. However, they point out that the accuracy of in-situ effective stress measurements is difficult to verify, and these estimates are still much more accurate than the strain energy construction for GoG. Finally, they also note a pre- to post-yield transition that is rounded, similar to GoG.

Sampling disturbance could also play an important role in explaining the discrepancy between yield stress and preconsolidation pressure. Lunne et al. (1997) proposed the following ratio as criteria for evaluating sample disturbance:

$$\frac{\Delta e}{e_0}$$

<div align="right">5-7</div>

$where: \Delta e = change\ in\ void\ ratio\ when\ loading\ to\ the\ in\ situ\ vertical\ stress$
$\qquad e_0 = initial\ void\ ratio$

Table 5-13 shows the ratings of sample disturbance on a scale of "excellent" to "very poor" based on the value of the ratio. The intact GoG specimen has a sample quality index ratio of approximately 0.06, which puts it in the "good to fair" sample quality range. However, this method of evaluating disturbance may not be applicable to low void ratio material such as GoG.

Kontopoulos (2012) studied the effects of sample disturbance on preconsolidation pressure on both normally consolidated and overconsolidated clays. He primarily tested San Francisco Bay Mud and Boston Blue Clay at lower stress levels. He concluded that disturbance always leads to more rounded compression curves, and that defining the preconsolidation pressure becomes more ambiguous with increasing disturbance. He also concluded that intact specimens are more prone to disturbance than resedimented specimens. His results showed that disturbance could cause the preconsolidation pressure to increase or decrease from the true value, and that depends on two mechanisms: decrease in sampling effective stress and change in virgin compression line slope. Kontopoulos found that preconsolidation is overpredicted when sampling effective stress decreases due to disturbance, but virgin compression line slope remains relatively unchanged. The intact virgin compression line slope of GoG is almost identical to that of RGoG, and the value of preconsolidation pressure was overpredicted, which agrees with the results from Kontopoulos.

Research on the effects of sampling disturbance on clays and shales at higher insitu effective stresses is scarce. Tanaka, Ritoh, and Omukai (2002) extensively investigated the consolidaion properties of pleistocene sediments in Osaka Bay in Western Japan to depths of up to 400 meters. They concluded that consolidation properties, including preconsolidaiton pressure, are somewhat scattered with depth. Figure 5-26 shows insitu effective overburden stress compared to preconsolidation pressure determined from CRS tests. The test specimens in

the plot had insitu effective stresses ranging from approximately 0.25 MPa to over 3 MPa. Although the sediments in question are believed to be normally consolidated, many of the test specimens have overconsolidaiton ratios of two or higher. They investigated sample disturbance as a possible explanation for the considerable scatter in preconsolidation presssure values measuerd in their CRS tests. They concluded that neither volumetric strains nor changes in sampling effective stress due to distrubance influence preconsolidaiton pressure. Instead, ageing and cementation of soil particles are the main influence on preconsolidation pressure values. If sampling does not destroy the cemented bonds in a specimen, then the preconsolidiation pressure can be correctly measured even if a large proportion of its sampling effective stress is lost during the sampling and test setup process. OCR can vary greatly with depth because the degree of cementation in each layer of a soil can be significantly influenced by the sedimentation environment.

Although the Tanaka, Ritoh, and Omukai study does not extend to stress levels equivalent to the effective overburden of GoG, it does extend to the same order of magnitude; whereas most geotechnical studies do not. Their results came when studying a comparatively much younger soil. They concluded that ageing and cementaiton are the main factors determining preconsolidaiton pressure, and those factors could even be amplified for the much older GoG.

On the other hand, Karig and Ask (2003) concluded that the yield stress of intact specimens accurately reflects the preconsolidation stress state, as discussed in 2.3.2. GoG appears to not fit into this conclusion. More testing of intact specimens is necessary to determine if all intact mudrocks at high stress levels can be expected to retain their preconsolidation pressure as the yield stress in a compression test.

5.4.5 Comparison of RGoG to Database

Figure 5-27 shows the compression curves for series II RGoG compared to RGoM_EI, RLC, and RNC in void ratio space. These three materials were used for the comparison because they have similar liquid limits to RGoG (Table 5-9), and therefore are expected to have similar mechanical behavior, including compression properties. The slopes of the curves are similar, but

RGoG plots at a higher void ratio than the other materials over the same stress range. The other curves are more concave up in slope, as observed by Casey et al. (2019).

Figure 5-28 shows compressibility correlations based on liquid limit developed by Casey (2014) based on the rest of the GeoFluids database. The correlations predict void ratio at a given stress level based on liquid limit. As stress level increases, liquid limit has less of an impact on void ratio. RGoG is slightly denser than the correlation predicts at 0.1 MPa. However, this value is uncertain because the void ratio value at 0.1 MPa was extrapolated by extending the virgin compression line. The other void ratio values at 1, 10, and 40 MPa are less dense than the correlation predicts. This is consistent with the compression curves for RGoG being higher on the void ratio axis than the other materials in Figure 5-27.

5.5   PERMEABILITY

Ten CRS tests were performed as described in section 5.4.1. Hydraulic conductivity measurements are recorded during CRS tests, and permeability is calculated from these measurements. Permeability values as a function of porosity for RGoG derived from low stress and high stress CRS tests are shown in Figure 5-29. The permeability of intact GoG as a function of porosity is also shown in Figure 5-29. Some of the CRS tests were not included in the figure to prevent cluttering the plot.

All tests show a trend of decreasing permeability that is log linear with decreasing porosity. This trend is expected and has been documented with resedimented clay specimens (Casey, 2014) and is typical of the rest of the materials in the GeoFluids database. Figure 5-30 shows a comparison of the permeability of RGoG to two GeoFluids database materials: RGoM_EI, RLC, and RNC. The comparison is discussed further in section 5.5.2.

Some scatter exists with the permeability data from the high stress CRS tests. The permeability curves for low stress tests have little scatter compared to the high stress curves. The high stress curves also show slightly higher permeability at the porosity values at which they overlap with the low stress curves. This could be due to apparatus differences. However, the slopes of the curves are consistent for both high and low stress. The permeability of the Series II

RGoG is slightly lower than that of the Series I RGoG for both the high and low stress cases, but the slopes of the curves for each series are consistent.

5.5.1 Comparison of Intact to Resedimented

The permeability of the intact GoG is plotted as the specimen reaches its normally consolidated phase. The intact permeability is lower than the resedimented permeability at any given porosity value during the normally consolidated phase. This result is consistent with the mercury porosimetry results shown in Figure 5-13. At a given porosity value, the intact GoG has a lower modal pore throat radius than RGoG. The lower modal pore throat radius leads to a lower permeability at a given value of porosity.

5.5.2 Comparison of RGoG to Database

The permeability of RGoG is compared to RGoM_EI, RLC, and RNC in Figure 5-30. These materials were chosen from the GeoFluids database for comparison because they have comparable Atterberg limits (Table 5-9), which implies that they also have comparable mechanical behavior, including permeability properties.

All the materials have permeability that is linear in log-log space when plotted versus porosity. This behavior is expected and is typical of the database as a whole. Casey et al. (2013) developed correlations for permeability of mudrocks based on liquid limit. The correlations were developed using permeability versus porosity measurements on several materials in the GeoFluids database, including those shown in Figure 5-30. In general, Casey et al. concluded that permeability decreases with increasing liquid limit. They developed the following two equations that use liquid limit to approximate a line in log-log porosity versus permeability space that represents the permeability of a given mudrock:

$$log_{10}(k_{0.5}) = -7.40log_{10}(LL) - 3.7 \qquad \text{5-8}$$

$$\gamma = -0.072LL + 4.9 \qquad \text{5-9}$$

$where: k_{0.5} = permeability\ at\ a\ porosity\ of\ 0.5$
$\quad LL = liquid\ limit\ (\%)$
$\quad \gamma = slope\ of\ the\ regression\ line$

The true values of $k_{0.5}$ and γ from both a high stress and low stress CRS test on series II RGoG are compared to the values for other materials used to develop the correlations are

compared in Figure 5-31 and Figure 5-32. The low stress test has a much lower slope (γ) than predicted by the liquid limit of RGoG. However, the high stress test has a slightly steeper slope that fits into the scatter of the rest of the data used to develop the correlation. The values of $k_{0.5}$ for both tests are slightly lower than predicted.

5.6 STRESS-STRAIN STRENGTH

The results of two successful triaxial tests on Series II RGoG: one low stress test and one medium stress test, are presented in this section.

5.6.1 Lateral Stress Coefficient K_0

The results for lateral stress ratio K_0 as a function of stress level during the normally consolidated phase of the two triaxial tests are shown in Figure 5-34. K_0 increases slightly with stress level during consolidation with each individual RGoG specimen, and it increases between the two specimens at different stress levels. This trend is expected and has been documented with other materials in the database (Casey, 2014).

5.6.2 Undrained Shear

Undrained shear results are summarized in Table 5-12. Stress-strain curves are shown in Figure 5-35. Both specimens reach peak strength at very low strain values then experience strain softening. Figure 5-36 shows a normalized p-q plot. The following equations define p' and q:

$$p' = \frac{\sigma'_1 + \sigma'_3}{2} \qquad \qquad 5\text{-}10$$

$$q = \frac{\sigma'_1 - \sigma'_3}{2} \qquad \qquad 5\text{-}11$$

$where\ p' = average\ effective\ stress$
$\qquad q = shear\ stress$

The angle α' used in p'-q space can be converted to the commonly used measure of friction angle (φ') using the following relation:

$$\tan(\alpha') = \sin(\varphi') \qquad \qquad 5\text{-}12$$

Both the peak friction angle and normalized undrained shear strength (S_u/σ'_{vc}) of RGoG decrease with increased stress level, a trend that has been well-documented with other materials in the database (Casey, 2014). Both specimens developed distinct failure planes during shear,

shown in Figure 5-37 and Figure 5-38. The development of failure planes is a phenomenon that is unexpected with normally consolidated fine-grained specimens at low to medium stress levels.

Triaxial tests have not yet been performed on intact GoG in the Tufts laboratory. Performing a triaxial test using the same methods and apparatus that was used for testing resedimented specimens is the next step in researching the relationship of intact and resedimented GoG.

5.6.3   Comparison of RGoG to Database

Correlations using liquid limit to predict K_0, critical state friction angle, and normalized shear strength were developed by Casey (2014) using test results for many of the materials in the GeoFluids database. These correlations are summarized in Germaine (2015). This section describes a preliminary comparison of the results from the two successful triaxial tests on RGoG to those correlations and the other materials in the database.

Figure 5-39 shows a comparison of K_0 values from triaxial tests on RGoG to two materials in the GeoFluids database: RGoM_EI and RBBC. The correlation for K_0 based on liquid limit is as follows:

$$K_{0,NC} = K_{0,10}(0.1\sigma'_{v[MPa]})^J \qquad \text{5-13}$$

$where: K_{0,10} = 0.0059LL + 0.32$
$ J = 0.243\log(LL) - 0.375$

The K_0 values for RGoG increase with increasing stress level, as predicted by the correlation. The slope (J) of the K_0 versus vertical effective stress line is similar to what the correlations predict based on the liquid limit of RGoG series II. The intercept ($K_{0,10}$) is much lower than expected.

Figure 5-40 shows the critical state friction angle of RGoG compared to several materials in the GeoFluids database. The correlation based on liquid limit is as follows:

$$\varphi_{cs} = A(0.001\sigma'_{p[MPa]})^B \qquad \text{5-14}$$

$where: A = -75\log(LL) + 148$
$ B = -0.39\log(LL) + 0.59$

94

Critical state friction angle decreases with increasing stress, as predicted by the correlations. Figure 5-41 and Figure 5-42 show how the A and B parameters of RGoG compare to the correlation, respectively. Both A and B for RGoG are higher than predicted by the correlation.

Figure 5-43 shows a comparison of the normalized undrained shear strength of RGoG to several materials in the GeoFluids database. The correlation for normalized undrained shear strength is as follows:

$$\frac{S_u}{\sigma'_{vc}} = S_1 (1000 \sigma'_{p[MPa]})^T \qquad 5\text{-}15$$

$where: S_1 = 0.86 \log(LL) - 1.04$
$\qquad T = -0.46 \log(LL) + 0.73$

Normalized undrained shear strength decreases with increasing stress, as predicted by the correlation. The S_1 parameter shows a very good fit with the rest of the database. The T parameter is slightly lower than predicted by the correlation.

The comparisons of RGoG to the rest of the GeoFluids database preliminary. They are only based on the results of two triaxial tests. More triaxial results at a range of stress levels are necessary to more accurately determine how RGoG fits into the correlations. Based on the preliminary results, the properties of RGoG have mixed success in fitting with the database correlations. The closest material analog to RGoG in the database is probably RGoM_EI, which has a very similar friction angle but much higher K_0 and normalized S_u values than RGoG. The differences could be a result of the fact that RGoG has much different mineralogy than the rest of the materials in the database, and more triaxial tests should be performed to further assess the fit with the correlations.

5.7 SUMMARY OF TESTING RESULTS

Index tests performed on RGoG included XRD mineralogy, grain size distribution, Atterberg limits, specific gravity, and salt content. RGoG is a high plasticity, kaolinitic clay, which was unexpected based on the mechanical properties of the material, specifically the high liquid limit. This represents a new clay mineralogy for the Tufts database. The amount of processing had a major effect on Atterberg limit results, with liquid limit increasing dramatically

after secondary processing. Hydrometer results began well above the 100% finer line, likely due to structured water, so the pipette test was used to confirm the grain size distribution.

Mercury porosimetry results and measurements performed by Chevron on preserved intact GoG show that RGoG is less dense than intact GoG at a given stress level. The modal pore throat radius of RGoG decreased linearly with decreasing porosity, with the modal pore throat radius of intact GoG sitting below that line. However, the shapes of the resedimented and intact curves are very similar, which indicates that resedimentation effectively recreates intact pore structure.

Compression curves have similar slopes and fall into a narrow range, although more scatter is present with high stress curves. Two equations were developed to fit the virgin compression line of RGoG. Resedimented specimens are less dense than intact specimens measured by Chevron at the in situ effective stress level of 9.5 MPa. The compression curve of intact GoG was very rounded, and the yield stress was much higher than the estimated in situ effective stress. The compression index of intact GoG was a good match for RGoG.

Permeability of both RGoG and GoG is log linear and decreases with decreasing porosity. The intact permeability is slightly lower than the resedimented permeability at the same porosity value. That difference is consistent with mercury porosimetry results that show intact GoG has a lower modal pore throat radius than RGoG at the same porosity.

A comparison to correlations developed based on other materials in the GeoFluids database based on liquid limit yielded mixed results. High stress CRS permeability fit reasonably well into the permeability predictions from Casey (2014). The rates of change in K_0 and normalized undrained shear strength with increasing stress are similar to what was predicted based on liquid limit, but the actual values are much lower than expected. Friction angle was predicted reasonably well. All the materials used to develop the correlations are composed of smectite and illite, with very little kaolinite present. The mineralogical differences as well as structured water and other microstructural differences are possible explanations of the discrepancies between RGoG and the rest of the database.

The next step in comparing intact to resedimented material behavior is to perform triaxial tests on intact GoG using the same methods and apparatus as those that were performed on RGoG.

Property	(units)	Series I		Series II	Comments
		Primary Processed	Secondary Processed	Secondary Processed	
Specific Gravity		2.619	2.657	2.668	Water submersion
Specific Gravity		2.589	-	-	Helium gas
Soluble Salts	(g/kg)	13.2	-	11.5	based on dry mass
Moisture content	(%)	5.5	-	4.45	air dry
Plastic Limit	(%)	30	38	32	
Liquid Limit	(%)	51	79	87	Casagrande cup
Plasticity Index	(%)	21	41	55	
Clay size (<2 um)	(%)	52	62	67	settling velocity
Activity		0.40	0.66	0.82	
CEC	(meq/100g)	-	29.3	23.6	

Table 5-1: RGoG index property summary

Material	Quartz %	Carbonate %	Non-Clay %	Kaolinite %	Ill./Sme. %	Sum. Clay %	CEC meg/100g
Intact							
Average	16	5	25	42	33	75	23
Std. Dev.	5.3	3.6	6.4	4.2	3.0	6.4	1.1
Resed							
Series I	13	1	18	47	35	82	N/A
Series II	10	6	23	47	25	80	24
Average	12	3	19	44	34	81	24
Std. Dev.	1.7	3.4	4.3	3.1	1.6	4.3	-

Table 5-2: XRD Mineralogy – Bulk Summary

Material	Illite %	Smectite %	Kaolinite %	Total %
Intact				
Average	22	23	55	100
% of whole	16.5	17.3	41.3	75.0
Series I				
Average	25	32	43	100
% of whole	20.5	26.2	35.3	82.0
Series II				
Average	23	22	55	100
% of whole	17.2	16.0	40.6	73.8

Table 5-3: XRD Mineralogy – Clay Fraction Summary

Material	Quartz %	Carbonate %	Non-Clay %	Kaolinite %	Ill./Sme. %	Sum. Clay %
Intact						
Average	16	5	25	42	33	75
Std. Dev.	5.3	3.6	6.4	4.2	3.0	6.4
Resed						
Series I	13	1	18	47	35	82
Series II	10	5	20	47	33	80

Table 5-4: XRD Mineralogy Results – Chevron Bulk

Material	Illite %	Smectite %	Kaolinite %	Total %
Intact				
Average	22	23	55	100.0
% of whole	16.5	17.3	41.3	75.0
Series I				
Average	25	32	43	100.0
% of whole	20.5	26.2	35.3	82.0

Table 5-5: XRD Mineralogy Results – Chevron Clay Fraction

Material	Quartz %	Carbonate %	Non-Clay %	Kaolinite %	Ill./Sme. %	Sum. Clay %
Resed						
Series II	10.3	7.7	26.2	41.6	32.2	73.8

Table 5-6: XRD Mineralogy Results – Hutton Bulk

Material	Illite %	Smectite %	Kaolinite %	Total %
Series II				
Average	23	22	55	100.0
% of whole	17.2	16.0	40.6	73.8

Table 5-7: XRD Mineralogy Results – Hutton Clay Fraction

Test Number	HY085	HY086	HY087	HY088	HY089	HY090	HY093	HY094	HY095	HY096
Test Inputs										
Temperature Reading (°C)	22.6	22.6	23.5	22.2	20.5	20.6	21.5	21.4	22.6	22.5
First Suspension Reading	1.0370	1.0370	1.0358	1.0342	1.0189	1.0182	1.029	1.0262	1.0272	1.0275
Total Dry Mass (g)	52.10	51.96	52.00	55.52	28.00	27.34	43.81	39.95	37.28	37.48
Mass of Sodium Hex (g)	5.00	5.00	5.01	5.00	5.00	5.00	5.00	5.00	5.00	5.00
Clay										
Clay Fraction (%)	80%	80%	80%	80%	80%	80%	80%	80%	80%	80%
Specific Surface Area (m^2/g)	500	500	500	500	500	500	500	500	500	500
Surface Water Density (g/cm^3)	1.5	1.5	1.5	1.5	1.5	1.5	1.5	1.5	1.5	1.5
Surface Layer Thickness (A)	6	6	6	6	6	6	6	6	6	6
Density										
Specific Gravity of Clay	2.668	2.668	2.668	2.668	2.668	2.668	2.668	2.668	2.668	2.668
Specific Gravity of Sodium Hex	3.2	3.2	3.2	3.2	3.2	3.2	3.2	3.2	3.2	3.2
Temperature Reading (°C)	22.6	22.6	23.5	22.2	20.5	20.6	21.5	21.4	22.6	22.5
First Suspension Reading	1.037	1.037	1.0358	1.0342	1.0189	1.0182	1.029	1.0262	1.0272	1.0275
Mass										
Total Dry Mass (g)	52.10	51.96	52.00	55.52	28.00	27.34	43.81	39.95	37.28	37.48
Mass of Sodium Hex (g)	5.00	5.00	5.01	5.00	5.00	5.00	5.00	5.00	5.00	5.00
Soil Dry Mass (g)	47.10	46.96	46.99	50.52	23.00	22.34	38.81	34.95	32.28	32.48
Total Mass in Cylinder (g)	1037.00	1037.00	1035.80	1034.20	1018.90	1018.20	1029.00	1026.20	1027.20	1027.50
Mass of Surface Water (g)	16.673	16.624	16.634	17.884	8.142	7.908	13.739	12.372	11.427	11.498
Mass of Free Water (g)	968.23	968.42	967.17	960.80	982.76	982.95	971.45	973.88	978.49	978.52
Volume										
Volume of Surface Water (cm^3)	11.116	11.083	11.090	11.923	5.428	5.272	9.159	8.248	7.618	7.665
Volume of Solids (cm^3)	17.65	17.60	17.61	18.94	8.62	8.37	14.55	13.10	12.10	12.17
Volume of Sodium Hex (cm^3)	1.56	1.56	1.57	1.56	1.56	1.56	1.56	1.56	1.56	1.56
Total Volume (cm^3)	1000	1000	1000	1000	1000	1000	1000	1000	1000	1000
Volume of Free Water (cm^3)	969.67	969.75	969.73	967.58	984.39	984.79	974.73	977.09	978.72	978.60
Comparison										
Density of Free Water at Temp (g/cm^3)	0.9976	0.9976	0.9974	0.9977	0.9981	0.9981	0.9979	0.9979	0.9976	0.9977
Calculated Density of Water (g/cm^3)	0.9985	0.9986	0.9974	0.9930	0.9983	0.9981	0.9966	0.9967	0.9998	0.9999
Difference from True Density	0.0009	0.0010	-0.0001	-0.0047	0.0002	0.0001	-0.0013	-0.0012	0.0021	0.0023
Percentage Difference	0.088%	0.099%	-0.007%	-0.475%	0.024%	0.005%	-0.125%	-0.120%	0.214%	0.227%

Table 5-8: Hydrometer water density calculations

Name	Liquid Limit (%)	Plastic Limit (%)	Plasticity Index (%)
Resedimented Gulf of Guinea - Series II (RGoG)	87	32	55
Resedimented Gulf of Mexico Eugene Island Block (RGoM_EI)	87	24	63
Resedimented London Clay (RLC)	74	31	43
Resedimented Nankai Clay (RNC)	68	29	39
Resedimented Nile Silty Clay (RNSC)	80	27	53

Table 5-9: Database Atterberg limit comparison

Test Number	Sample Number	Series	Reduction	Setup Conditions					Maximum Stress				
				W_i	e_i	S_i	γ_d	γ_t	σ'_{vm}	ε_a	e_c	S_f	γ_t
				(%)	-	(%)	(g/cm^3)	(g/cm^3)	(MPa)	(%)	-	(%)	(g/cm^3)
CRS1551	RS585	I	Primary	58.6	1.762	95.28	0.981	1.600	10	44.12	0.543	132.58	2.210
CRS1553	RS585	I	Primary	57.4	1.696	96.82	1.000	1.625	35	42.00	0.564	99.77	2.075
CRS1556	RS592	I	Secondary	41.2	1.246	93.34	1.207	1.726	35	21.28	0.768	95.25	1.935
CRS1557	RS592	I	Secondary	44.6	1.335	94.62	1.153	1.705	10	31.17	0.607	84.32	1.985
CRS1588	RS585	I	Primary	53.2	1.528	99.53	1.066	1.683	100	51.10	0.236	99.90	2.349
CRS1589	RS592	I	Secondary	38.7	1.139	95.74	1.254	1.778	100	43.91	0.200	99.85	2.388
CRS1590	RS585	I	Primary	54.9	1.576	99.65	1.048	1.672	100	50.25	0.281	100.77	2.305
CRS1599	RS647	II	Secondary	63.4	1.825	100.08	0.963	1.620	10	58.44	0.570	99.90	2.073
CRS1610	RS654	II	Secondary	34.4	1.013	95.43	1.333	1.824	100	39.45	0.219	99.97	2.367
CRS1615	Intact	-	-	9.2	0.565	44.98	1.717	1.868	100	18.52	0.275	99.80	2.309

Table 5-10: CRS phase relations

Test Number	Sample Number	Series	Reduction	Setup Conditions					Maximum Stress				Pre-Shear					
				W_i	e_i	S_i	γ_d	γ_t	σ'_{vm}	ε_a	e_c	$K_{0(NC)}$	σ'_{vc}	ε_a	e_c	OCR	γ_t	$K_{0(NC)}$
				(%)	-	(%)	(g/cm^3)	(g/cm^3)	(MPa)	(%)	-	-	(MPa)	(%)	-	-	(g/cm^3)	-
TX1445	RS674	II	Secondary	57.4	1.952	106.92	0.947	1.643	0.40	19.85	1.366	0.419	0.40	20.80	1.338	1.00	1.921	0.414
TX1455	RS648	II	Secondary	35.1	0.987	100.03	1.376	1.859	3.75	11.67	0.755	0.567	3.75	13.09	0.727	1.00	1.975	0.566

Table 5-11: Triaxial consolidation phase

Test Number	Sample Number	Series	Reduction	End of Consolidation Conditions						At Maximum Shear				At Maximum Obliquity			
				σ'_{vc}	ε_a	e_c	OCR	$K_{0(pre-shear)}$	$t_{secondary}$	ε_a	q/σ'_{vc}	p'/σ'_{vc}	ϕ'	ε_a	q/σ'_{vc}	p'/σ'_{vc}	ϕ'
				(MPa)	(%)	-	-	-	(hr)	(%)	-	-	(°)	(%)	-	-	(°)
TX1445	RS674	II	Secondary	0.40	20.80	1.338	1.00	0.414	16.4	0.18	0.353	0.729	28.94	4.23	0.294	0.741	30.46
TX1455	RS648	II	Secondary	3.75	13.09	0.727	1.00	0.566	174.7	0.62	0.292	0.766	22.43	1.39	0.282	0.737	22.55

Table 5-12: Triaxial shear phase

Table 3. Proposed criteria for evaluation of sample disturbance.

| Overconsolidation ratio | $\Delta e/e_0$ | | | |
	Very good to excellent* (1)	Good to fair* (2)	Poor* (3)	Very poor* (4)
1–2	<0.04	0.04–0.07	0.07–0.14	>0.14
2–4	<0.03	0.03–0.05	0.05–0.10	>0.10

* The description refers to use of the samples for measurement of mechanical properties.
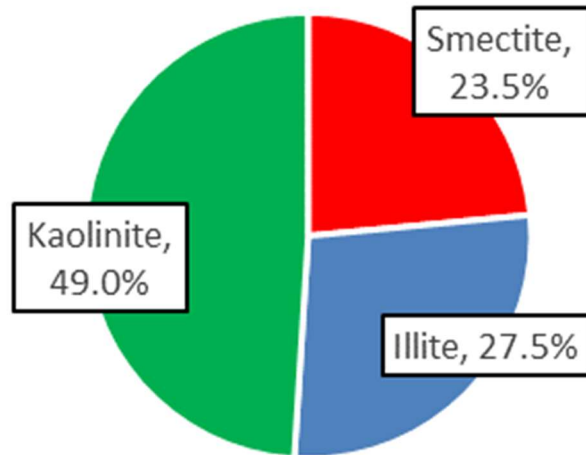
Table 5-13: Sample disturbance criteria
(Lunne, Berre, & Strandvik, 1997)

Figure 5-1: Average clay mineralogy of GoG
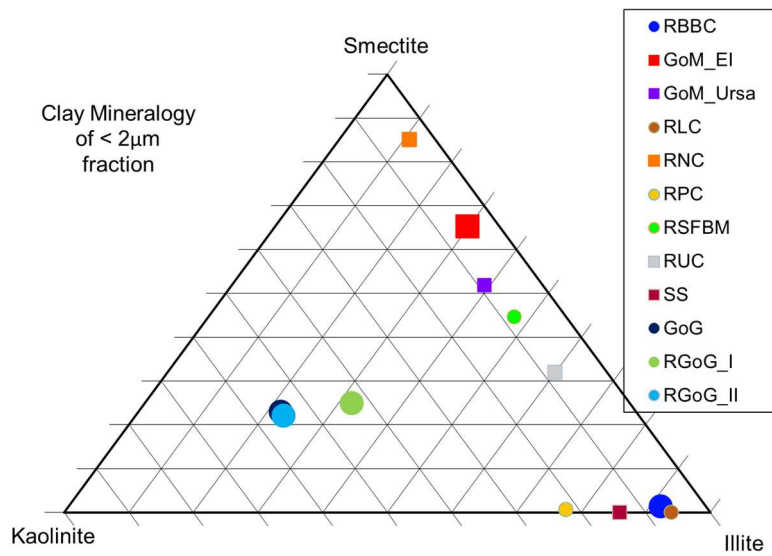
Figure 5-2: Mineralogy of natural soils in the GeoFluids database
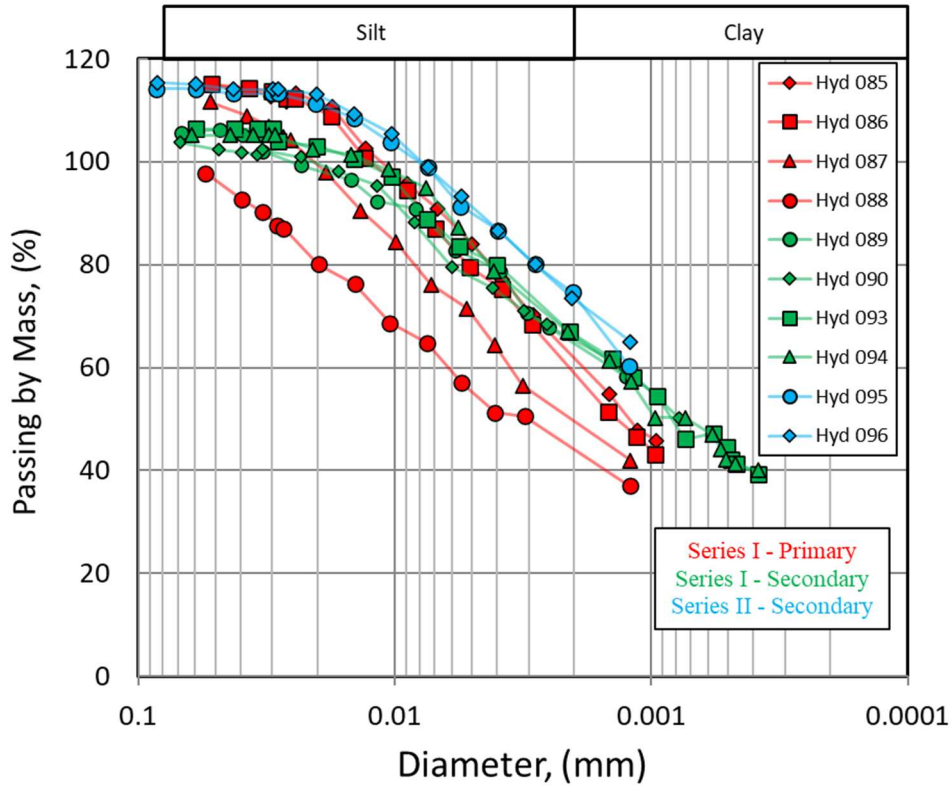
Figure 5-3: Hydrometer test results
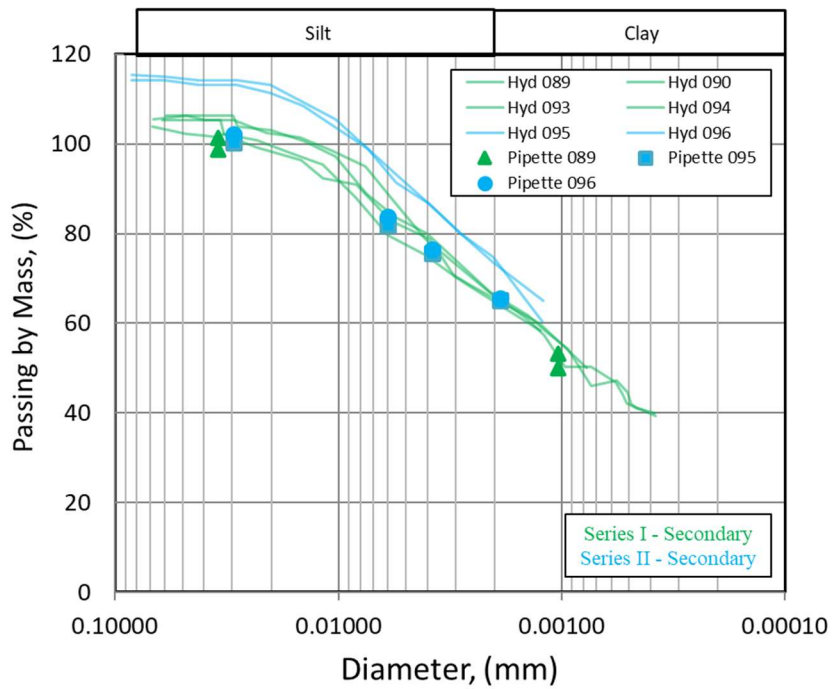
Figure 5-4: Series II grain size distribution results
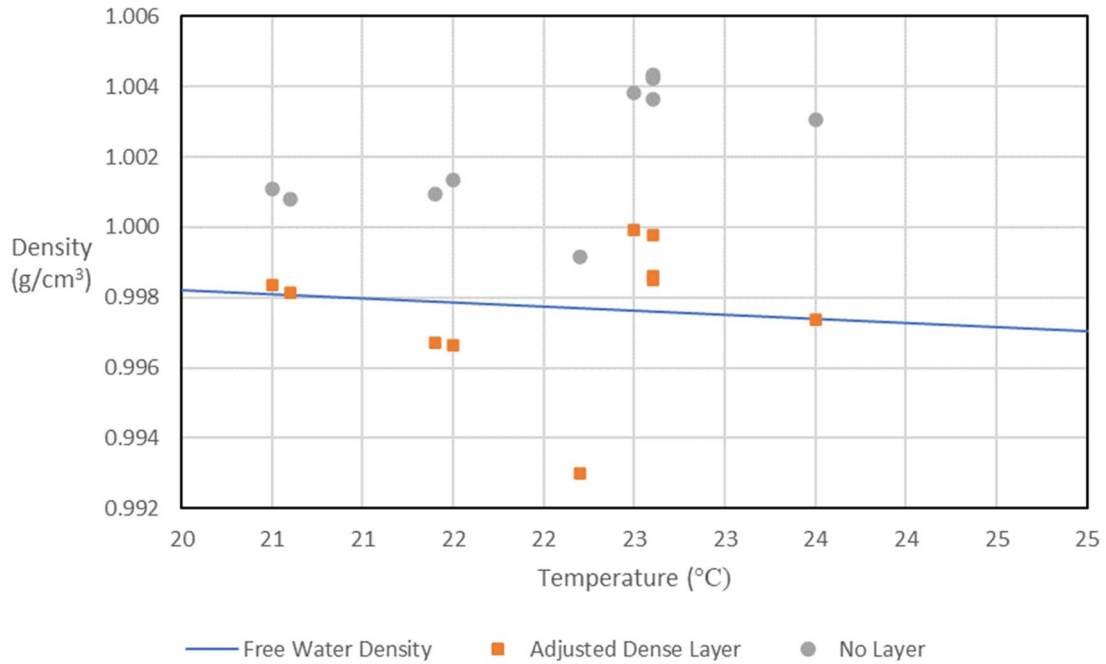
Figure 5-5: Hydrometer water density estimates
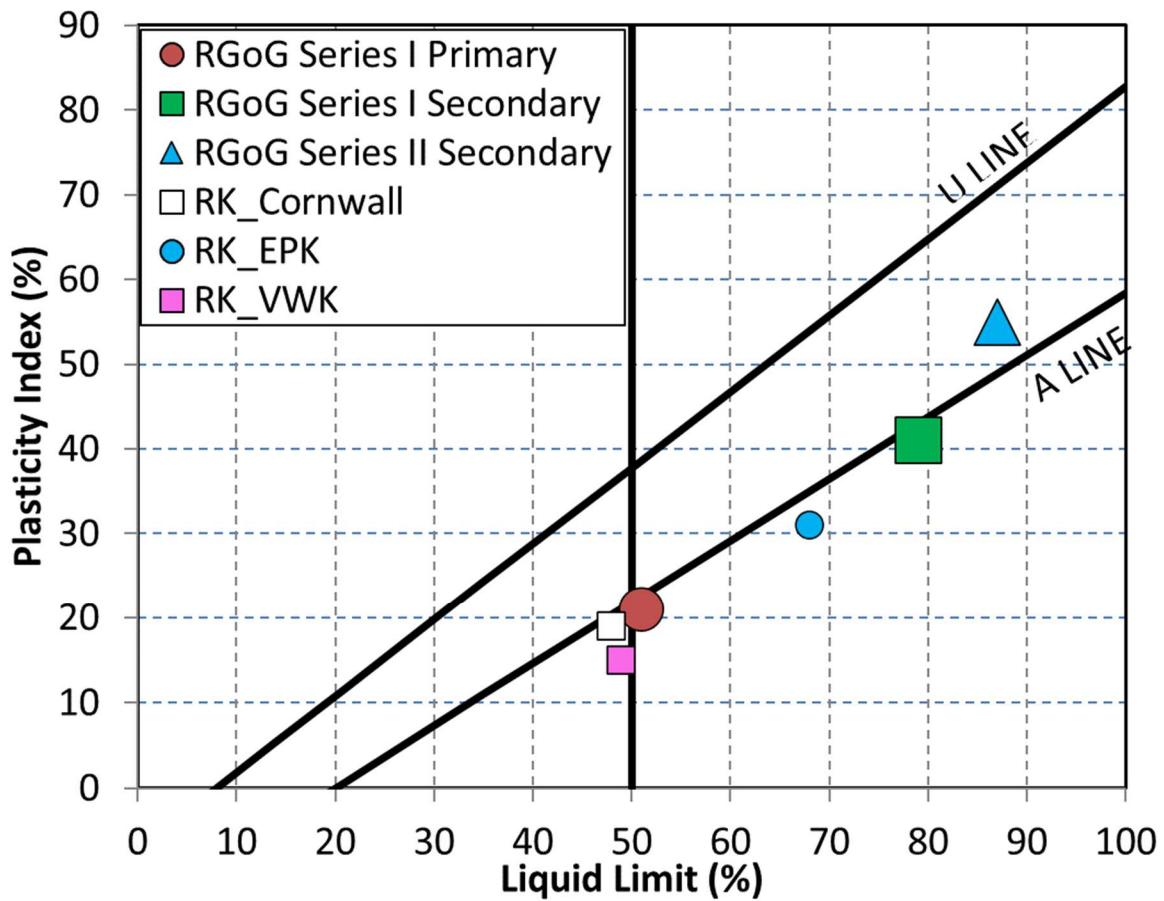
Figure 5-6: Atterberg limit plot: RGoG compared to database kaolins
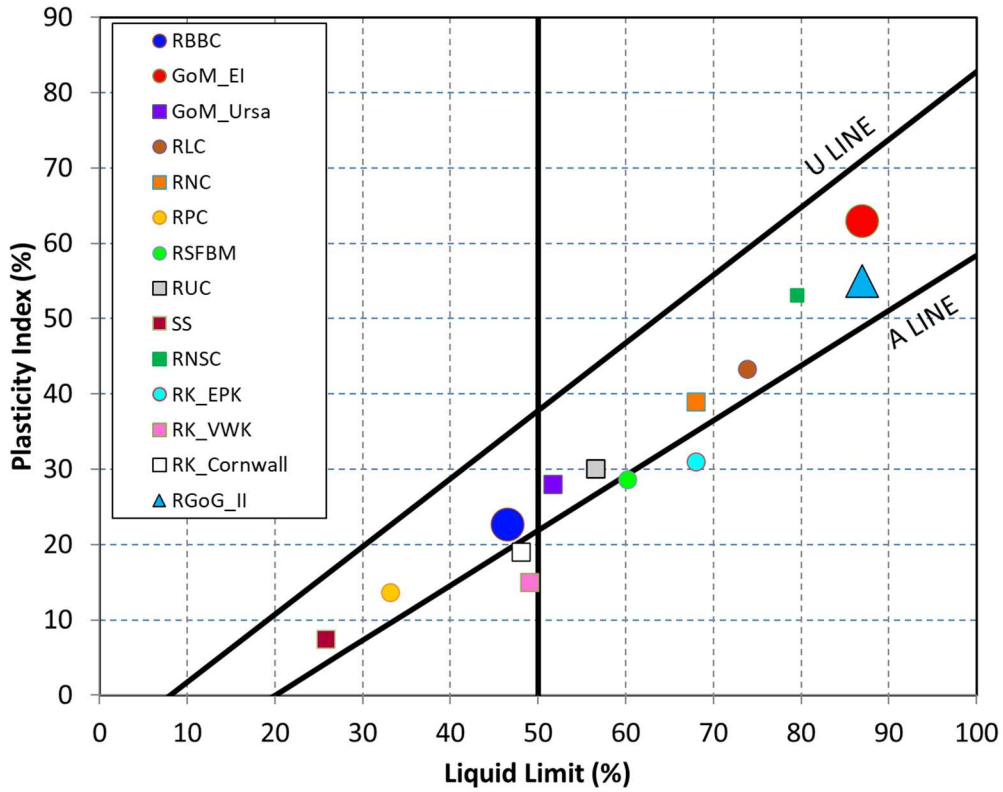
Figure 5-7: Atterberg limit plot: RGoG compared to GeoFluids database
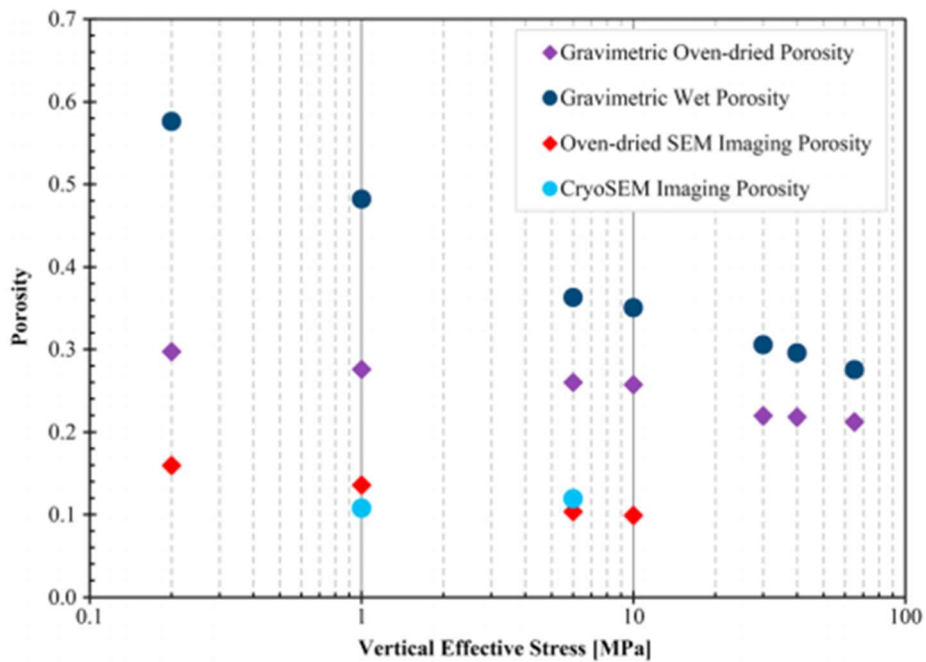
Figure 5-8: Shrinkage due to oven drying
(Deirieh, Chang, Casey, Joester, & Germaine, 2019)
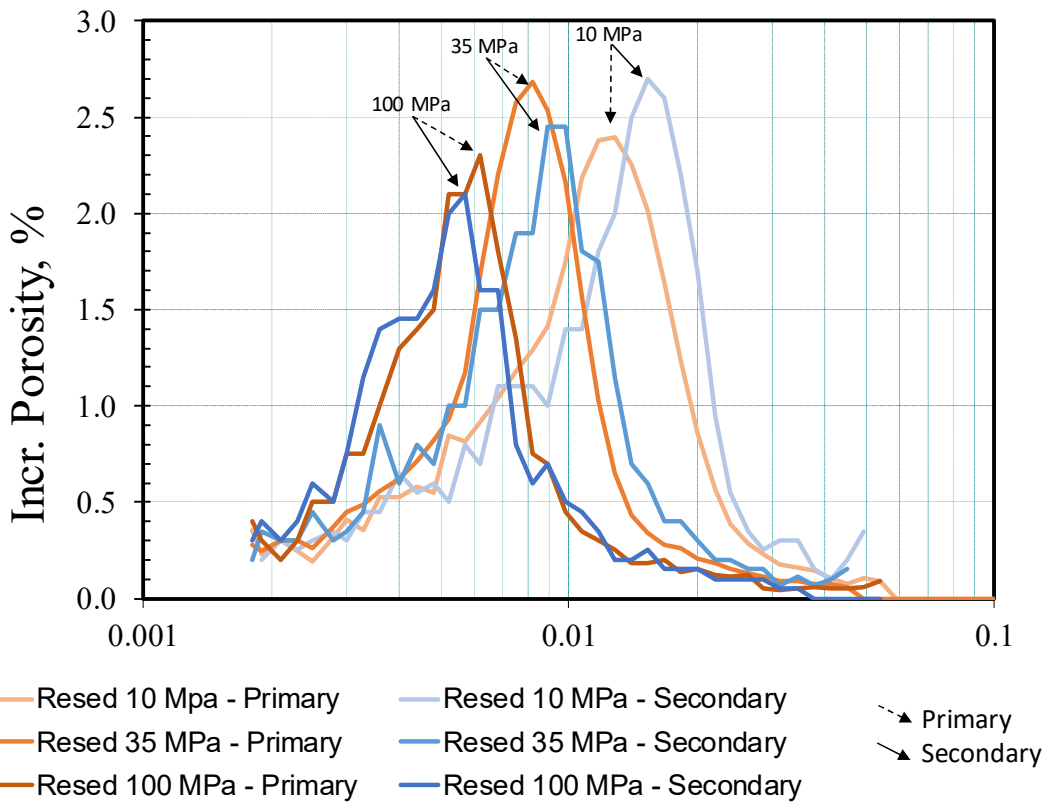
Figure 5-9: MICP results: primary vs. secondary processing
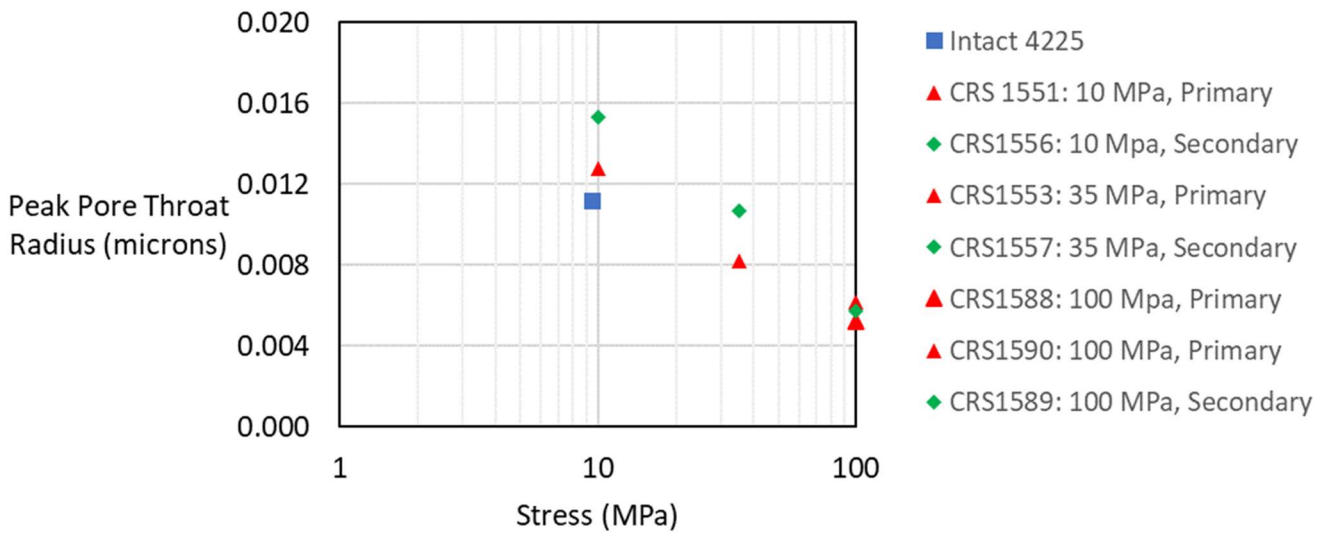
Figure 5-10: MICP results: peak pore throat radius vs stress level
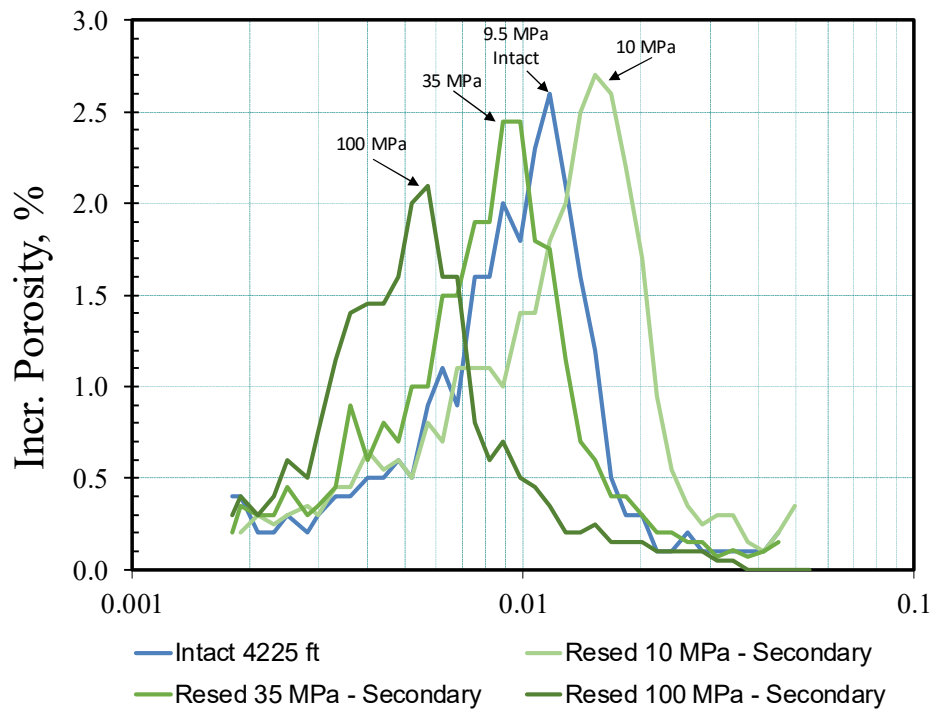
Figure 5-11: MICP results: secondary processing vs. intact
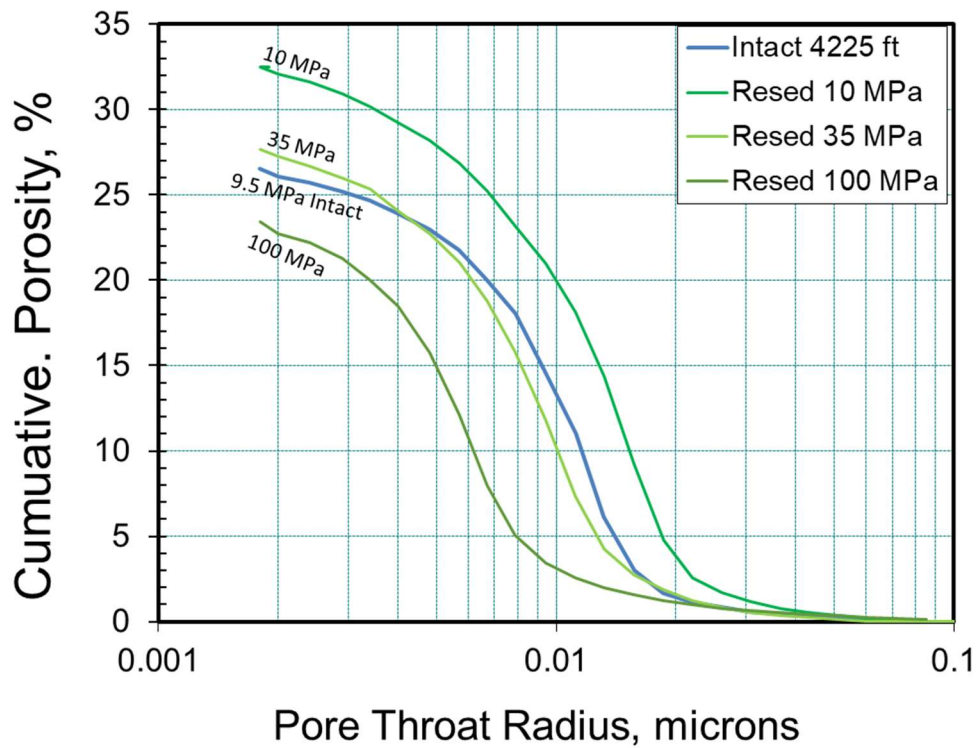
Figure 5-12: Cumulative porosity vs pore throat radius

108
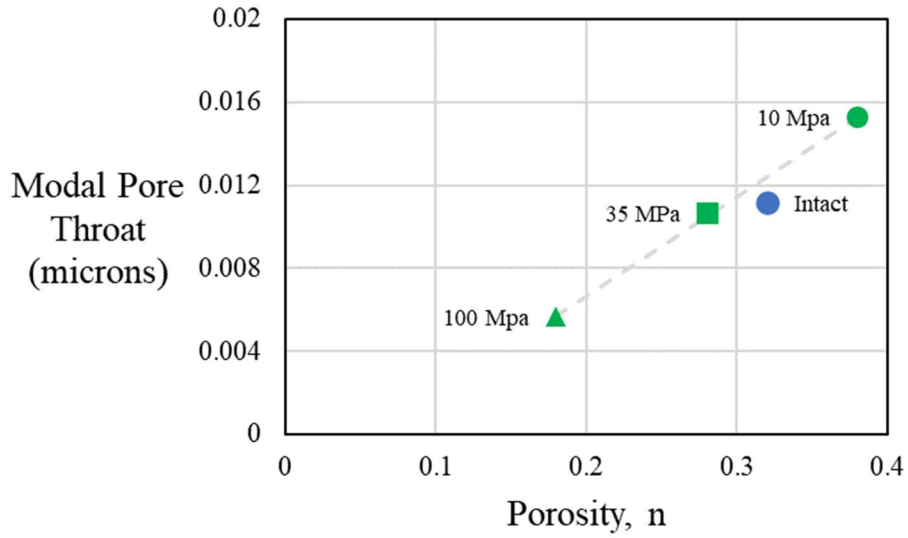
Figure 5-13: Porosity vs modal pore throat radius
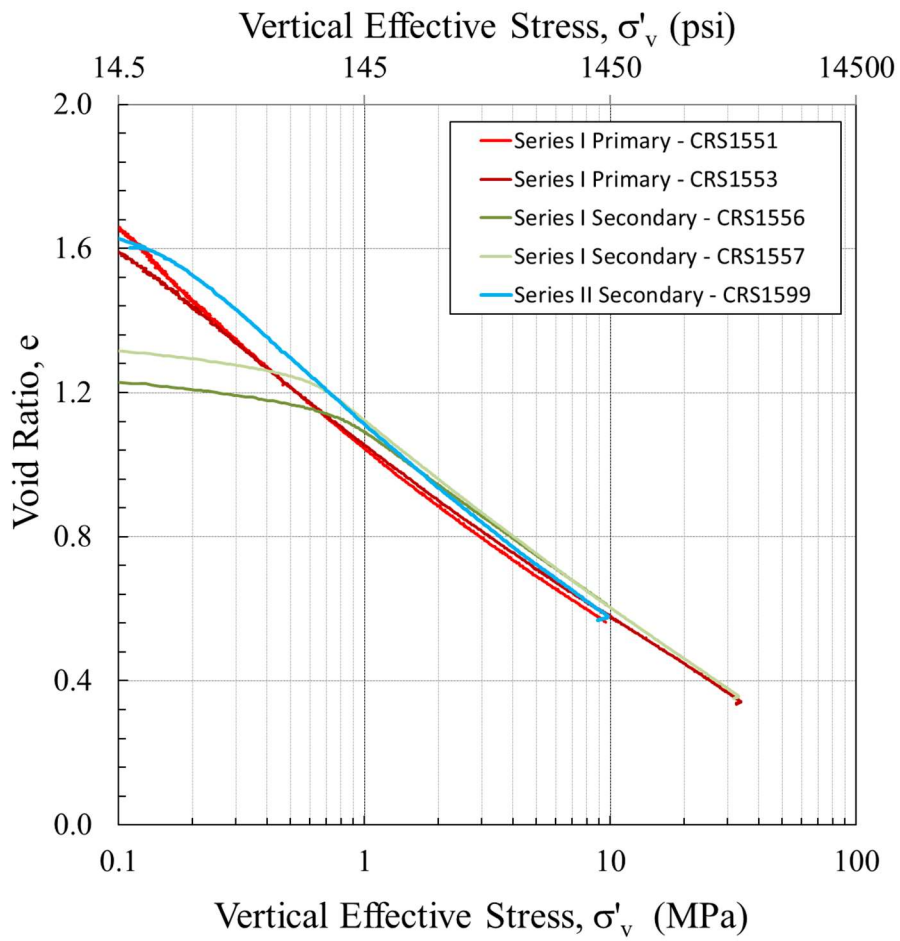
Figure 5-14: Low stress CRS compression curves: void ratio space

109
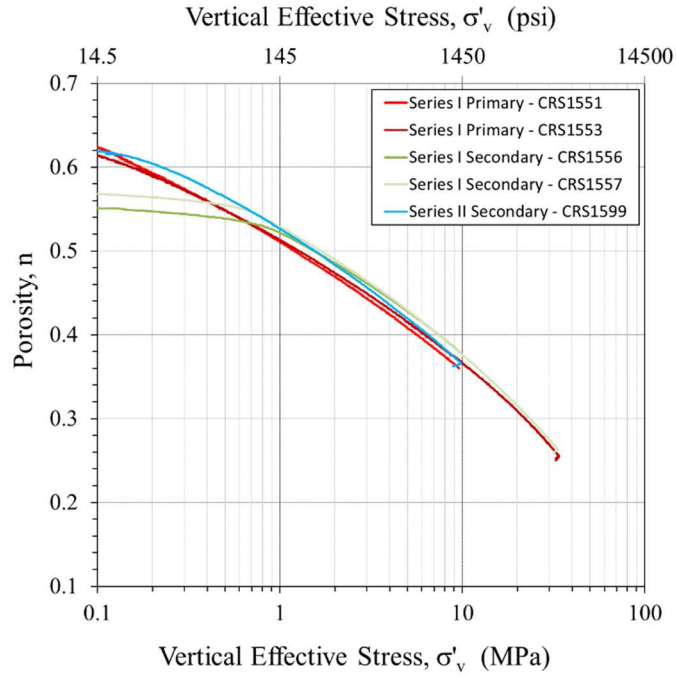
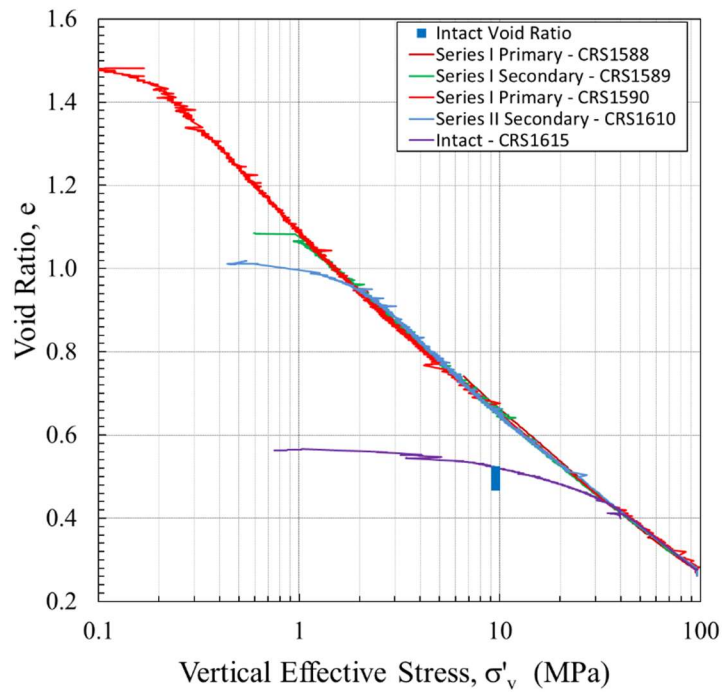Figure 5-15: Low stress CRS compression curves: porosity space
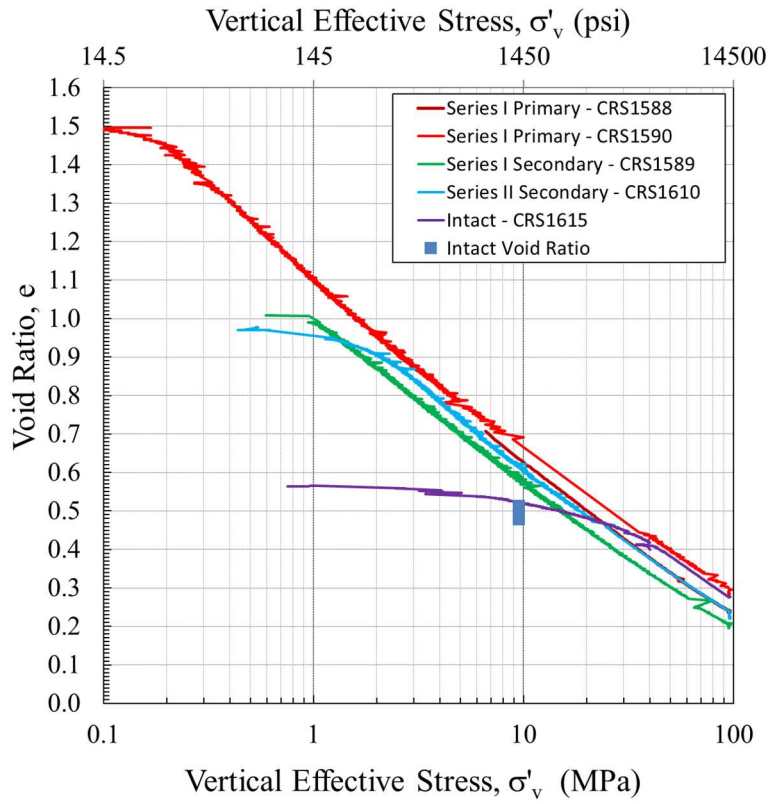
Figure 5-16: High stress CRS compression curves: void ratio space

110
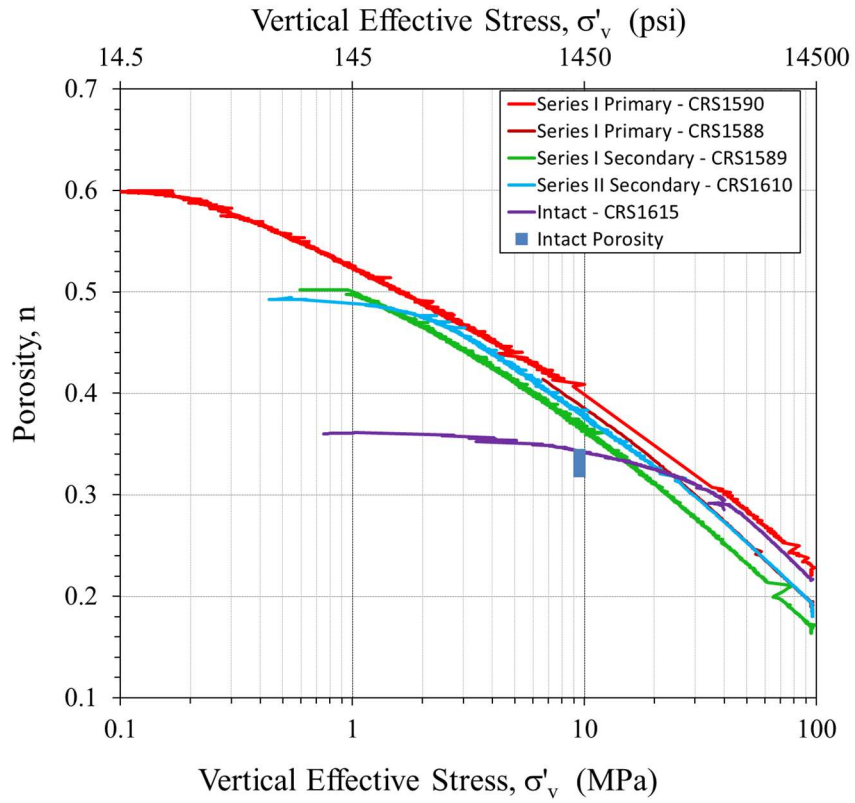
Figure 5-17: High stress CRS compression curves: porosity space

Figure 5-18: High stress CRS results with adjusted initial void ratios

111
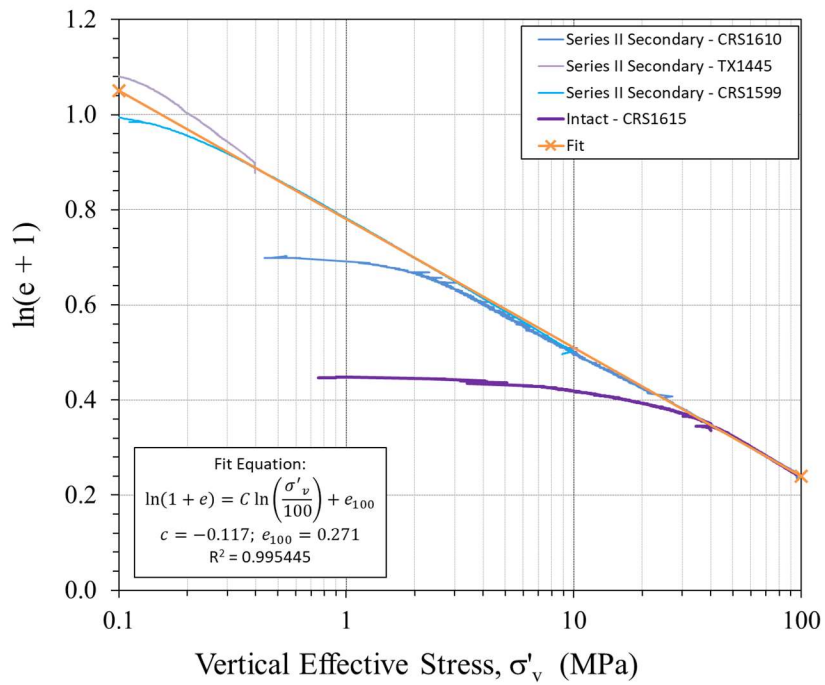
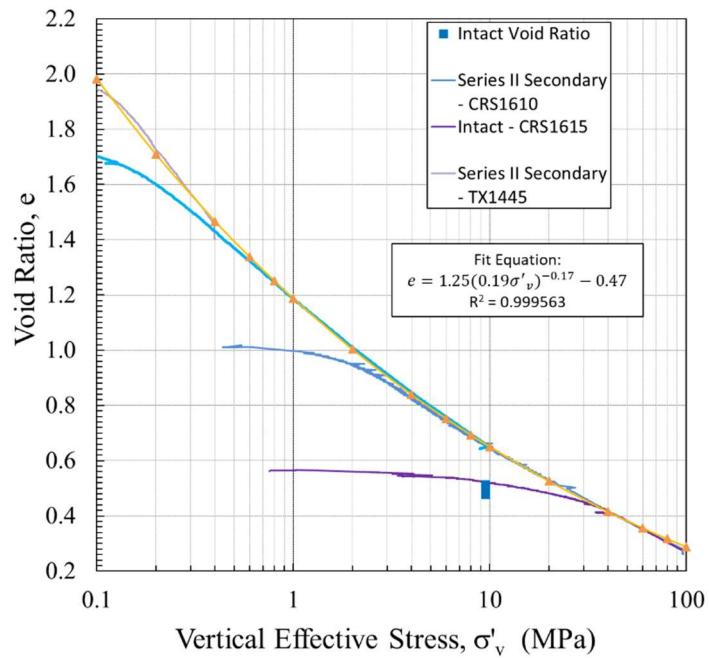Figure 5-19: Adjusted Series II CRS ln(1 + e) correlation

Figure 5-20: Adjusted Series II CRS exponential void ratio correlation
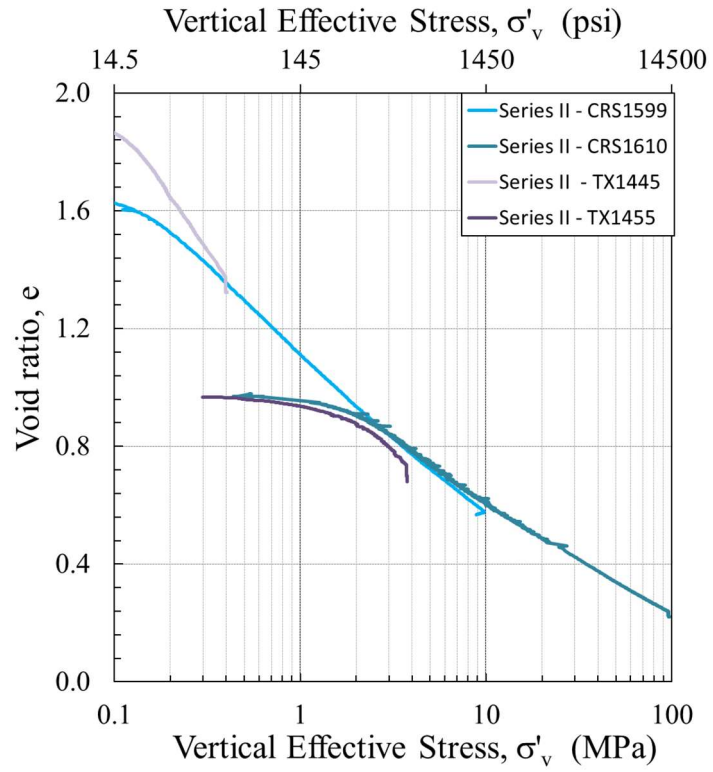
Figure 5-21: Triaxial K_0 consolidation compression curves

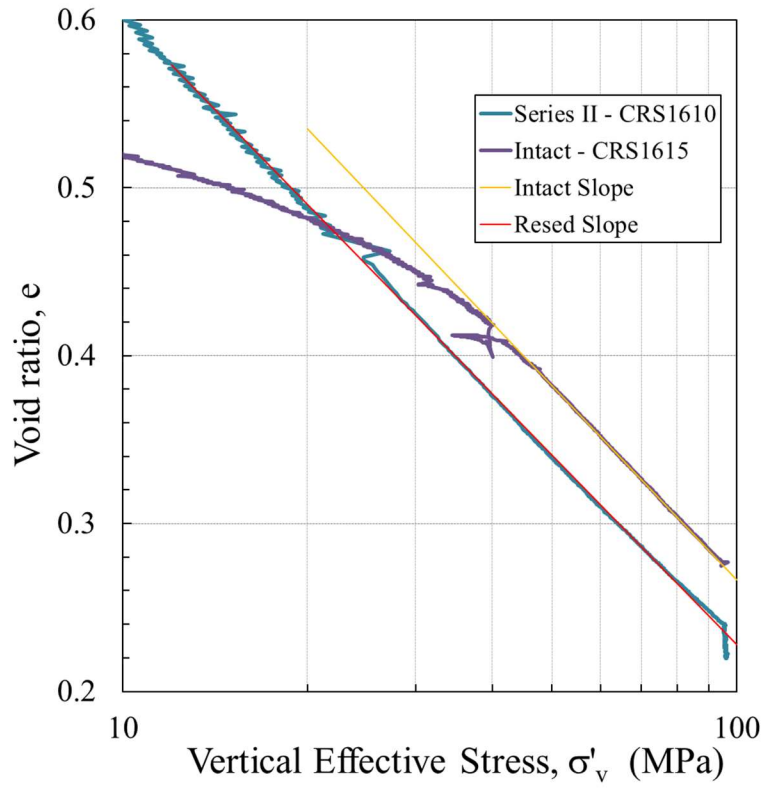Figure 5-22: Intact CRS specimens

113

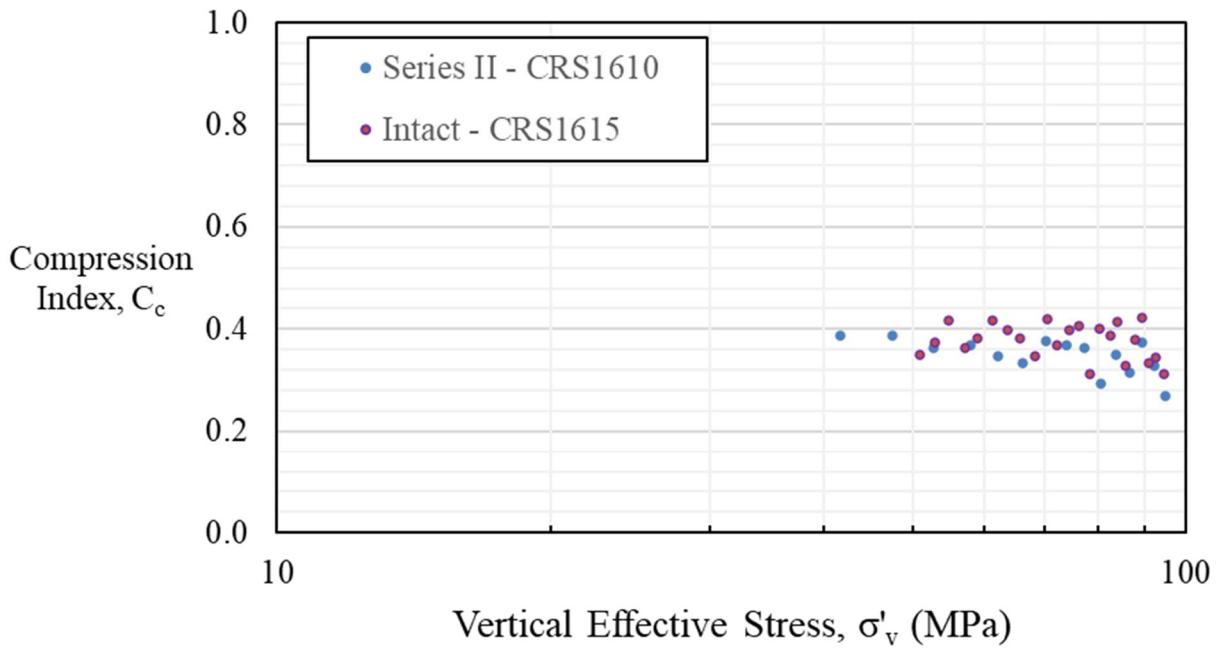Figure 5-23: Intact vs resedimented high stress CRS results

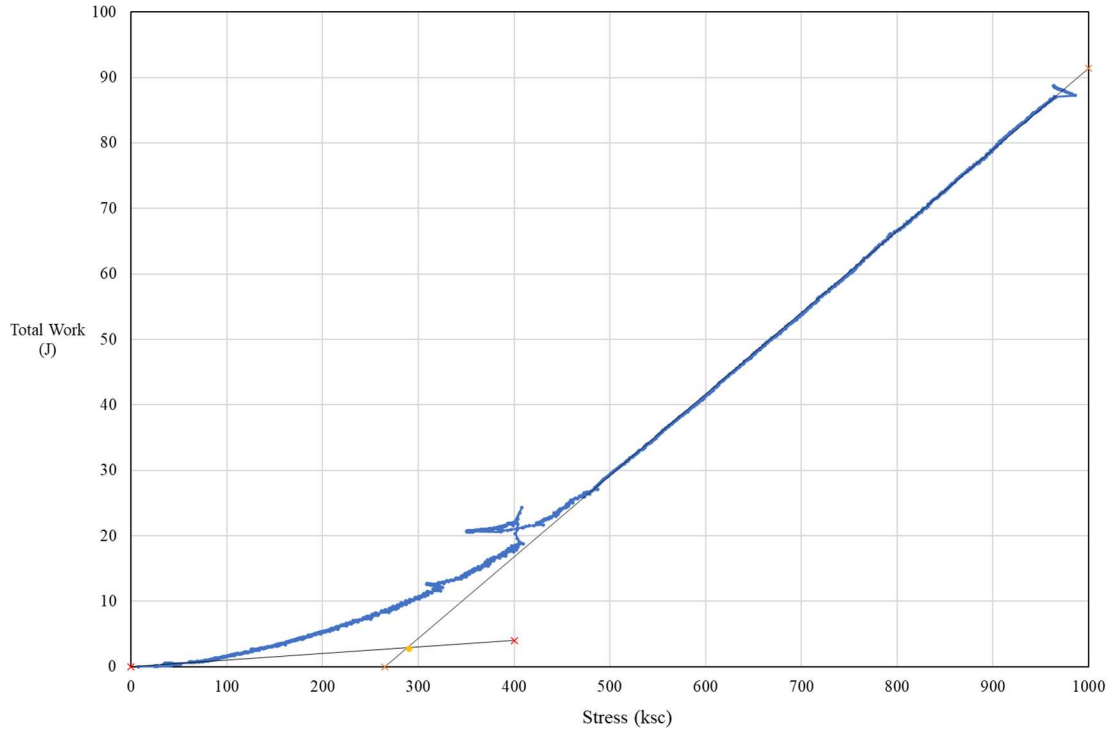Figure 5-24: High stress CRS compression index comparison

Figure 5-25: Strain energy construction for intact RGoG
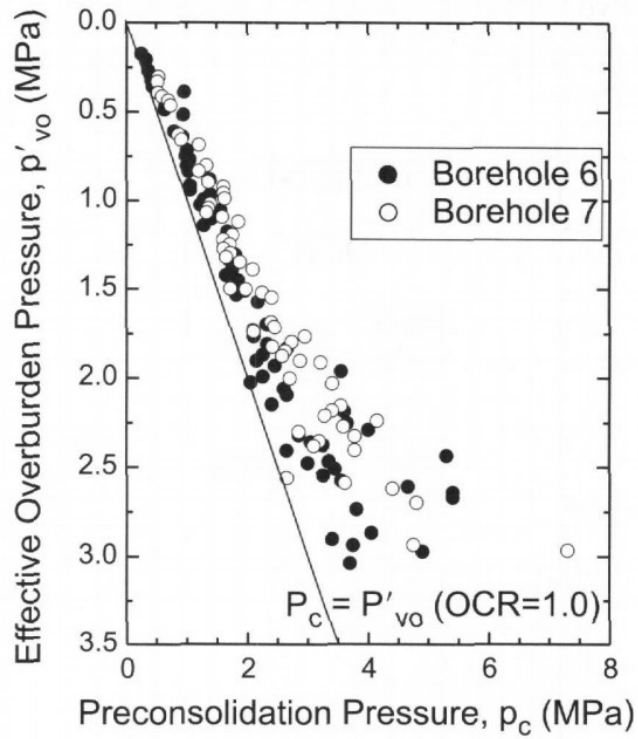Note: preconsolidation pressure is equal to 290 ksc (28.44 MPa)

Figure 5-26: Preconsolidation pressure from CRS tests compared to insitu effective stress
From: Tanaka, Ritoh, & Omukai, 2002

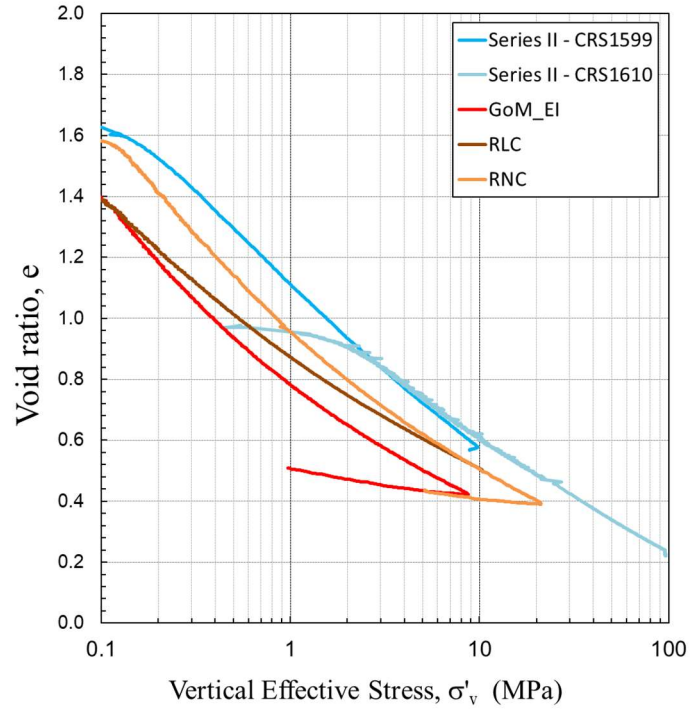Figure 5-27: Compression curves: comparison of RGoG to database
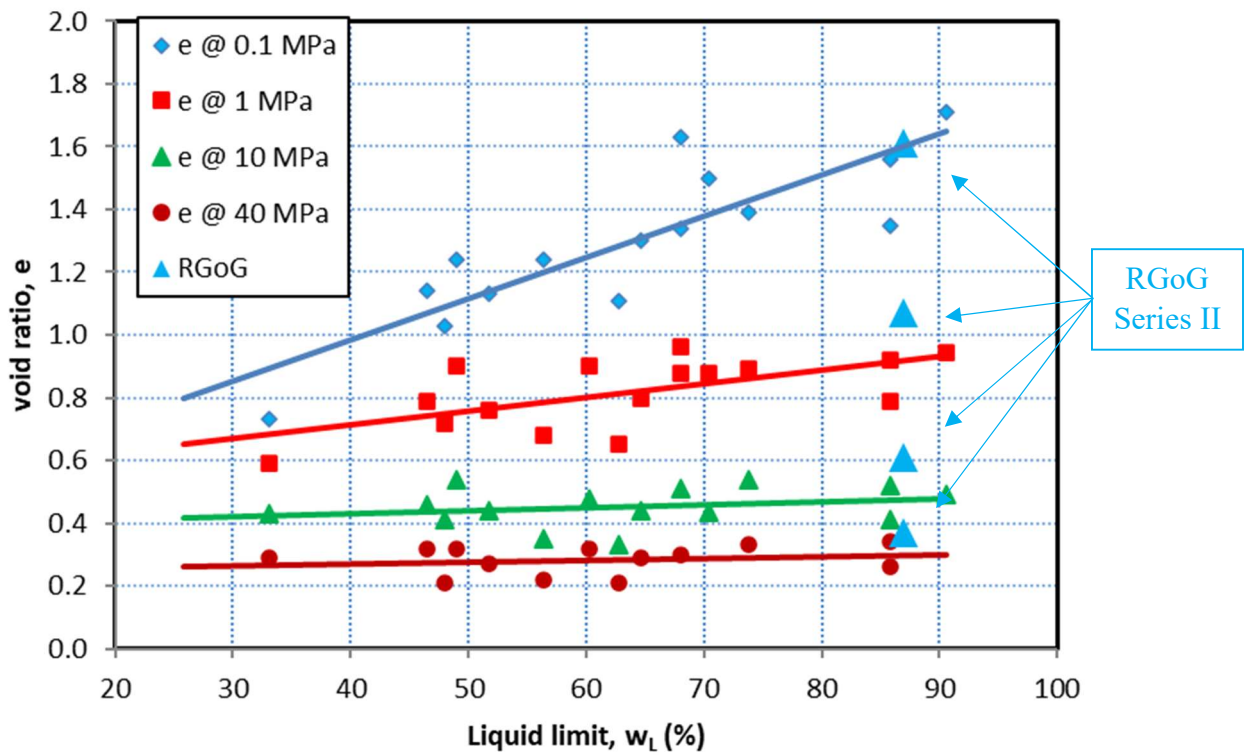

Figure 5-28: Liquid limit and compressibility correlations

116
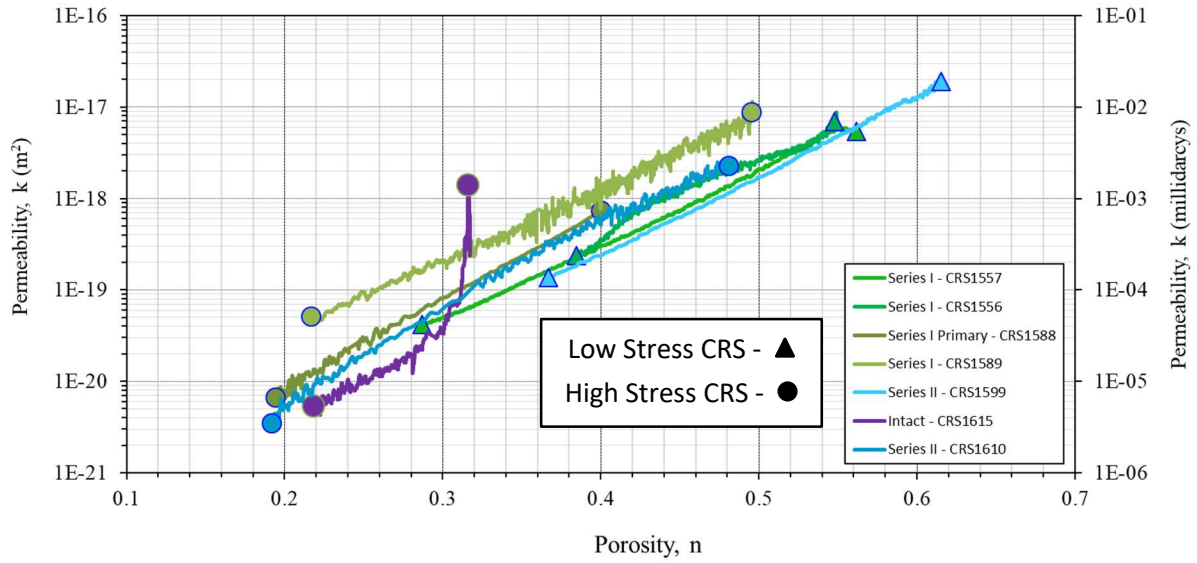
Figure 5-29: Permeability data: RGoG and GoG
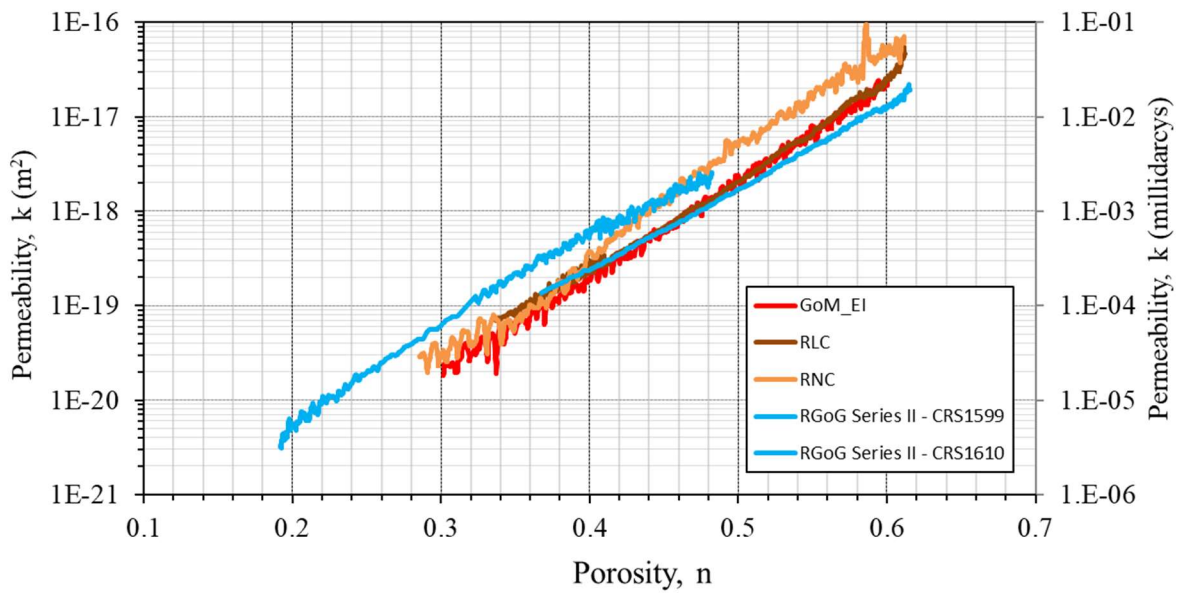
Figure 5-30: Permeability data: comparison of RGoG to database

117
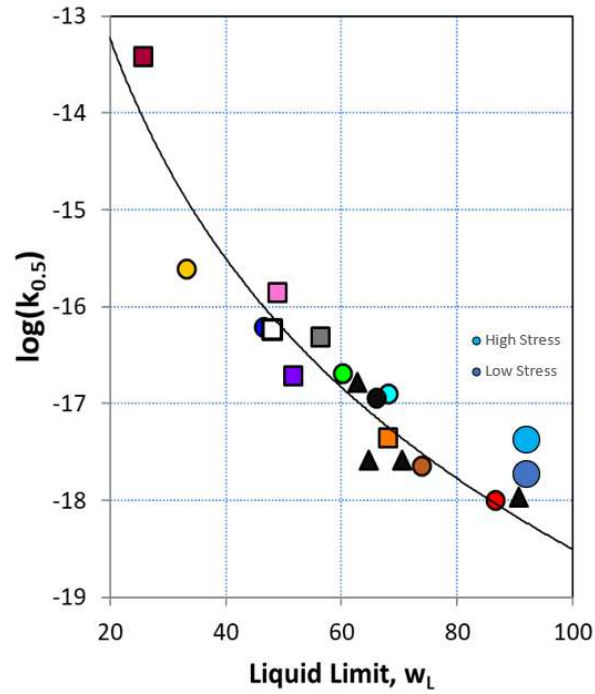
Figure 5-31: Liquid limit permeability correlation k_0 comparison
Other values from Casey, 2014
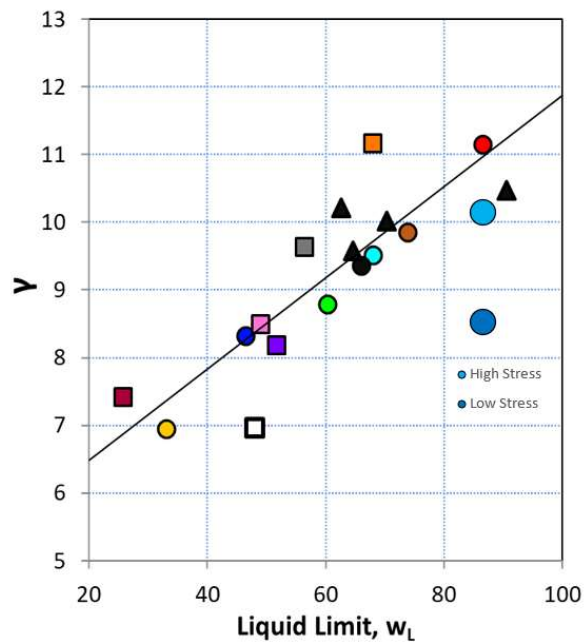
Figure 5-32: Liquid limit permeability correlation γ comparison
Other values from Casey, 2014

118

● RBBC
● GoM_EI
■ GoM_Ursa
● RLC
■ RNC
● RPC
● RSFBM
□ RUC
■ SS
■ RNSC
● RK_EPK
■ RK_VWK
□ RK_Cornwall

Figure 5-33: Key for figures Figure 5-31 and Figure 5-32
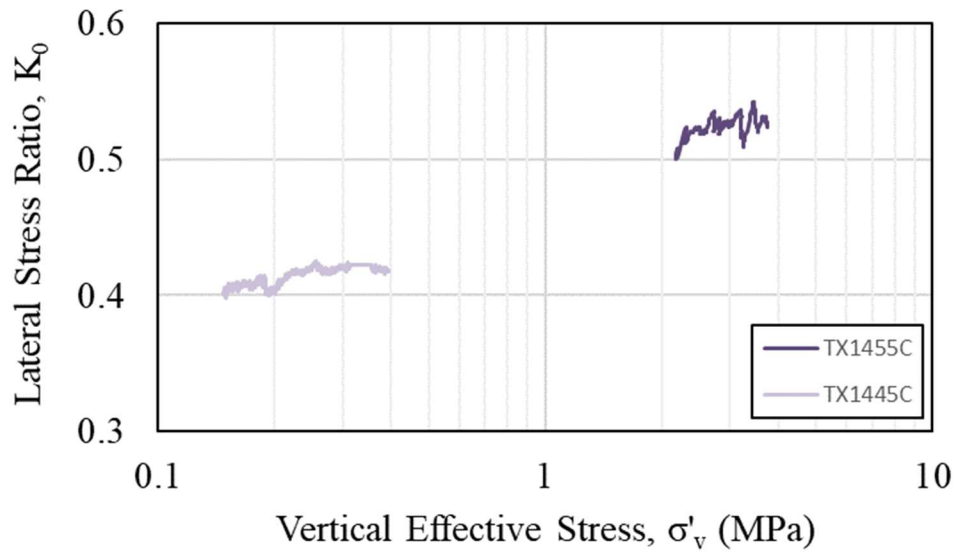
Figure 5-34: Lateral stress ratio K_0 vs effective stress
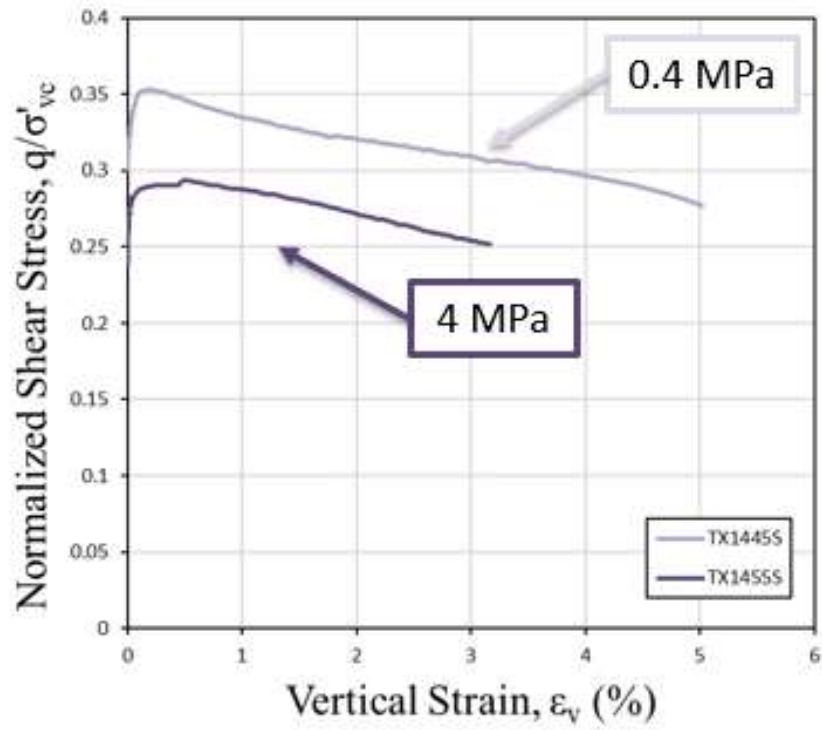
Figure 5-35: Triaxial stress-strain curves
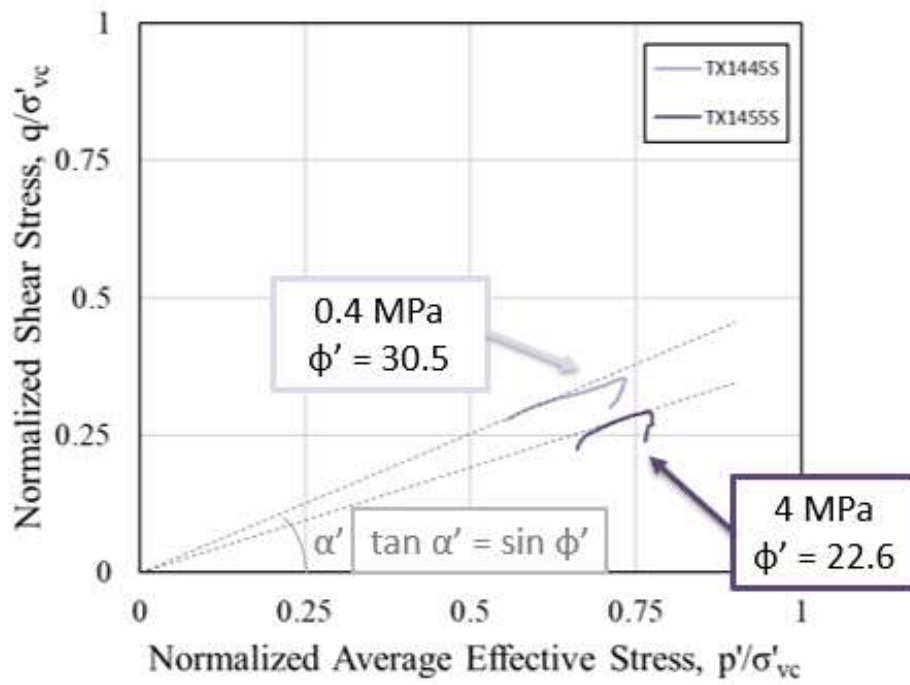
Figure 5-36: Triaxial results: p-q plot

Figure 5-37: Failure plane in low stress specimen

Figure 5-38: Failure plane in medium stress specimen
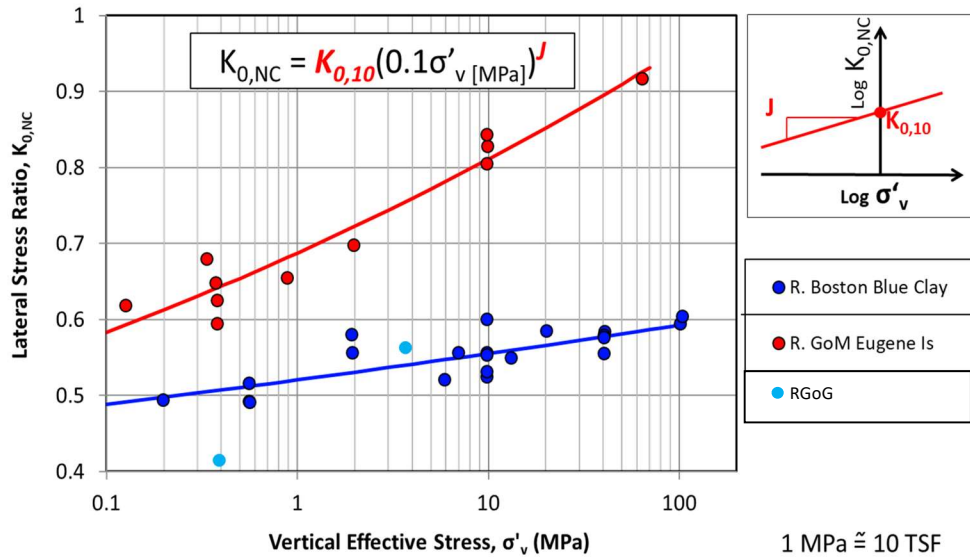
Figure 5-39: K_0 correlation comparison
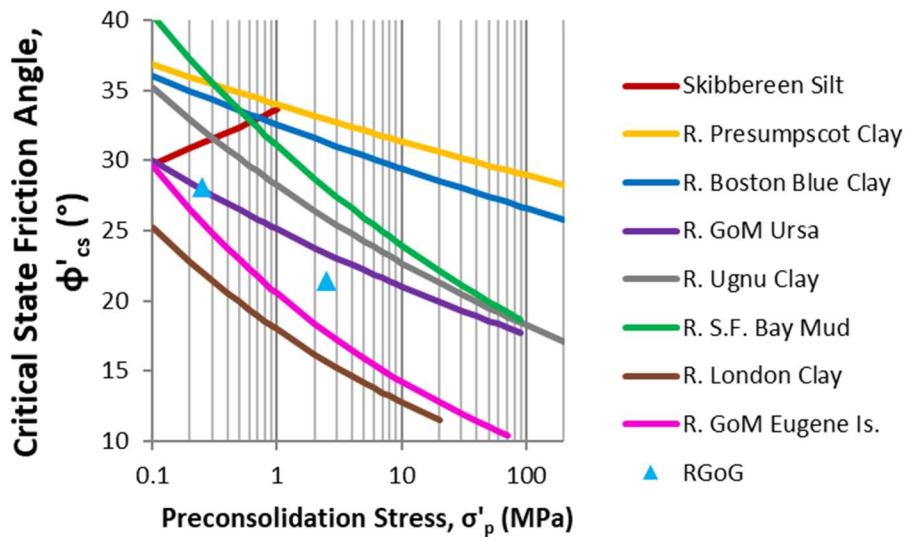
Figure 5-40: Critical state friction angle comparison to database
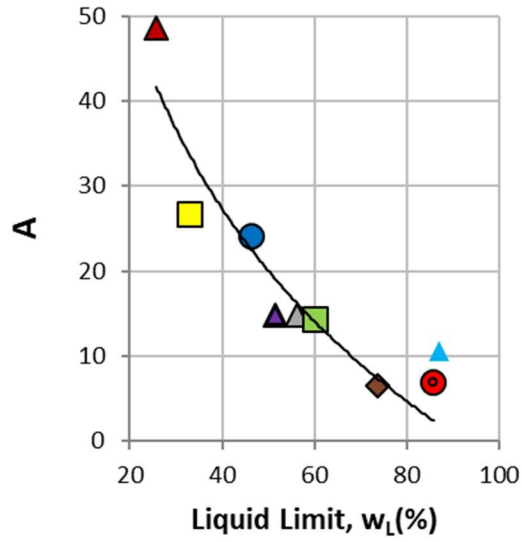
Figure 5-41: RGoG comparison to friction angle correlation: A parameter
Other values from Casey, 2014
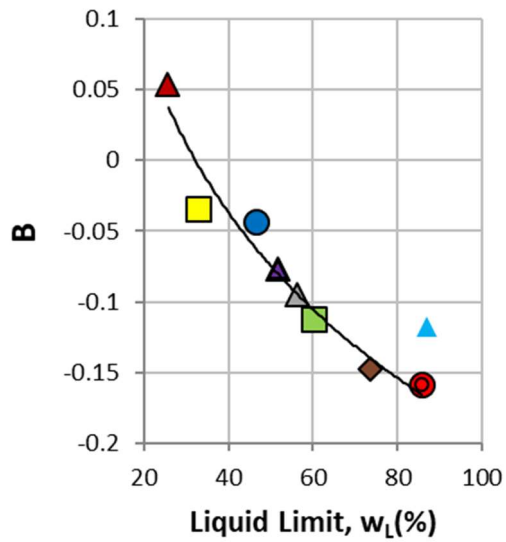
Figure 5-42: RGoG Comparison to friction angle correlation: B parameter
Other values from Casey, 2014
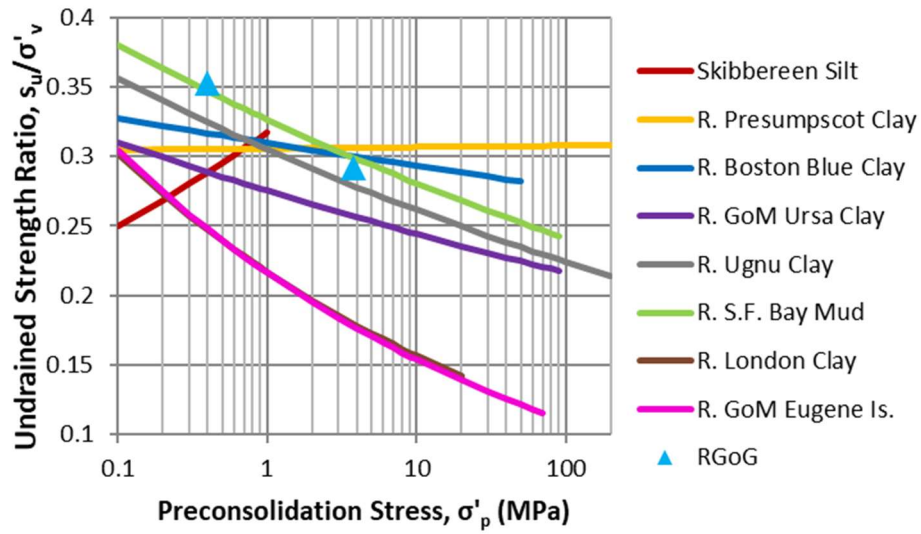
Figure 5-43: Normalized undrained shear strength comparison to database
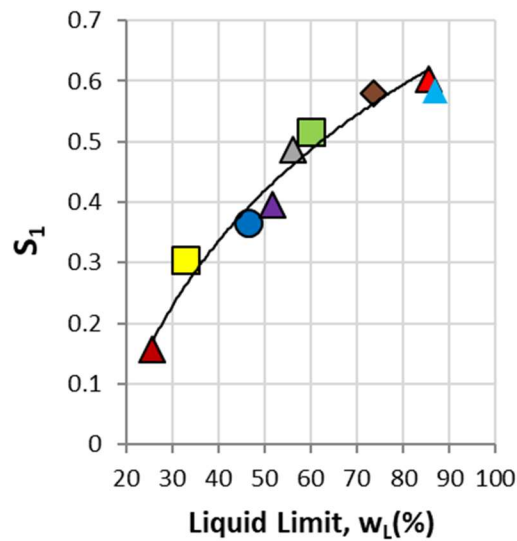
Figure 5-44: RGoG comparison to undrained shear strength correlation: S_1 parameter
Other values from Casey, 2014
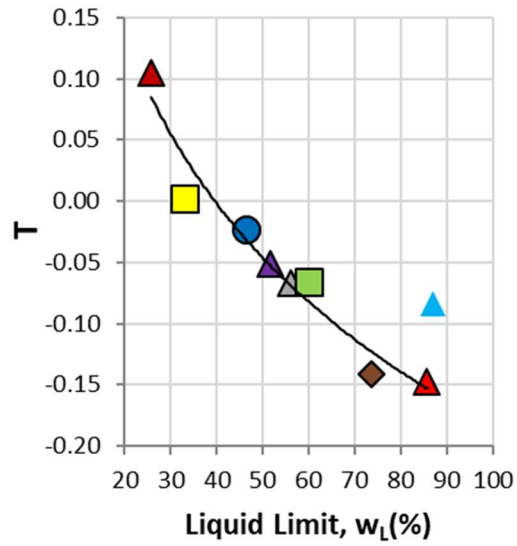
Figure 5-45: RGoG comparison to undrained shear strength correlation: T parameter
Other values from Casey, 2014

Figure 5-46: Key for figures Figure 5-41, Figure 5-42, Figure 5-44, and Figure 5-45

6 CONCLUSIONS AND RECOMMENDATIONS

The goal of this research was to classify a new material, Gulf of Guinea Miocene Mudrock and integrate it into the GeoFluids database (Table 2-1). Another goal was to compare intact GoG material behavior and compare it to RGoG behavior. This chapter summarizes the conclusions drawn in this thesis and some recommendations for future research.

6.1 RESEDIMENTATION

Resedimentation has been used for decades, as discussed in section 3.4.1 to create identical test specimens and develop correlations and material models. Resedimentation was used for this research to create test specimens used to analyze the engineering properties of Gulf of Guinea mudrock. The results of tests on resedimented material were used as the basis of comparison to intact behavior. The resedimentation process was modified slightly for this research for use with a wet slurry after secondary processing.

6.2 NEW METHODS

New methods for materials processing resedimented material were developed for this research. New methods for saturating, trimming, and testing intact specimens were also developed. The new methods developed during this research are summarized in this section.

6.2.1 Material Processing

Primary processing, grinding the bulk sample into a powder and homogenizing it, did not sufficiently reduce clay aggregates, so a new method of processing known as secondary processing was developed. The goal of secondary processing is to break apart the clay aggregates so that resedimentation accurately recreates the depositional environment of GoG. This method involves forming a slurry with primary processed powder and salt water and circulating the slurry though a shear pump. The circulation process continues until no clay aggregates are visible in the slurry. This processing technique resulted in a large increase in liquid limit and plasticity index.

6.2.2 Resedimentation

The resedimentation method discussed in section 3.4.1 was modified slightly to accommodate use of a wet slurry instead of a dry powder. The slurry was mixed to the desired

salt and water content prior to secondary processing then vacuumed and tremied into a consolidometer.

6.2.3   Intact Testing

This research was the first CRS test on a preserved intact GoG specimen in the Tufts lab. Methods for trimming and testing intact CRS GoG specimens were developed for the research. The trimming process for intact GoG specimens was more labor intensive and difficult than the process for a typical resedimented specimen (RGoG). The test specimen was at 45% saturation, much lower than all resedimented tests, during trimming and setup, and it was back pressure saturated in the CRS apparatus before loading. In the future, CRS GoG specimens should be brought to full saturation using the vacuum desiccator technique. The cell lines were vacuumed to prevent water from contacting the specimen. Then the lines and cell were flushed with water once the GoG specimen was under a load to prevent swelling.

6.3   PROPERTIES OF RGOG

Index tests, including XRD mineralogy, grain size distribution, Atterberg limits, specific gravity, and salt content were performed to classify RGoG. Then engineering tests, CRS compression and triaxial shear, were performed to analyze its engineering behavior. Conclusions from those tests are summarized in this section.

6.3.1   Index Tests

Approximately half of the clay fraction of GoG is kaolinite. The remainder is split evenly between illite and smectite. Kaolinite mineralogy is new for natural materials in the GeoFluids database. The amount of processing has a major effect on the Atterberg limits results. The Atterberg limits of secondary processed RGoG classify it as a high plasticity clay, which is unexpectedly high for a kaolinitic soil.

Hydrometer test results showed considerable bias, with results starting well above the 100% finer line, likely because of the presence of a structured water layer around the clay particles. Structured water is water on the surface of soil particles that does not have the same density as free water. The structured water layer in the hydrometer tests increased the density of the fluid in the cylinder and led to biased results. Pipette tests were used to provide an accurate

127

grain size distribution. No major differences exist between the grain size distributions of Series I and Series II.

6.3.2 Compressibility

Five low stress and four high stress CRS tests were performed on RGoG, as well as K_0 consolidation as part of the two triaxial tests. The curves have similar slopes and fall into a narrow range, although more scatter is present with the high stress curves. Two equations were developed to fit the virgin compression line of RGoG. The concavity of the curves does not match the expected concavity based on the liquid limit.

6.3.3 Permeability

The permeability of RGoG based on nine CRS tests is log linear and decreases with increasing porosity, as expected based on other materials in the database. Some scatter exists among high stress CRS permeability results.

6.3.4 Stress-Strain Strength

The lateral stress ratio K_0 increases as a function of stress level during the consolidation phase of each triaxial test and between the two tests. Peak friction angle and normalized shear strength decrease with stress level. The development of failure planes was an unexpected phenomenon that occurred during both the low stress and the medium stress test.

6.3.5 Comparison to Database

A comparison to correlations developed based on other materials in the GeoFluids database based on liquid limit yielded mixed results. High stress CRS permeability fit reasonably well into the permeability predictions from Casey (2014). The rates of change in K_0 and normalized undrained shear strength with increasing stress are similar to what was predicted based on liquid limit, but the actual values are much lower than expected. Friction angle was predicted reasonably well. All the materials used to develop the existing correlations are composed of smectite and illite, with very little kaolinite present. The mineralogical differences as well as structured water and other pore structure differences are possible explanations of the discrepancies between RGoG and the rest of the database.

6.4 COMPARISON OF RESEDIMENTED TO INTACT RESULTS

A major goal of this research is to analyze material properties of intact GoG and compare those properties to RGoG. The results of those comparisons are summarized in this section.

6.4.1 Mineralogy

Intact and non-preserved mineralogy show no major differences. Any differences are likely due to small sample sizes used for the test not capturing the representative mineralogy of the material. However, the mineralogy of the non-preserved and the intact core can be assumed to be the same.

6.4.2 Mercury Porosimetry

Mercury porosimetry tests were performed on resedimented specimens at various stress levels and intact specimens at the in situ stress of 9.5 MPa. The modal pore throat radius of the resedimented specimens decreased with increasing stress. The modal pore throat radius of resedimented specimens decreases linearly with porosity. The intact modal pore throat radius is below the resedimented line.

The shapes of the resedimented and intact curves are very similar at each stress level. Although the intact specimens are denser at the same stress level, the similar shapes show that the resedimented specimens are an accurate analog for the intact specimens. Oven drying is known to cause shrinkage and collapse of pores of all sizes, which directly impacts mercury porosimetry results. Mercury porosimetry is valuable to assess pore structure trends but should not be used to quantify changes in porosity.

6.4.3 Compression

Chevron measured the porosity of specimens cut from preserved intact core. Those porosities were compared to compression curves on RGoG. The intact porosity is significantly denser than the virgin compression line of RGoG at the same stress level. This result agrees with the mercury porosimetry results that show that RGoG is less dense at the in situ stress level.

A CRS test was performed on intact GoG and compared to the results for RGoG. The transition from recompression to virgin compression was very rounded. RGoG and GoG had the same compression index in their normally consolidated stress range. The yield stress of GoG calculated using the strain energy method was much higher than the in situ vertical effective

stress. The difference can be caused by several factors, including diagenesis, creep, underestimation of field stress, and sampling disturbance.

6.4.4   Permeability

The permeability of intact GoG followed the same trend as RGoG: log linear and decreasing with decreasing porosity. The intact permeability is lower than the resedimented porosity at the same given porosity value. This result is consistent with the modal pore throat radius of GoG being lower than that of RGoG at the same porosity based on the mercury porosimetry results.

6.5   RECOMMENDATIONS FOR FUTURE WORK

This thesis describes the preliminary study undertaken to classify Gulf of Guinea mudrock, understand its engineering properties, and compare intact and resedimented behavior. Several questions remain unanswered. Some recommendations for future research include:

- Atterberg limits
- Intact mercury porosimetry
- Intact CRS unloading
- Creep
- Resedimented triaxial tests
- Intact triaxial tests
- Other intact materials

Details of these recommendations are laid out in the following sections.

6.5.1   Atterberg Limits

This research confirmed that secondary processing has a major impact on the Atterberg limits of RGoG. Atterberg limits are correlated to many engineering properties, and they are the basis for assessing how the material fits in with existing correlations for the database. Quantifying the relationship between processing method and liquid limit would be worthwhile because RGoG has such a wide range in liquid limit depending on the processing technique.

Observing particles under a microscope to look for intact clay aggregates and performing sedimentation tests in a beaker to observe the coarse fraction as described in section 3.3.3 after

various amounts of processing could shed more light on this relationship. Performing Atterberg limits tests on preserved intact core would also provide a valuable comparison. However, Atterberg limits tests require a substantial amount of soil to perform the test, which is a drawback when working with a limited amount of material.

6.5.2   Intact Mercury Porosimetry

Now that a method for CRS testing of intact specimens has been developed, mercury porosimetry can be performed on compressed intact CRS specimens. The only mercury porosimetry that has been performed on intact GoG to date has been on GoG preserved at the in situ stress level of 9.5 MPa. Intact specimens can be compressed to stress levels up to 100 MPa, which allows MICP analysis over a full order of magnitude of stress level. MICP on intact specimens at increasing stress levels will provide a comparison of the evolution of pore structure with stress level between intact GoG and RGoG. The comparison would use the same CRS apparatus and methods and provide a direct comparison that could better explain differences between intact and resedimented permeability and porosity.

6.5.3   Intact CRS Unloading

Now that a method for CRS testing of intact specimens has been developed, more CRS tests should be performed on intact GoG. These tests can include an unload-reload portion after the intact yield stress has been reached and the specimen is undergoing normal consolidation, at around 50 MPa for example. The reloading curve will be a good comparison to the initial loading portion of the intact compression curves, which could provide insights into the difference between yield stress and in situ effective stress.

6.5.4   Creep

Creep is an important factor for assessing porosity, and it could provide valuable insight into the differences between intact and resedimented porosity. Analyzing creep rates by maintaining a constant load in the CRS cell on specimens at various stress levels for at least one log cycle of time after CRS loading could explain differences in porosity between intact and resedimented material.

6.5.5 Resedimented Triaxial Tests

Only two successful triaxial tests were performed on RGoG as part of this research. More triaxial tests should be performed over a range of stress levels for a more complete understanding of the strength properties of RGoG and a better comparison to the GeoFluids database. Particularly, medium stress tests to stress levels of 10 MPa should be performed to reach the in situ stress level of GoG and compare to intact triaxial results.

6.5.6 Intact Triaxial Tests

Chevron cut triaxial specimens from preserved intact core and sent them to the Tufts lab. Medium stress tests on those specimens should be performed for comparison to resedimented triaxial results.

6.5.7 Other Intact Materials

The comparison between intact and resedimented behavior could be further explored if other new materials are used for testing. Obtaining new intact core requires significant investment, but testing on materials of different lithologies and in situ stress levels would provide a more robust comparison and further insights into the similarities and differences of resedimentation.

APPENDIX – APPARATUS COMPRESSIBILITY

$f_n = net\ force\ accounting\ for\ cell\ pressure\ uplift\ and\ piston\ mass$

$f_a = ln(f_n)/ln(10)$

$d_f = apparatus\ compressibility\ for\ force\ f\ (cm)$

Low Stress CRS Compressibility

Piecewise equation:

For f_a < 2.75323

$d_f = 0.0001798(f_a)^4 - 0.000047(f_a)^3 - 0.00185364(f_a)^2 + 0.00510229(f_a) - 0.00110016$

For f_a > 2.75323

$d_f = 0.04007641(f_a)^3 - 0.34368844(f_a)^2 + 1.00149216(f_a) - 0.98031422$

High Stress CRS Compressibility

$d_f = (-2.67 \cdot 10^{-18})(f_n)^4 + (7.6 \cdot 10^{-14})(f_n)^3 - (7.36 \cdot 10^{10})(f_n)^2 + (4.4 \cdot 10^{-6})(f_n)$

REFERENCES

Abdulhadi, N. O. (2009). *An Experimental Investigation into the Stress-Dependant Mechanical Behavior of Cohesive Soil with Application to Wellbore Instability.* Cambridge, MA: PhD Thesis, MIT.

Anderson, D. G., & Stokoe, K. H. (1978). Shear Modulus: a Time-dependent Soil Property. *Dynamic Geotechnical Testing*. ASTM International.

Anderson, D. G., & Woods, R. D. (1976). Time-dependent Increase in Shear Modulus of Clay. *Journal of Geotechnical and Geoenvironmental Engineering, 102*(ASCE #12147 Proceeding).

ASTM International. (2011). *D4767-11 Standard Test Method for Consolidated Undrained Triaxial Compression Test for Cohesive Soils.* Retrieved from https://doi-org/10.1520/D4767-11

ASTM International. (2012). *ASTM D4186 Standard Method for One-Dimensional Consolidation Properties of Saturated Cohesive Soils Using Controlled-Strain Loading.* Retrieved from https://doi-org/10.1520/D4186_D4186M-12E01

ASTM International. (2014). *ASTM D5550-14 Standard Test Method for Specific Gravity of Soil Solids by Gas Pycnometer.* Retrieved from https://doi.org/10.1520/D5550-14

ASTM International. (2014). *ASTM D854-14 Standard Test Methods for Specific Gravity of Soil Solids by Water Pycnometer.* Retrieved from https://doi.org/10.1520/D0854-14

ASTM International. (2017). *ASTM D4318 - 17e1 Standard Test Methods for Liquid Limit, Plastic Limit, and Plasticity Index of Soils.* Retrieved from https://doi.org/10.1520/D4318-17E01

ASTM International. (2017). *ASTM D7928-17 Standard Test Method for Particle-Size Distribution (Gradation) of Fine-Grained Soils Using the Sedimentation (Hydrometer) Analysis.* Retrieved from Retrieved from https://doi.org/10.1520/D7928-17

Becker, D. E., Crooks, J. H., Been, K., & Jefferies, M. G. (1987). Work as a Criterion for Determining In Situ and Yield Stresses in Clays. *Canadian Geotechnical Journal, 24*(4), 549-564.

Betts, W. S. (2014). *Compressibility and Permeability of Gulf of Mexico Mudrocks, Resedimented and In-Situ.* Austin, TX: MS Thesis, University of Texas at Austin.

Brice, S. E., Cochran, M. D., Pardo, G., & Edwards, A. D. (1982). Tectonics and sedimentation of the South Atlantic rift sequence: Cabinda, Angola. *AAPG*, 5-20.

Broucke, O., Temple, F., Rouby, D., Robin, C., Calassou, S., Nalpas, T., & Guillocheau, F. (2004). The Role of Deformation Processes on the Geometry of Mud-dominated

Turbiditic Systems: Oligocene and Lower-Middle Miocene of the Lower Congo Basin (West African Margin). *Marine and Petroleum Geology, 21*(3), 327-348.

Bullard, E., Everett, J. E., & Gilbert Smith, A. (1965). The Fit of the Continents Around the Atlantic. *Philosophical Transactions of the Royal Society of London. Series A, Mathematical and Physical Sciences, 258*(1088), 41-51.

Burke, K., Dessauvagie, T. F., & Whiteman, A. J. (1971). Opening of the Gulf of Guinea and Geological History of the Benue Depression and Niger Delta. *Nature Physical Science, 233*, 51-55.

Burland, J. B. (1990). On the Compressibility and Shear Strength of Natural Clays. *Geotechnique, 40*(3), 329-378.

Casagrande, A. (1932). Research on the Atterberg Limits of Soils. *Public Roads, 13*(8).

Casagrande, A. (1936). The Determination of the Preconsolidation Load and its Practical Significance. *Proc. Int. Conf. Soil Mech. Found. Eng., 3*.

Casey, B. (2011). *The Significance of Specimen End Restraint in High Pressure Triaxial Testing of Cohesive Soil.* Cambridge, MA: MS Thesis, MIT.

Casey, B. (2014). *The Consolidation and Strength Behavior of Mechanically Compressed Fine-Grained Sediments.* Cambridge, MA: PhD Thesis, MIT.

Casey, B., Germaine, J. T., Flemmings, P. B., Reece, J. S., Gao, B., & Betts, W. (2013). Liquid Limit as a Predictor of Mudrock Permeability. *Marine and Petroleum Geology, 44*, 256-263.

Casey, B., Reece, J. S., & Germaine, J. T. (2019). One-dimensional Normal Compression Laws for Resedimented Mudrocks. *Marine and Petroleum Geology, 103*, 397-403.

Chevron USA, I. (2001). *Chevron Announces Seventh Significant Oil Find in Angola's Deepwater.* Oil and Gas Online. Retrieved from https://www.oilandgasonline.com/doc/chevron-announces-seventh-significant-oil-fin-0001

Daigle, H., & Screaton, E. J. (2015). Evolution of Sediment Permeability During Burial and Subduction. *Geofluids, 15*(1-2), 84-105.

Deirieh, A., Chang, I. Y., Casey, B., Joester, D., & Germaine, J. (2019). Impact of Drying and Effective Stresses on the Pore Space and Microstructure of Mudrocks. *Journal of Geophysical Research: Soild Earth, 124*(5), 4290-4304.

Diamond, S. (2000). Mercury Porosimetry, an Inappropriate Method for the Measurement of Pore Size Distributions in Cement-based Materials. *Cement and Concrete Research, 30*(10), 1517-1525.

Ferrari, A., Favero, V., & Laloui, L. (2016). One-Dimensional Compression and Consolidation of Shales. *International Journal of Rock Mechanics and Mining Sciences, 88*, 286-300.

Ge, C. (2019). *Compression Behavior of Smectitic vs. Illitic Mudrocks.* Cambridge, MA: PhD Thesis, MIT.

Germaine, J. T. (1982). *Development of the Directional Shear Cell for Measuring Cross-Anisotropic Clay Properties.* Cambridge, MA: ScD Thesis, MIT.

Germaine, J. T. (2015). Trends in Mechanically Compressed Sediment Behavior with Stress and Plasticity. *2015 Charles C. Ladd Memorial Lecture.*

Germaine, J. T., & Germaine, A. V. (2009). *Geotechnical Laboratory Measurements for Engineers.* John Wiley and Sons.

Germaine, J. T., & Ladd, C. C. (1988). State of the Art Paper: Triaxial Testing of Saturated Cohesive Soils. *Advanced Triaxial Testing of Soil and Rock, ASTM STP 997*, 421-459.

Hanley, A. J. (2017). *The Characterization of the Yield Surface for Fine-Grained Sediments.* Medford, MA: MS Thesis, Tufts University.

Head, K. H. (1980). *Manual of Soil Laboratory Testing.* Pentech Press.

Hogervorst, T., Bouma, H., & Vos, J. (2009). Evolution of the Hip and Pelvis. *Acta Orthopaedica. Supplementum., 80*, 1-39.

House, R. D. (2012). *A Comparison of the Behavior of Intact and Resedimented Boston Blue Clay (BBC).* Cambridge, MA: MS Thesis, MIT.

Karig, D. E., & Ask, M. V. (2003). Geological Perspectives on Consolidation of Clay-rich Marine Sediments. *Journal of Geophysical Research: Solid Earth, 108*(B4).

Kontopoulos, N. S. (2012). *The Effects of Sample Disturbance on Preconsolidation Pressure for Normally Consolidated and Overconsolidated Clays.* Cambridge, MA: PhD Thesis, MIT.

Ladd, C., & Varrallyay, J. (1965). *The Influence of Stress System on the Behavior of Saturated Clays During Undrained Shear.* Cambridge, MA: MIT.

Lambe, T. W., & Whitman, R. V. (1969). *Soil Mechanics.* John Wiley & Sons.

Lavier, L. L., Steckler, M. S., & Brigaud, F. (2001). Climatic and Tectonic Control of the Cenozoic Evolution of the West African Margin. *Marine Geology, 178*(1-4), 63-80.

Lowe, J., Jonas, E., & Obrican, V. (1969). Controlled Gradient Consolidation Test. *Journal of Soil Mechanics & Foundations Div, 92*, (SM5, Proc Paper 490).

Lunne, T., Berre, T., & Strandvik, S. (1997). Sample Disturbance Effects in Soft Low Plastic Norwegian Clay. *Proceedings of the Conference on Recent Developments in Soil and Pavement Mechanics*, (pp. 81-102). Rio de Janeiro.

Marques, A. C. (2015). *Turbiditic Reservoirs Simulation of Morphology by Multipoint Statistics and Evaluation of Petrophysical Properties.* Lisbon, Portugal: Masters Degree Disseration, NOVA University Lisbon.

McGinnis, J. P., Driscoll, N. W., Karner, G. D., Brumbaugh, W. D., & N., C. (1993). Flexural response of passive margins to deep-sea erosion and slope retreat: implications for relative sea-level change. *Geology, 21*, 893-896.

Mitchell, J. K., & Soga, K. (2005). *Fundamentals of Soil Behavior* (Vol. 3). New York: John Wiley & Sons.

Negrel, P., Allegre, C. J., Dupre, B., & Lewin, E. (1993). Erosion Sources Determined by Inversion of Major and Trace Element Ratios and Strontium Isotopic Ratios in River Water: The Congo Basin Case. *Earth and Planetary Science Letters, 120*(1-2), 59-76.

Parry, A. R. (2018). *The Effect of Temperature and Variation of Salinity during One Dimensional Consolidation.* Medford, MA: MS Thesis, Tufts University.

Powell, J. S., Take, W. A., Siemens, G., & Remenda, V. H. (2012). Time-dependent Behavior of the Bearpaw Shale in Oedometric Loading and Unloading. *Canadian Geotechnical Journal, 49*(4), 427-441.

Roberts, E., Jelsma, H. A., & Hegna, T. (2015). Mesozoic Sedimentary Cover Sequences of the Congo Basin in the Kasai Region. In *Geology and Resource Potential of the Congo Basin* (pp. 163-191). Springer, Berlin, Heidelberg.

Santagata, M. C. (1994). *Simulation of Sampling Disturbance in Soft Clays Using Triaxial Element Tests.* Cambridge, MA: MS Thesis, MIT.

Santagata, M., & Kang, Y. I. (2006). Effects of Geologic Time on the Initial Stiffness of Clays. *Engineering Geology, 89*(1-2), 98-111.

Savoye, B., Babonneau, N., Dennielou, B., & Bez, M. (2009). Geological Overview of the Angola-Congo Margin, the Congo Deep-Sea Fan and its Submarine Valleys. *Deep Sea Research Part II: Topical Studies in Oceanography, 56*(23), 2169-2182.

Schmertmann, J. H. (1991). The Mechanical Aging of Soils - 25th Karl Terzaghi Lecture. *Journal of Geotechnical Engineering, 117*(9), 1288-1330.

Seah, T. (1990). *Anisotropy of Resedimented Boston Blue Clay.* Cambridge, MA: ScD Thesis, MIT.

Seranne, M. (1999). Early Oligocene stratigraphic turnover on west Africa continental margin: a signature of the Tertiary greenhouse to icehouse transition? *Terra Nova, 11*, 135-140.

Seranne, M., Seguret, M., & Fauchier, M. (1992). Seismic super-units and post-rift evolution of the continental passive margin of southern Gabon. *Bulletin de la Société Géologique de France, 163*(2), 135-146.

Sheahan, T. (1991). *An Experimental Study of the Time-Dependent Undrained Shear Behavior of Resedimented Clay Using Automated Stress Path Triaxial Equipment.* Cambridge, MA: ScD Thesis, MIT.

Sheahan, T., & Germaine, J. T. (1992). Computer Automation of Conventional Triaxial Equipment. *Geotechnical Testing Journal, 15*(4), 311-322.

Skempton, A. W. (1954). The Pore-Pressure Coefficients A and B. *Geotechnique, 4*(4), 143-147.

Smith, R. E., & Wahls, H. E. (1969). Consolidation Under Constant Rates of Strain. *Journal of Soil Mechanics and Foundations Division, ASCE, 95*(2), 519-539.

Tanaka, H., Ritoh, F., & Omukai, N. (2002). Quality of Samples Retrieved from Great Depth and Its Influence on Consolidation Properties. *Canadian Geotechnical Journal, 39*(6), 1288-1301.

Uenzelmann-Neben, G. (1998). Neogene Sedimentaion History of the Congo Fan. *Marine and Petroleum Geology, 15*(7), 635-650.

Uenzelmann-Neben, G., Spiess, V., & Bleil, U. (1997). A Seisimic Reconnaissance Survey of the Northern Congo Fan. *Marine Geology, 140*(3-4), 283-306.

Willgoose, G., Bras, R. L., & Rodriguez, I. I. (1991). A Coupled Channel Network Growth and Hillslope Evolution Model: 2. Nondimensionalization Applications. *Water Resources Research, 27*(7), 1685-1696.

Wissa, A. E., Christian, J. T., Davis, E. H., & Heiberg, S. (1971). Consolidation at Constant Rate of Strain. *Journal of the Soil Mechanics and Foundations Division, ASCE, 97*(10), 1393-1416.

Zablocki, M. (2018). *Resedimented Nile Silty Clay (RNSC): Charactarization and Soil Behavior Comparison.* Medford, MA: MS Thesis, Tufts University.

Zhang, C., & Lu, N. (2018). What is the Range of Soil Water Density? Critical Reviews With a Unified Model. *Reviews of Geophysics, 56*(3), 532-562.